



Article scientifique

Article

2008

Published version

Open Access

This is the published version of the publication, made available in accordance with the publisher's policy.

---

## Mineral zoning and geochemistry of epithermal polymetallic Zn-Pb-Ag-Cu-Bi mineralization at Cerro de Pasco, Peru

---

Baumgartner, Regine; Fontboté, Lluís; Vennemann, Torsten

### How to cite

BAUMGARTNER, Regine, FONTBOTÉ, Lluís, VENNEMANN, Torsten. Mineral zoning and geochemistry of epithermal polymetallic Zn-Pb-Ag-Cu-Bi mineralization at Cerro de Pasco, Peru. In: Economic geology and the bulletin of the Society of Economic Geologists, 2008, vol. 103, p. 493–537. doi: 10.2113/gsecongeo.103.3.493

This publication URL: <https://archive-ouverte.unige.ch//unige:21616>

Publication DOI: [10.2113/gsecongeo.103.3.493](https://doi.org/10.2113/gsecongeo.103.3.493)

# Mineral Zoning and Geochemistry of Epithermal Polymetallic Zn-Pb-Ag-Cu-Bi Mineralization at Cerro de Pasco, Peru\*

REGINA BAUMGARTNER<sup>†,\*</sup> LLUÍS FONTBOTÉ,

*Department of Mineralogy, University of Geneva, 13 Rue des Maraichers, 1205 Genève, Switzerland*

AND TORSTEN VENNEMANN

*Institute of Mineralogy and Geochemistry, University of Lausanne Anthropole, 1015 Lausanne, Switzerland*

## Abstract

The large Cerro de Pasco Cordilleran base metal deposit in central Peru is located on the eastern margin of a middle Miocene diatreme-dome complex and comprises two mineralization stages. The first stage consists of a large pyrite-quartz body replacing Lower Mesozoic Pucará carbonate rocks and, to a lesser extent, diatreme breccia. This body is composed of pyrite with pyrrhotite inclusions, quartz, and black and red chalcodony (containing hypogene hematite). At the contact with the pyrite-quartz body, the diatreme breccia is altered to pyrite-quartz-sericite-pyrite. This body was, in part, replaced by pipelike pyrrhotite bodies zoned outward to carbonate-replacement Zn-Pb ores bearing Fe-rich sphalerite (up to 24 mol % FeS).

The second mineralization stage is partly superimposed on the first and consists of zoned east-west-trending Cu-Ag-(Au-Zn-Pb) enargite-pyrite veins hosted in the diatreme breccia in the western part of the deposit and well-zoned Zn-Pb-(Bi-Ag-Cu) carbonate-replacement orebodies; in both cases, sphalerite is Fe poor and the inner parts of the orebodies show typically advanced argillic alteration assemblages, including aluminum phosphate sulfate (APS) minerals. The zoned enargite-pyrite veins display mineral zoning, from a core of enargite-pyrite ± alunite with traces of Au, through an intermediate zone of tennantite, chalcopyrite, and Bi minerals to a poorly developed outer zone bearing sphalerite-galena ± kaolinite. The carbonate-hosted replacement ores are controlled along N35°E, N 90° E, N 120° E, and N 170° E faults. They form well-zoned upward-flaring pipelike orebodies with a core of famatinite-pyrite and alunite, an intermediate zone with tetrahedrite-pyrite, chalcopyrite, matildite, cuprobismutite, emplectite, and other Bi minerals accompanied by APS minerals, kaolinite, and dickite, and an outer zone composed of Fe-poor sphalerite (in the range of 0.05–3.5 mol % FeS) and galena. The outermost zone consists of hematite, magnetite, and Fe-Mn-Zn-Ca-Mg carbonates. Most of the second-stage carbonate-replacement orebodies plunge between 25° and 60° to the west, suggesting that the hydrothermal fluids ascended from deeper levels and that no lateral feeding from the veins to the carbonate-replacement orebodies took place.

In the Venenocha and Santa Rosa areas, located 2.5 km northwest of the Cerro de Pasco open pit and in the southern part of the deposit, respectively, advanced argillic altered dacitic domes and oxidized veins with advanced argillic alteration halos occur. The latter veins are possibly the oxidized equivalent of the second-stage enargite-pyrite veins located in the western part of the deposit.

The alteration assemblage quartz-muscovite-pyrite associated with the pyrite-quartz body suggests that the first stage precipitated at slightly acidic pH. The sulfide mineral assemblages define an evolutionary path close to the pyrite-pyrrhotite boundary and are characteristic of low-sulfidation states; they suggest that the oxidizing, slightly acidic hydrothermal fluid was buffered by phyllite, shale, and carbonate host rock. However, the presence in the pyrite-quartz body of hematite within quartz suggests that, locally, the fluids were less buffered by the host rock. The mineral assemblages of the second mineralization stage are characteristic of high- to intermediate-sulfidation states. High-sulfidation states and oxidizing conditions were achieved and maintained in the cores of the second-stage orebodies, even in those replacing carbonate rocks. The observation that, in places, second-stage mineral assemblages are found in the inner and outer zones is explained in terms of the hydrothermal fluid advancing and waning.

Microthermometric data from fluid inclusions in quartz indicate that the different ores of the first mineralization stage formed at similar temperatures and moderate salinities (200°–275°C and 0.2–6.8 wt % NaCl equiv in the pyrite-quartz body; 192°–250°C and 1.1–4.3 wt % NaCl equiv in the pyrrhotite bodies; and 183°–212°C and 3.2–4.0 wt % NaCl equiv in the Zn-Pb ores). These values are similar to those obtained for fluid inclusions in quartz and sphalerite from the second-stage ores (187°–293°C and 0.2–5.2 wt % NaCl equiv in the enargite-pyrite veins; 178°–265°C and 0.2–7.5 wt % NaCl equiv in quartz of carbonate-replacement orebodies; 168°–222°C and 3–11.8 wt % NaCl equiv in sphalerite of carbonate-replacement orebodies; and 245°–261°C and 3.2–7.7 wt % NaCl equiv in quartz from Venenocha). Oxygen and hydrogen isotope compositions on kaolinite from carbonate-replacement orebodies ( $\delta^{18}\text{O} = 5.3\text{--}11.5\text{‰}$ ,  $\delta\text{D} = -82$  to  $-114\text{‰}$ ) and on alunite from the Venenocha and Santa Rosa areas ( $\delta^{18}\text{O} = 1.9\text{--}6.9\text{‰}$ ,  $\delta\text{D} = -56$  to  $-73\text{‰}$ ). Oxygen isotope compositions of quartz from the first and second stages have  $\delta^{18}\text{O}$  values from 9.1 to 17.8 per mil. Calculated fluids in equi-

<sup>†</sup> Corresponding author: e-mail, regina.baumgartner@teckcominco.com

\* A digital supplement to this paper is available at <<http://www.geoscienceworld.org/>> or, for members and subscribers, on the SEG website, <<http://www.segweb.org/>>.

\* Present address: Teck Cominco Peru, Psje. los Delfines 159, Las Gardenias, Santiago de Surco Lima 33, Peru.

librium with kaolinite have  $\delta^{18}\text{O}$  values of 2.0 to 8.2 and  $\delta\text{D}$  values of  $-69$  to  $-97$  per mil; values in equilibrium with alunite are  $-1.4$  to  $-6.4$  and  $-62$  to  $-79$  per mil. Sulfur isotope compositions of sulfides from both stages have a narrow range of  $\delta^{34}\text{S}$  values, between  $-3.7$  and  $+4.2$  per mil; values for sulfates from the second stage are between 4.2 and 31.2 per mil. These results define two mixing trends for the ore-forming fluids. The first trend reflects mixing between a moderately saline ( $\sim 10$  wt % NaCl equiv) magmatic end member that had degassed (as indicated by the low  $\delta\text{D}$  values) and meteoric water. The second mixing indicates condensation of magmatic vapor with HCl and  $\text{SO}_2$  into meteoric water, which formed alunite.

The hydrothermal system at Cerro de Pasco was emplaced at a shallow depth ( $\sim 500$  m) in the epithermal and upper part of a porphyry environment. The similar temperatures and salinities obtained for the first stage and second stages, together with the stable isotope data, indicate that both stages are linked and represent successive stages of epithermal polymetallic mineralization in the upper part of a porphyry system.

## Introduction

RECENT GEOLOGIC studies of magmatic-hydrothermal systems have mainly concentrated on fluid evolution in porphyry copper and epithermal high-sulfidation Au-(Ag) deposits (Einaudi et al., 2003; Bethke et al., 2005; Fifiarek and Rye, 2005; Heinrich, 2005). However, less attention has been paid to associated epithermal polymetallic base metal deposits which occur in the upper parts of the same environment and which, according to crosscutting relationships and geochronological data, form later in the evolution of the system than the precious metal deposits. A number of such base metal deposits are superimposed on porphyry copper deposits (e.g., Butte, Morococha), whereas others have no known link to mineralized porphyry deposits (Einaudi et al., 2003). In the porphyry environment, epithermal high-sulfidation Au-(Ag) deposits also may be overprinted by such base metal deposits (e.g., Bendezú et al., 2003).

Epithermal polymetallic deposits are also referred to as Cordilleran base metal deposits, a term introduced by Sawkins (1972). The term Cordilleran base metal veins and/or deposits was subsequently used by Einaudi (1982), Gilbert and Park (1986), Bartos (1987), Macfarlane and Petersen (1990), Hemley and Hunt (1992), Bendezú and Fontboté (2002), and Bendezú et al. (2003, 2008). Cordilleran deposits have also been termed as Butte-type vein deposits (Meyer et al., 1968), polymetallic veins, and recently zoned base metal veins (Einaudi et al., 2003). The main features of Cordilleran base metal deposits can be summarized as follows, from Bendezú et al. (2008): (1) they have a close association in time and space with calc-alkaline igneous activity (i.e., in the same environment as most porphyry Cu and high-sulfidation epithermal Au-Ag deposits); (2) they form under epithermal conditions at shallow levels beneath the paleosurface; (3) they include Cu-Zn-Pb-(Ag-Au-Bi) metal suites, very rich in sulfides (up to more than 50% total sulfides), and have high Ag/Au ratios; (4) there is a well-developed zonation of ore and alteration minerals (core zones may also include high-sulfidation and advanced argillic alteration); (5) early pyrite-quartz cores are associated with low-sulfidation mineral assemblages containing pyrrhotite-(arsenopyrite) that can be extensive and form large bodies zoned outward to Zn-Pb ores; (6) they occur as open-space fillings (veins, breccia bodies) in silicate host rocks and as replacement in carbonate rocks; and (7) the base metals are deposited late in the evolution of the porphyry system (as seen from abundant crosscutting relationships and sparse geochronological data) after porphyry Cu, skarn, and high-sulfidation Au(-Ag) mineralization. Cordilleran base metal deposits have been historically an important source of Cu as well as Zn, Pb, and Ag in the North American

Cordillera and Peru. Table 1 summarizes the characteristics of several of these deposits.

The second largest known Cordilleran base metal deposit, after Butte (Montana), is Cerro de Pasco, in central Peru. It is a Zn-Pb-Ag-Cu-Bi deposit spatially related to a middle Miocene diatreme-dome complex. Post-1950 production plus known resources total more than  $\sim 175$  million metric tons (Mt) at 7 wt percent Zn and 2 wt percent Pb, as well as 3 oz/t Ag (Einaudi, 1977; Geological staff of Cerro de Pasco, 1950, pers. commun., 2001). In addition, prior to 1950, 1200 million ounces (Moz) Ag, 2 Moz of Au, and about 50 Mt at 2 wt percent Cu were mined (our estimate based on data of Jiménez, 1924; Geological staff of Cerro de Pasco Corporation, 1950; Einaudi, 1977; Fischer, 1977; Baumgartner, 2007). Contributions on the geology and mineralization at Cerro de Pasco include McLaughlin (1924), Bowditch (1935), Graton and Bowditch, (1936), Lacy (1949), Geological staff of Cerro de Pasco Corporation (1950), Jenks (1951), Ward (1961), Petersen (1965), Einaudi (1968, 1977), Silberman and Noble (1977), Mégard (1978), Rivera (1997), Angeles (1999), Baumgartner et al. (2003), and Baumgartner (2007). Several unpublished reports of Cerro de Pasco Corporation, CENTROMIN, and Volcán Compañía Minera S.A contain additional information on Cerro de Pasco.

While it is probable that silver was mined at Cerro de Pasco prior to the Spanish conquest, the first historic record of production from the district is in 1630 (Bowditch, 1935, and references therein). In the 19<sup>th</sup> century, Ag production declined and most claims at Cerro de Pasco were acquired by the American Cerro de Pasco Corporation (1906–1970). Two mineralization stages occur at Cerro de Pasco. The first consists of a large pyrite-quartz body with pipelike pyrrhotite bodies zoned to Zn-Pb ores characterized by marmatitic sphalerite, mainly the Cayac Noruega A, B, and J-337 and K-327A orebodies: see Einaudi, 1977; these orebodies were exploited underground in the late 1940s, as well as the the oxidized portion of the eastern part of the deposit (belonging to the second mineralization stage). The second mineralization stage comprises polymetallic base metal carbonate-replacement orbodies on the eastern part of the deposit and enargite pyrite veins on the western part; the latter narrow and rich copper veins and orebodies (mainly enargite and chalcopyrite) were exploited down to a depth of 700 m at the beginning of Cerro de Pasco Corporation. In the early 1970s, the mine was nationalized and was integrated into the state-owned CENTROMIN. In 1999, Cerro de Pasco was again privatized and Volcán Compañía Minera S.A., the current owner, took the control of the mine.

Mineralization at Cerro de Pasco comprises two stages with contrasting mineralogy (Einaudi, 1977; Baumgartner, 2007).

TABLE 1. Examples of Polymetallic Epithermal Deposits (Cordilleran type)

Location	Age	First-stage ore minerals <sup>5</sup>	Second-stage ore minerals <sup>4,5</sup>	Host rock	Type of orebodies	References
Cerro de Pasco, Peru <sup>1</sup>	15–11 Ma	py-qtz body, po, asp, sl	enr, lz, fm, tt-tn, sl, gn	Mainly carbonate rocks (Pucará Grp.) but also diatreme breccia and siliciclastic rocks (Excelsior Fm.)	Veins and replacement bodies	Baumgartner et al. (2003), this study, Einaudi (1977), Petersen (1965)
Colquijirca, Peru <sup>1</sup>	10.6–12.4 Ma		enr, cpy, tn-tt, bn, sl, gn	Mainly carbonate Pocobamba Fm. but also in diatreme breccia and dacitic volcanic rocks	Veins and replacement bodies	Bendezú et al. (2003), Fontboté and Bendezú (1999, 2001), Bendezú (2007)
Huanzala, Peru <sup>1</sup>	7.7 ± 0.4 Ma	po, asp, sl	tn, enr	Santa Formation limestone	Replacement bodies	Imai et al. (1985), Soler et al. (1986), Imai (1986)
Hualgayoc, Peru <sup>1</sup>	~11 Ma		replacement bodies: po, asp, sl, veins: enr, tn, cp, pyrg, sl, gn	Limestones from the Chulec Fm. and sandstone from the Goyllarisquizga Group and the Inca Fm.	Veins and replacement bodies	MacFarlane and Petersen (1990)
Julcani, Peru <sup>1</sup>	10.1–7.0 Ma		enr, cp, sl, gn	Dacite-rhyolite domes	Veins	Deen et al. (1994)
Morococha, Peru <sup>1</sup>	9.1 and 6.4 Ma	py-qtz body, po, mt, sl, gn	enr, tn-tt, cp, sl, gn	Quartz-monzonite porphyry stocks and limestones (Pucará Grp.)	Replacement bodies and veins	Barrenes (1970), Petersen (1965), Beuchat (2003)
San Cristobal, Peru <sup>1</sup>	~5-6 Ma	py-qtz body, py, wf, asp, sl	tt, sl, gn	Pucará Group limestone, Mitu Group volcanics	Veins and replacement bodies	Beuchat (2003), Campbell (1983), Bartlett (1984)
Quiravilca, Peru <sup>1</sup>	Miocene		enr, tn-tt, cp, sl, sn	Andesitic lavas and quartz-monzonite porphyry	Veins	Bartos (1987)
Yauricocha, Peru <sup>1</sup>	Late Miocene	py-qtz body	enr, cp, bn, cv, sl, gn	Mainly limestones (Machay Fm.) but also granodiorite stocks	Replacement bodies and veins	Petersen (1965), Thomson (1960), Alvarez and Noble (1988)
Pasto Bueno, Peru <sup>1</sup>	~9 Ma	wf, po, asp, mo	late stage: enr, tt, sl, gn	Quartz-monzonite Consuzo stock	Veins	Landis and Rye (1974)
Huarón, Peru <sup>1</sup>	~15 Ma	po, wf, cst, asp, cp, sl	Late stage: enr, lz, cp, tn-tt, sl, gn	Eocene to Oligocene sandstone and conglomerate and quartz-monzonite porphyric dikes (Callipuy volcanism)	Veins and replacement bodies	Thouvenin (1984)
Bor, Serbia <sup>1</sup>	65 ± 4 Ma		enr, cp, bn, tn-tt, sl, gn	Andesite, volcanoclastic rocks, pyroclastic rocks	Veins and replacement bodies	Sillitoe (1983), Jankovic et al. (1980)
Main and East Tintic, Utah, United States <sup>1</sup>	Late Eocene		enr, tn-tt, Ag-gn, sl	Paleozoic limestones (Ophir Fm.)	Replacement bodies and veins	Shepard et al. (1968), Morris (1968), Hildreth and Hannah (1996)
Magma, Arizona, United States <sup>2</sup>	Paleocene		cp, bn, sl, tn, enr, cc, dg, gn	Devonian Martin limestones	Replacement bodies and veins	Ransome (1912), Short and Etlinger (1926), Short et al. (1943), Gustafson (1961), Hammer and Peterson (1968), Paul and Knight (1995)
Butte Main stage, Montana, United States <sup>2</sup>	66–63 Ma		enr, cc, bn, cv, dg, tn, cp, sl, gn	Butte quartz-monzonite	Veins	Sales and Meyer (1949), Proffett (1979), Meyer et al. (1968), Brimhall, (1979)
Bisbee, Arizona, United States <sup>2</sup>	Late Jurassic		enr, bn	Argillaceous limestone	Replacement bodies	Bryant (1964), Frieauf (1998), Schwartz and Park (1932)
Cananea, Mexico <sup>2</sup>			lz, cv, cp, sl, gn	Limestone (Puertecitos Lm.)	Replacement bodies	Emmons (1910), Kelley (1935), Perry (1961)

TABLE 1. (Cont.)

Location	Age	First-stage ore minerals <sup>5</sup>	Second-stage ore minerals <sup>4,5</sup>	Host rock	Type of orebodies	References
Bingham, "non-porphry ores," Utah, United States	37.0–38.5 Ma		cp, sl, gn, tn	Sandstone and limestone	Veins and replacement bodies	Rubright and Hart (1968); ages compiled in Landtving (2004); Inan and Einaudi (2002)
Chuquicamata, Chile. Main stage veins (superimposed on early porphyry) <sup>3</sup>	31–33 Ma		py, enr, ep, bn, tt-tn supergene cc and cv	Chuqui porphyry Complex	Veins	Sillitoe (2000), Ossandon et al. (2001)
La Escondida, Late stage, Chile <sup>3</sup>	38–36 Ma		enr, cv, ep, bn, tn, sl, gn	Paleocene andesite, and quartz-monzonite porphyry	Veins	Padilla et al. (2001)
Collahuasi, Rosario vein, Chile <sup>3</sup>	32.9 Ma (porphyry stage)		py-ep-(tn), py-bn-(enr), cc-dg-cv	Porphyry stock and volcano-sedimentary rocks	Veins	Hunt (1985), Diek et al. (1994), Clark et al. (1998), Masterman et al. (2005)

<sup>1</sup> Main ore in the district

<sup>2</sup> Subordinate ore in the district

<sup>3</sup> Cordilleran ores are not mined

<sup>4</sup> Pyrite accompanies ore minerals

<sup>5</sup> First and second stage are referred to early and late

Mineral abbreviations: asp = arsenopyrite; bn = bornite; cc = chalcocite; cp = chalcopyrite; cst = cassiterite; cv = covellite; dg = digenite; enr = enargite; fm = famatinite; gn = galena; lz = luzonite; mt = magnetite; mo = molybdenite; nk = nukundamite; po = pyrrhotite; pyrg = pyrrargyrite; py = pyrite; sl = sphalerite; tn = tetrahydrite; tt = tetrahedrite; wf = wolframite

This contribution presents a study of the mineralogical zoning of the Cerro de Pasco deposit and a fluid inclusion and stable isotope study of ore and gangue minerals. The mineralogical study includes field and petrographic documentation of the well-zoned polymetallic mineralization of the second stage and updates the early descriptions of Ward (1961) and Einaudi (1968, 1977) of the first mineralization stage. The documentation of the second-stage polymetallic mineralization has become possible because of recent extensive mine development in the eastern part of the open pit, which allowed a detailed description of the structure, morphology, mineralogy, and zoning of the newly exposed orebodies at Cerro de Pasco. For the fluid inclusion and stable isotope study, samples were collected from both mineralization stages. Fluid inclusions were measured in quartz (from the first and second mineralization stages) and sphalerite (second mineralization stage). Cathodoluminescence (CL) imaging was used in the fluid inclusion survey in order to highlight different quartz generations. The mineralogical and microthermometric data, combined with stable isotope measurements of sulfide, sulfate, carbonate, and silicate minerals from the first and second mineralization stages, constrain the temperature, pH, redox state, salinity and origin of the ore-forming fluids and provide information on their spatial and temporal evolution.

#### District and Deposit Geology at Cerro de Pasco

Cerro de Pasco is located on the high Andean plateau of central Peru, at an elevation of 4,300 m. A regional north-south longitudinal fault juxtaposes Paleozoic metamorphic rocks with Mesozoic sedimentary rocks (Fig. 1). In the mine area, the longitudinal fault is believed to be represented by high-angle, N 15° W-striking reverse faults (Fig. 2). The oldest exposed rocks at Cerro de Pasco are weakly metamorphosed shale, phyllite, and quartzite of the Devonian Excelsior Group. On the eastern side of the diatreme-dome complex, the Excelsior Group phyllite forms a north-south-striking and north-plunging anticline, named the Cerro anticline (Fig. 3). This Group is overlain in an angular unconformity by sandstone and conglomerate with pebbles of quartz and Excelsior-type argillaceous clasts belonging to the Permo-Triassic Mitu Group (McLaughlin, 1924; Jenks, 1951). Outcrops of the Mitu Group are rare in the vicinity of the Cerro de Pasco district and become more widespread to the south (Fig. 1). Above the eastern half of the district, the Mitu Group is covered by a thick (up to 3000 m) Upper Triassic-Lower Jurassic carbonate sequence belonging to the Pucará Group (Angeles, 1999; Rosas et al., 2007). This carbonate sequence is principally composed of thick-bedded, dark-colored limestone and dolomite with local shale interbeds and siliceous concretions (Jenks, 1951). In the western part of the district, the Pucará Group is only 300 m thick and consists of thin-bedded, light-colored limestone (Jenks, 1951).

From the Eocene to lower Miocene, multiple folding episodes with a northeast-southwest axial direction brought the Excelsior, Pucará, and the Mitu Group rocks to shallower levels. In the Middle Miocene, magmatic activity affected the region (Silberman and Noble, 1977; Bendezú et al, 2003; Baumgartner, 2007; Bendezú, 2007). At Cerro de Pasco, as in the nearby Colquijirca district, magmatism consisted of an early phase of explosive volcanism, represented mainly by a

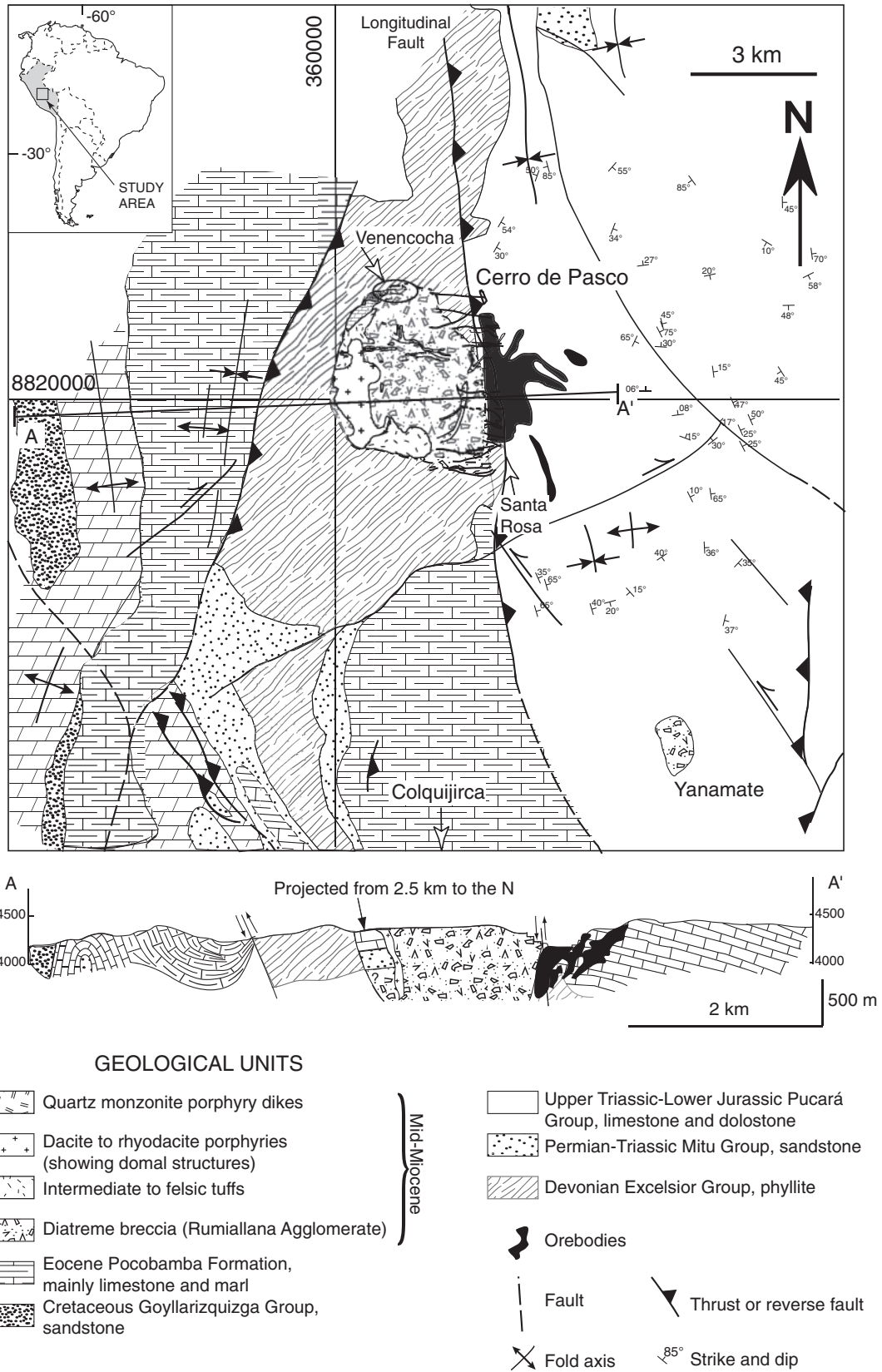


FIG. 1. Regional geologic map (modified from Bendezú et al., 2003) and schematic west-east (A-A') cross section of the Cerro de Pasco district. The cross section illustrates the present topography at Cerro de Pasco.

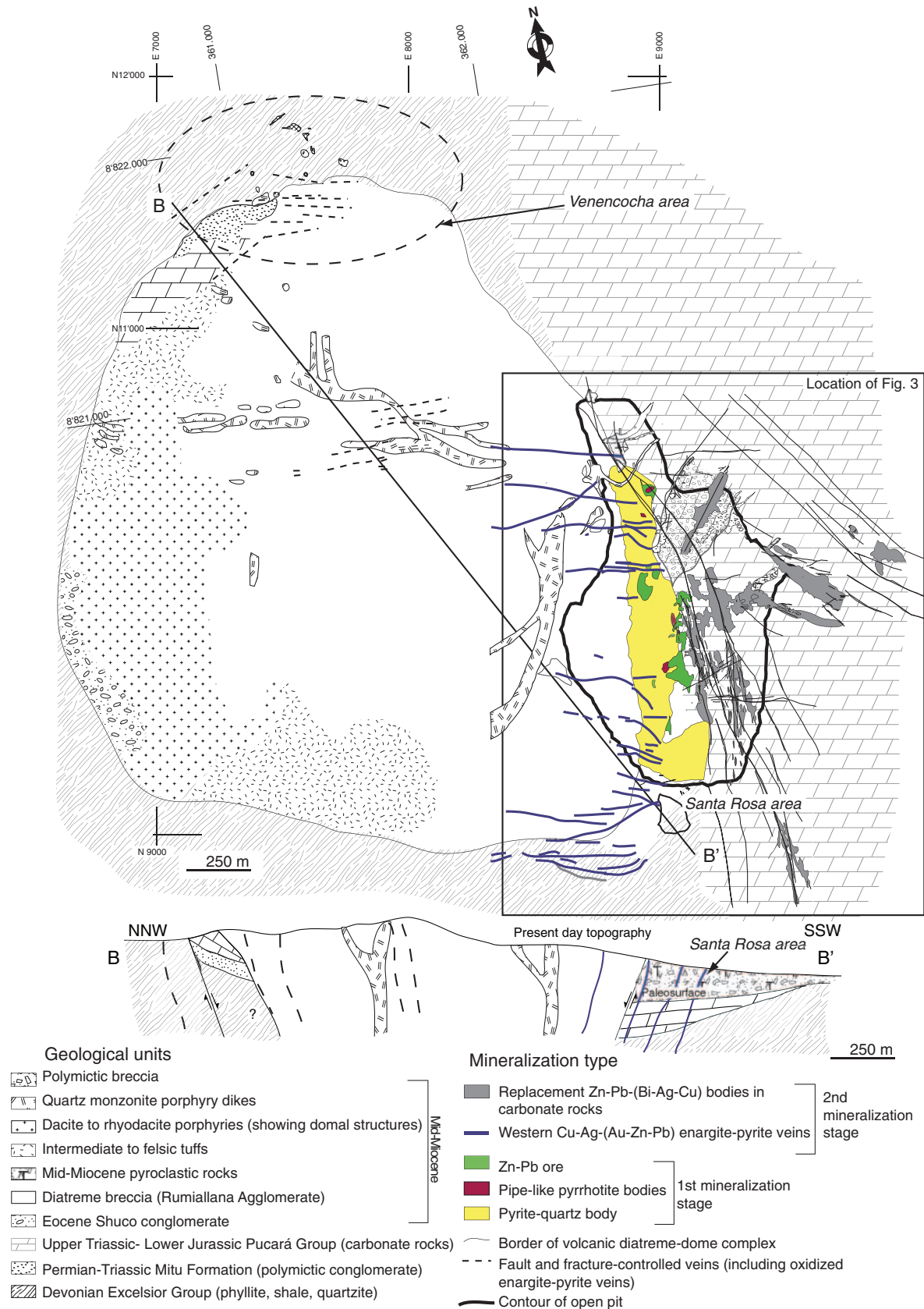
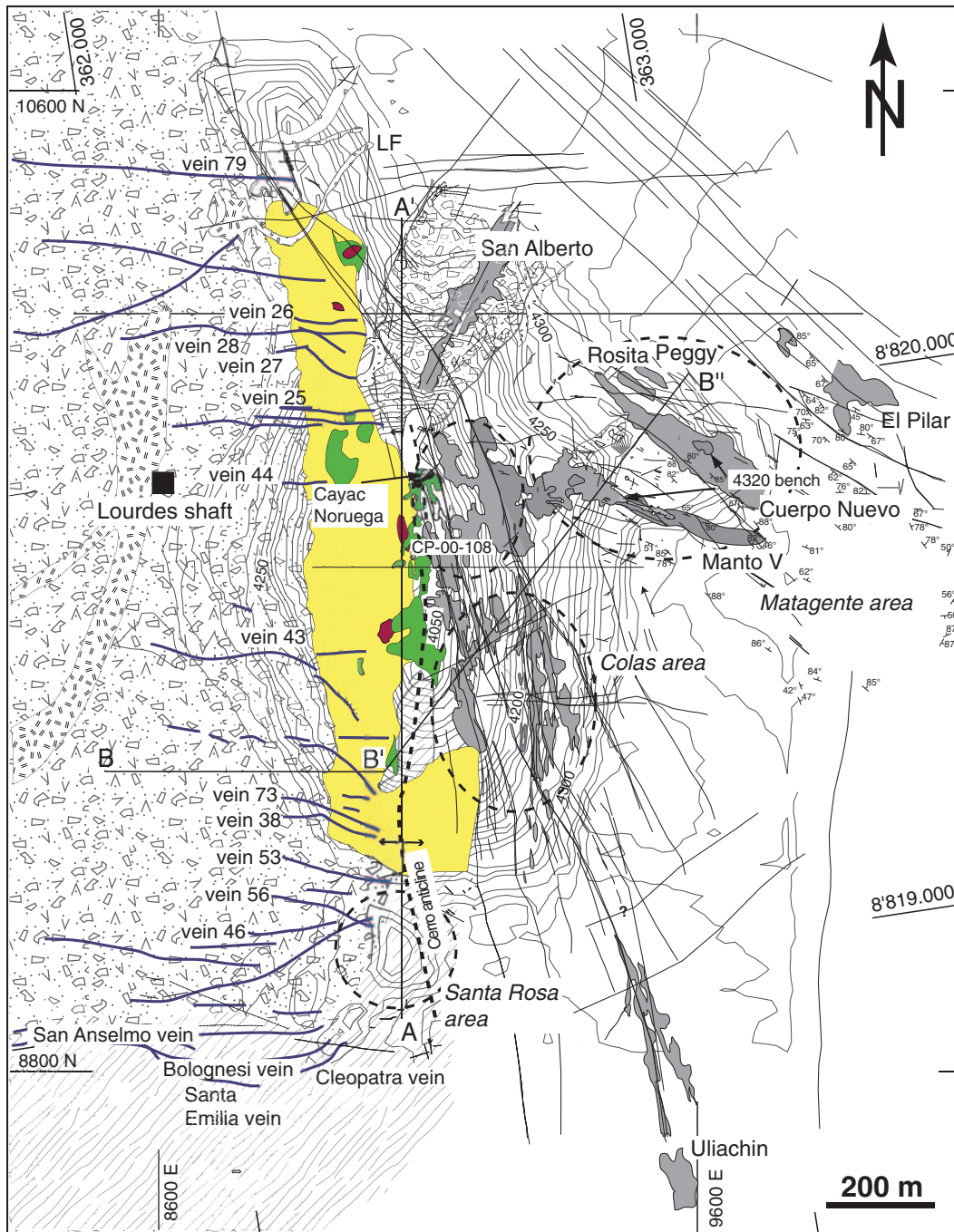


FIG. 2. Geologic map of the diatreme-dome complex at Cerro de Pasco, compiled from Rogers (1983) and Huanqui (1994, unpub. report). The mineralization types occurring in the open pit (plain black line) are shown, as well as the names of the principal orebodies studied here.



Geological units		Mineralization type	
	Mid-Miocene (?) polymictic breccia		Zn-Pb-(Bi-Ag-Cu) replacement (Fe-poor sphalerite)
	Mid-Miocene quartz-monzonite porphyry dikes		Cu-Ag-Au-(Zn-Pb) energite-pyrite vein
	Mid-Miocene diatreme breccia (Rumiallana agglomerate)		Pipe-like pyrrhotite body
	Upper Triassic-Lower Jurassic Pucará Group		Zn-Pb ore (Fe-rich sphalerite)
	Devonian Excelsior Group		Pyrite-quartz body
			4300 Open pit contours

	Stage I		Folding axis
	Stage II		Faults
			Strike and dip

FIG. 3. Geologic map of the Cerro de Pasco open pit, showing the rock units, the structure, and the different mineralization stages, based on maps of the Cerro de Pasco Geology staff. Lines labeled A-A' and B-B'-B'' indicate locations of cross sections in Figures 4 and 5.

dacitic diatreme breccia (known locally as Rumiallana Agglomerate), and sparse external volcanic deposits (only recognized southeast of the diatreme, in the Santa Rosa area; Fig. 2), followed by multiple dacitic porphyritic domes at 15.4 Ma (Baumgartner, 2007) and quartz-monzonite porphyry dikes intruded at 15.4 to 15.1 Ma (Baumgartner, 2007). The presence of vertical breccia bodies with angular clasts of several centimeters in size of Pucará carbonate rocks and carbonate rock-flour matrix suggests that diatreme-related fluid expulsion occurred through the sedimentary sequence. These breccia bodies follow a northeast-southwest-trending corridor in the San Alberto area and can also be recognized in the north-south-trending large pyrite-quartz body (Fig. 3, see below).

Erosion removed part of the diatreme-dome complex, as well as the overlying rocks, as shown by the presence of collapsed blocks of Mitu and Pucará Group rocks inside the diatreme and the absence of these rocks outside the diatreme (Figs. 1, 3; Baumgartner, 2007). The total erosion from the middle Miocene to the present is probably on the order of 500 m, as indicated by the fact that the pre-diatreme erosion surface in the Santa Rosa area is preserved below ~100 m of outflow deposits (Fig. 3) and by the diatreme size.

The north-south-trending longitudinal fault, mentioned above, was probably already active during the Triassic to Jurassic, at the time of deposition of the Pucará Group, as supported by the fact that the its thickness is different on opposite sides of the longitudinal fault (3,000 m in the eastern and 300 m in the western portions). The occurrence of the Upper Cretaceous to Eocene Shuco breccia and conglomerate, which belongs to the Pocobamba Formation and consists of Pucará clasts, along the longitudinal fault is additional evidence for the protracted tectonic activity of the longitudinal fault. A complex set of faults is prominent in the Pucará carbonate rocks in the Cerro de Pasco open pit. The first set strikes N 120° E, dips 70° to 80° S and is present in the eastern part of the open pit (Fig. 3). The second set strikes N 170° E, dips vertically, and is mainly present in the southern part of the deposit. The third fault set strikes N 35° E, dips 80° E, and is present in the northern open pit. The three fault sets are dextral and/or sinistral strike-slip faults and formed by compression in the later stages of folding.

### First Mineralization Stage

The large pyrite-quartz body (Fig. 3) is 1,800 m long and 150 m wide (in places up to 300 m) and has an elongated, vertically oriented funnel shape (Figs. 4, 5). Below the 1800 level (~550 m), the pyrite-quartz body is narrower and becomes a discontinuous sheath along the diatreme breccia-Excelsior shale contact. According to Lacy (1949), at greater depth (below 750 m), the pyrite-quartz body passes into the diatreme breccia and adjacent to the contact of a stock of quartz monzonite porphyry. To the west, the pyrite-quartz body has a steep contact to the diatreme breccia and replaces it (Fig. 3), whereas the eastern portion against the Pucará carbonate rocks is irregular, apparently reflecting different facies of the replaced carbonate rocks. Relict sedimentary textures of the Pucará carbonate rocks, as well as those of the breccia fabrics of the diatreme and of the vertical breccia bodies in the Pucará rocks, are locally recognizable in the replaced rock (Fig. 6B). Following the contour of the pyrite-quartz body and up

to a distance of 50 m, an alteration halo is present and is characterized by the assemblage muscovite-pyrite-quartz, typical of phyllic alteration (Fig. 6A).

In the following, sulfide minerals found in contact without showing reaction products are grouped as an “assemblage,” according to Barton et al. (1963). The symbol (-) joins minerals of a single assemblage that are in apparent equilibrium. The term “association” is used for all minerals appearing in a sample but not necessarily in contact or showing reaction borders. The symbol (+) joins minerals that are present everywhere in the association and the symbol (±) precedes minerals that are not always present or are rare.

A paragenetic sequence for the first stage of mineralization is presented in Figure 7, which integrates the observations of Einaudi (1968, 1977), Lacy (1949), and Bowditch (1935). Pyrite I (Fig. 7) constitutes 90 percent of the body, and black and red hematite-bearing chalcedony and quartz account for the remaining 10 percent. Pyrite I has a grain size of 500  $\mu\text{m}$  to 1 mm and contains minute pyrrhotite inclusions (Fig. 6C) and trace amounts of chalcopyrite and arsenopyrite. Lacy (1949) also reported stannite inclusions in pyrite I. Minute cracks have been observed within the pyrite grains. Table 2 lists the chemical composition of typical samples of the pyrite-quartz body.

Steep to vertical pipelike pyrrhotite bodies partly replaced the pyrite-quartz body along its entire vertical extent (Figs. 3, 4). These pyrrhotite pipes show an upward and outward zonation and are mineralized with the metal suite W-Sn-Cu-Zn-Pb (Fig. 8). The core zone, only observed at deep levels, is composed of the assemblage pyrrhotite-quartz-wolframite. The intermediate-level assemblage consists of pyrrhotite-sphalerite-chalcopyrite-stannite (Fig. 6E; Einaudi, 1977). The outer zone, which is present over the whole vertical extent of the pyrrhotite bodies and which includes the Zn-Pb ore, consists of the association pyrrhotite + Fe-rich sphalerite + arsenopyrite with minor marcasite, tennantite, chalcopyrite, chlorite, muscovite, siderite, and calcite (Fig. 6D). Sphalerite contains 10 to 23.9 mol percent FeS with larger variations along crystallographic growth zones (Einaudi, 1977; Baumgartner, 2007). The Zn-Pb ores, characterized by this Fe-rich sphalerite and the presence of fine-grained (avg size around 50  $\mu\text{m}$ ) pyrite II and arsenopyrite, form extensive replacements of carbonate in the Pucará Group rocks (Fig. 3), with galena becoming increasingly important at the margins. The transition zone between the pyrrhotite pipes and the Zn-Pb ores consists of a fine-grained mixture of pyrite and marcasite resulting from the alteration of pyrrhotite (Fig. 6F). A typical ore composition of the pyrite-quartz body and the Zn-Pb ores is given in Table 2.

### Second Mineralization Stage Carbonate-Replacement Orebodies

#### *Morphology of the main orebodies*

The main zoned Zn-Pb-(Bi-Ag-Cu) carbonate-replacement orebodies are Cuerpo Nuevo, Manto V, Cayac Noruega C, Rosita, Peggy, and Cola C.N.A and Cola C.N.B (Fig. 3). They comprise an important resource and have only recently become accessible. These bodies follow subvertical faults trending N 35° E, N 120° E, and N 170° E (Figs. 3, 9) and

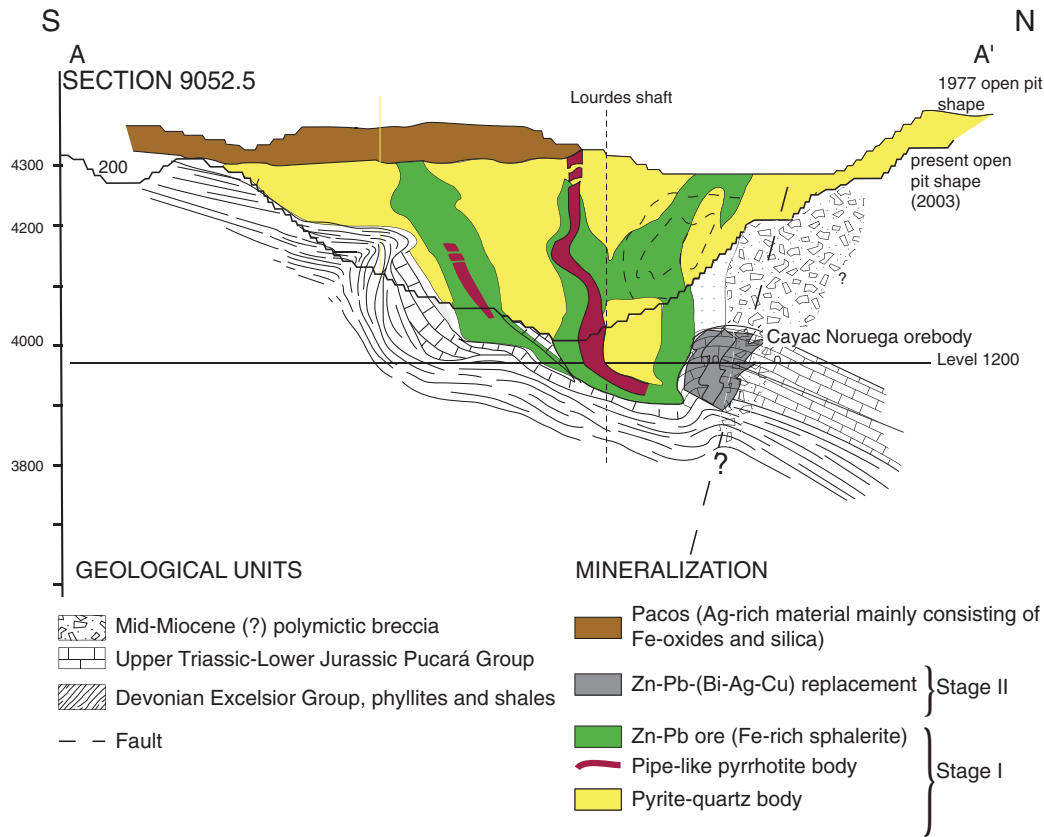


FIG. 4. A-A' north-south cross section (trace A-A' in Fig. 3), showing pipelike pyrrhotite bodies and related Zn-Pb ores from the first mineralization stage emplaced in the pyrite-quartz body and in the Triassic-Jurassic Pucará carbonate rocks, modified from Einaudi (1977). The second mineralization stage is also shown based on underground workings (contours absent in the section).

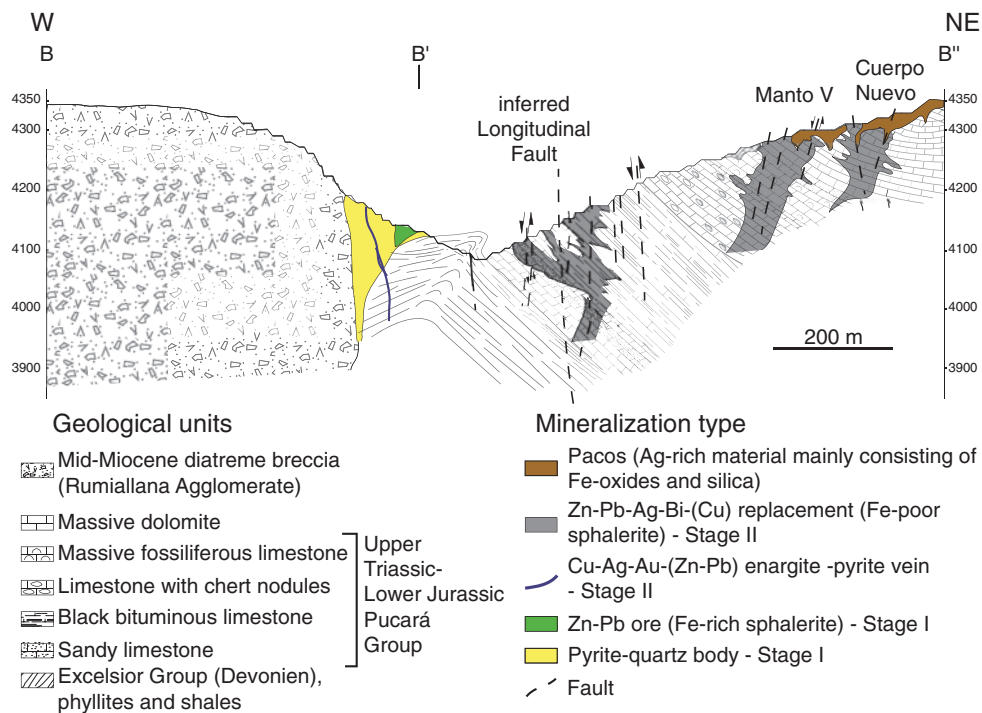


FIG. 5. B-B' cross section (trace in Fig. 3) through the diatreme and the first mineralization stage (including the pyrite-quartz body and the Zn-Pb ores), and the second stage of enargite-pyrite veins in the diatreme breccia plus replacement orebodies hosted in Pucará carbonate rocks. Note that the second mineralization stage orebodies are controlled by faults.

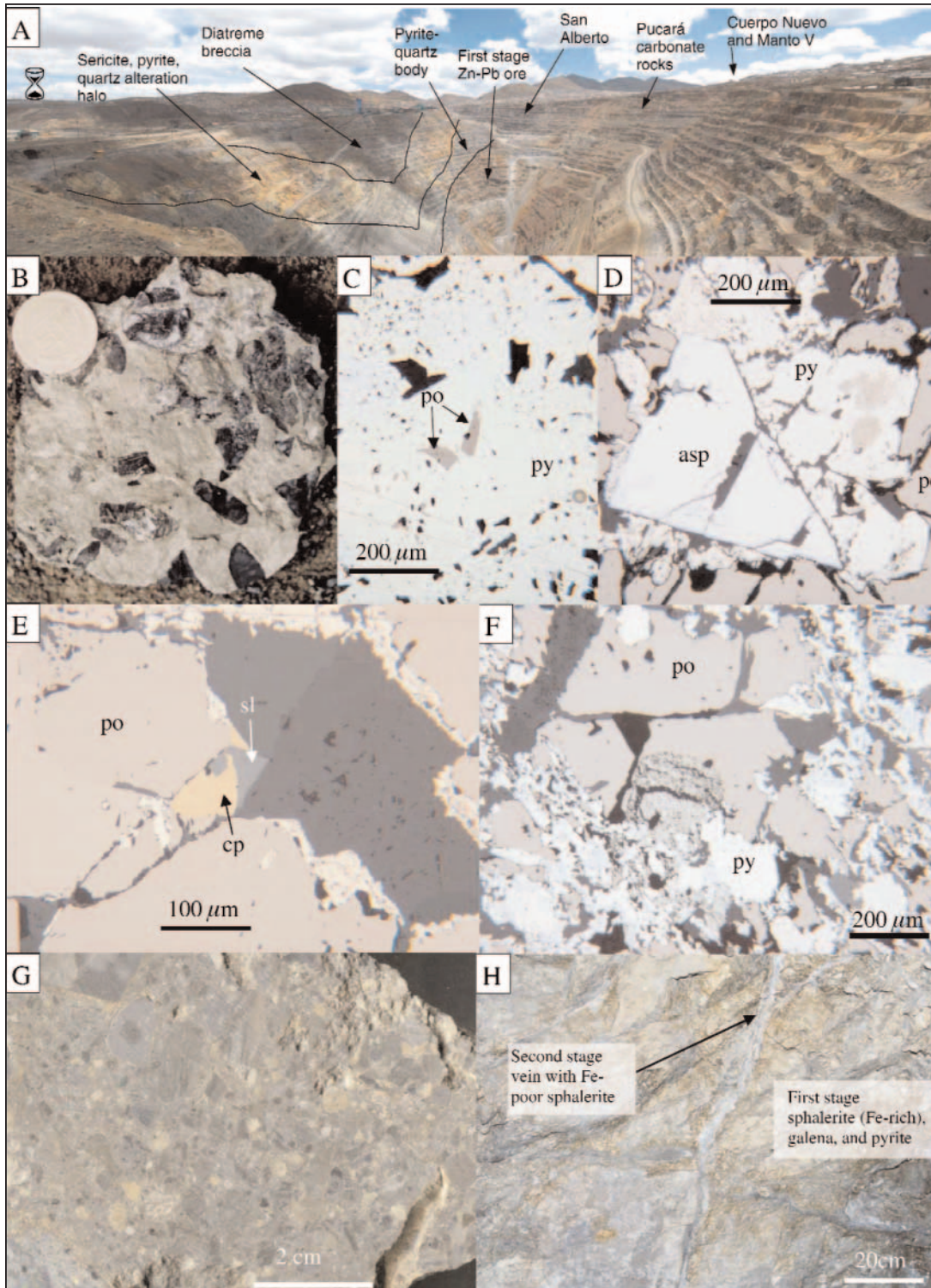


FIG. 6. A. View of the Cerro de Pasco open pit looking north. The important features have been outlined. B. Sample of the diatreme breccia partly replaced by the pyrite-quartz body. C. Photomicrograph showing pyrite I with pyrrhotite blebs (plain-polarized reflected light, CPR 433). D. Association of pyrrhotite with arsenopyrite and pyrite (plain-polarized reflected light, fpe-131-3). E. Deep- to intermediate-level association of pyrrhotite, chalcopyrite, and sphalerite occurring in the pipelike pyrrhotite bodies (plain-polarized reflected light, fpe-131-3). F. Pyrite replacing pyrrhotite, in part showing bird's eye texture (plain-polarized reflected light, fpe-136-9). G. Breccia (probably fluid-escape breccia) from the San Alberto area consisting of angular and subangular clasts of different facies of the Pucará Group rocks with a rock-flour matrix of the same composition (CPR 99). H. Example of a second-stage vein crosscutting the first-stage Zn-Pb mineralization related to pyrrhotite in the central part of the open pit, 1200 level, S920-E, 9860-N. Abbreviations: asp = arsenopyrite, cp = chalcopyrite, po = pyrrhotite, py = pyrite, sl = sphalerite.

FIRST MINERALIZATION STAGE

		Assemblages or associations typical for a zone			
		pyrrhotite - quartz - wolframite	pyrrhotite - sphalerite - chalcopyrite - stannite	pyrrhotite + sphalerite + arsenopyrite + pyrite + chalcopyrite	sphalerite + arsenopyrite + pyrite + chalcopyrite + pyrrhotite
zone minerals	pyrite-quartz body	pipe-like pyrrhotite bodies			Zn-Pb ore
pyrite I	—————			—————	—————
pyrite II	—————			—————	—————
pyrrhotite	— — —	—————	—————	—————	— — —
wolframite		— · · · ·			— — —
cassiterite		—			
ilmenite		—			
chalcopyrite	— · ·		— — —	— — —	— — —
sphalerite			— — —	—————	—————
stannite	— · ·		— · · · ·	—————	—————
arsenopyrite	— · ·		— · ·	—————	— — —
galena					—————
tetrahedrite-tennantite					— · · · ·
magnetite					— · · · ·
argentite					— · ·
polybasite					— · ·
quartz	—————	—————	—————		—————
chlorite					— — —
sericite	— — —				— — —
siderite					— — —
calcite					— — —
mol% FeS in sphalerite			23.9-10.0 mol % FeS		

Key	Minerals present in the association
—————	Major, ubiquitous
— · · · ·	Common
— · ·	Uncommon
— · · · ·	Local, in minor amounts
—	Rare

FIG. 7. Paragenetic sequence for the first stage of mineralization (including observations of Bowditch, 1935, Lacy, 1949, and Einaudi, 1968, 1977). Pyrite generations according to Lacy (1949). Pyrite I is coarse grained ( $>500 \mu\text{m}$ ); pyrite II is fine grained ( $\sim 50 \mu\text{m}$ ). This sequence reflects the evolution of a fluid in time and space; therefore, minerals precipitating in the outer zones (right part of the diagram) may be contemporaneous with other minerals in the inner zones (left part of the diagram).

TABLE 2. Selected Whole-Rock Analyses of Mineralized Samples from the Second-Stage Replacement Orebodies Hosted in Pucará Carbonate Rocks and from Western Enargite Veins Hosted by the Diatreme Breccia, Cerro de Pasco

Zone	Sample no.	Location	Au (ppb)	Ag (ppm)	Bi (ppm)	Sb (ppm)	Cu (ppm)	As (ppm)	Sn (ppm)	Zn (%)	Pb (%)
Carbonate-replacement bodies											
Core	cpr 149	N-9964, E-9575, 4320m	b.d.l.	184	2385	31200	48018	4280	b.d.l.	0.8	1.3
Intermediate	cpr 82	CP-00-108 (34.00m)	b.d.l.	29100	10100	56600	77200	3200	b.d.l.	1.16	0.38
Outer (close to intermediate)	cpr 77	CP-00-108 (13.00m)	b.d.l.	348	b.d.l.	473	262	1250	b.d.l.	3.75	b.d.l.
Outer	cpr 76	CP-00-108 (9.70m)	b.d.l.	150	b.d.l.	110	480	1090	b.d.l.	45	5.95
Outermost	cpr 89	CP-00-108 (74.70m)	b.d.l.	5	b.d.l.	101	22	33	b.d.l.	2.6	0.25
Western enargite-pyrite veins											
Core zone	cpr 109	W open pit	416	186	267	5860	>99999	43100	b.d.l.	0.38	0.02
Core zone	cpr 124	W open pit	b.d.l.	103	14	7750	>99999	49700	b.d.l.	0.08	0.1
Core zone	cpr 135	W open pit	2960	81.2	49	795	8674	2670	b.d.l.	0	0.03
Intermediate	cpr 137	W open pit	11500	216	761	20300	>99999	10500	b.d.l.	0.18	0.15
Intermediate	cpr 139	W open pit	16200	216	268	11000	76404	27300	b.d.l.	0.13	0.03

Notes: All samples were analyzed with ICP + INNA except samples cpr 82 and 76, which were analyzed with XRF; analytical methods: XRF = X-ray fluorescence spectroscopy; INNA = instrumental neutron activation analysis; ICP = "near total" digestion ICP-MS; b.d.l. = below detection limits

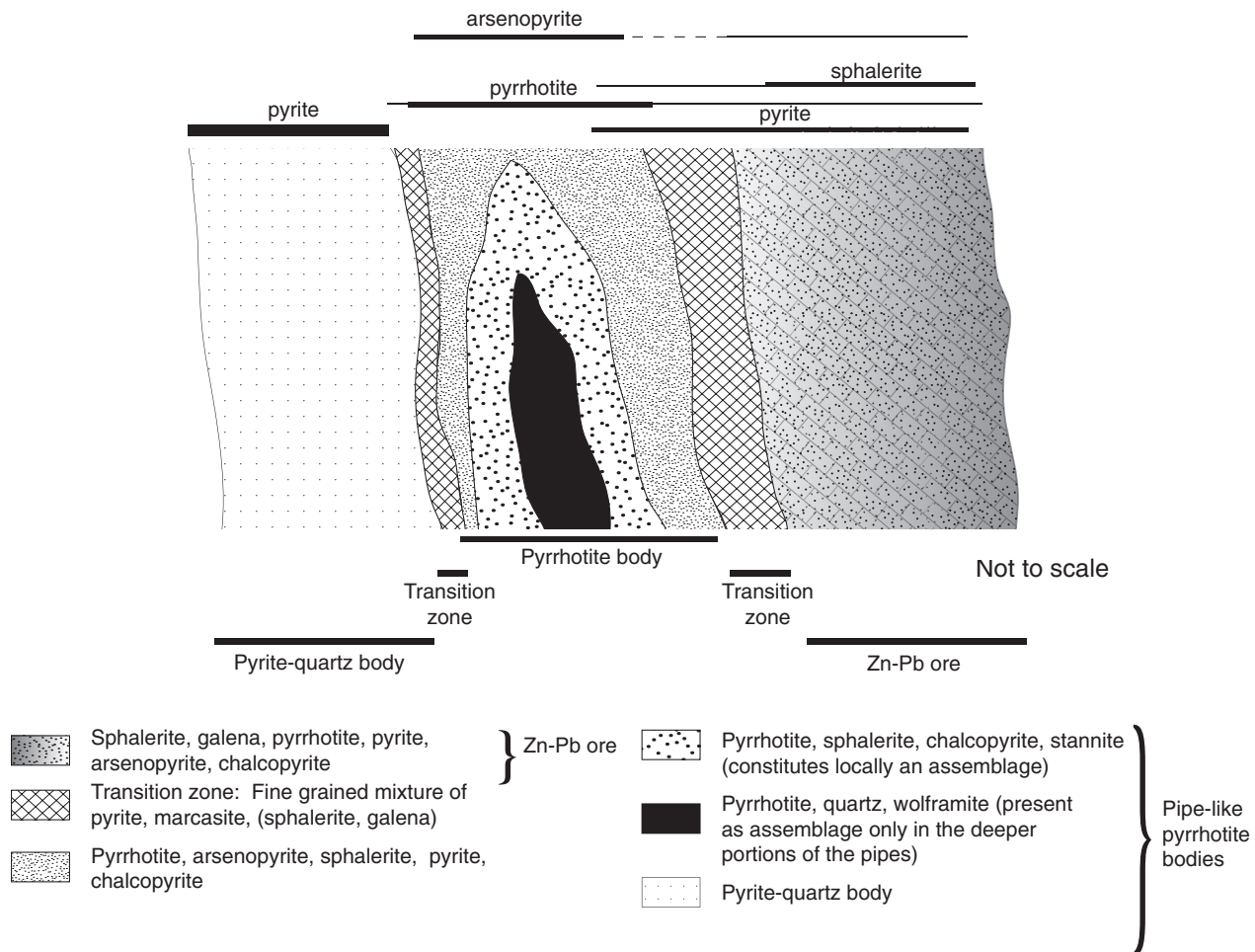


FIG. 8. Schematic zoning of pipe-like pyrrhotite bodies and related Zn-Pb ores from the first mineralization stage, based on Einaudi (1977) and this study.

locally favorable Pucará beds, mainly dolo-arenite horizons. The carbonate-replacement orebodies have an irregular upward-flaring pipe-like shape with a diameter ranging from 50 cm to 50 m (Figs. 9, 10, 11). Most of these bodies show an inclined plunge (between 25° and 60°) in the direction of the diatreme-dome complex. The morphologies and sizes of the main orebodies are listed in Table 3. The Matagente area contains two main orebodies, Cuerpo Nuevo and Manto V, as well as two smaller ones, Peggy and Rosita (Fig. 3). The Cayac Noruega body is located in the central part of the open pit (Fig. 3).

The San Alberto orebody, located in the northern open pit, is hosted by an elongated northeast-southwest, subvertical body breccia consisting of angular and subangular clasts of Pucará Group rocks, up to 5 cm in size, with a rock-flour matrix of the same composition (Fig. 6G). The breccia is recognized to extend from the bench 4350 to 4100 and crosscuts bedding. In the benches of level 4200 and deeper, the breccia contains, in addition to Pucará carbonate fragments, clasts of Excelsior Group phyllite. This breccia is probably related to fluid escape controlled by faults following a N 35° E direction.

The Uliachín and El Pilar orebodies, located 500 m south and 200 m east of the open pit, respectively (Fig. 3), also

belong to the second-stage carbonate-replacement orebodies and have been mined since ancient times.

#### Mineral zoning

The orebodies replacing carbonate rocks show a well-developed lateral and vertical zoning (Fig. 12). (1) A core zone comprises the assemblage fanatinite-pyrite accompanied by alunite. It is surrounded by (2) an intermediate zone with the assemblage pyrite-tetrahedrite + bismuthinite-stibnite solid solution with kaolinite and aluminum phosphate sulfate (APS) minerals such as hinsdalite and (3) an outer Zn-Pb-rich zone with the association pyrite + sphalerite + galena, accompanied by kaolinite and quartz. (4) The outermost zone is characterized by Fe-Mn-Zn-Ca-Mg carbonates + hematite + magnetite. The best developed zones are the intermediate pyrite-tetrahedrite + Bi mineral zone and the outer sphalerite + galena zone, which are economic, whereas the core zone is only weakly developed and in part absent.

This zoning is typical for all orebodies in the Cerro de Pasco pit except the breccia-hosted San Alberto orebody, where only the outer Zn-Pb and the outermost zones are recognized. Figure 13 shows a paragenetic sequence for each zone. This sequence must be viewed as the evolution of a

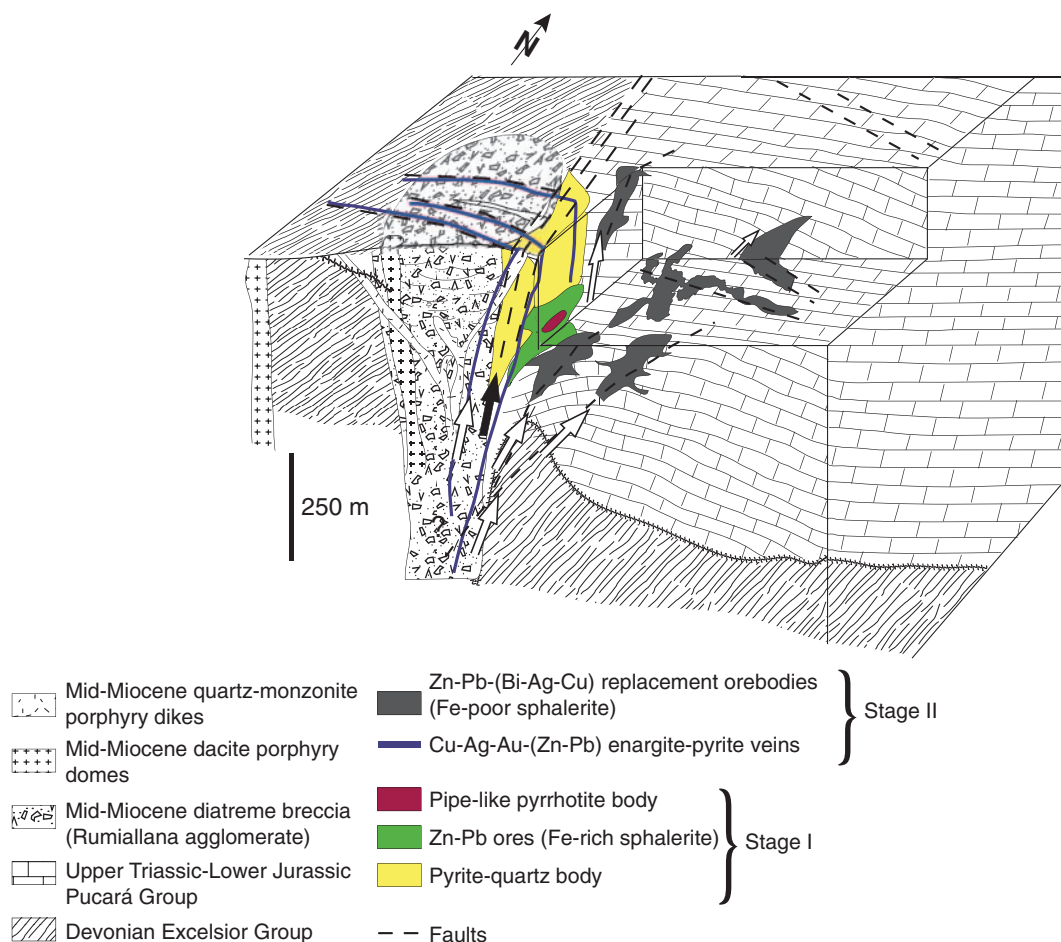


FIG. 9. Three-dimensional block diagram, showing the Cerro de Pasco deposit with possible fluid path for the two mineralizing events. Black arrow is for the first mineralization stage, mainly following the north-south structures, and white arrow is for the second mineralization stage. The fluids for the enargite-pyrite veins followed east-west structures, whereas the fluids responsible for the carbonate-replacement orebodies followed structures along the N 35° E, N 120° E, and N 170° E faults.

fluid in time and space; therefore, minerals precipitating in the outer zones (right part of the diagram) may be contemporaneous with other minerals in the inner zones (left part of the diagram). Table 4 lists the chemical formulas of uncommon sulfosalts present at Cerro de Pasco.

**Core zone (famatinite-pyrite):** The core zone is generally less than 5 to 20 cm wide and has been observed at the 4320 bench outcrop in the Cuerpo Nuevo orebody, in the Cayac Noruega, and Manto V orebodies. Cuerpo Nuevo consists of a well-zoned replacement body. The bulk rock texture is fine grained (150  $\mu\text{m}$ ) and friable, showing a grayish color. The sulfide assemblage in the core consists of famatinite-pyrite. Famatinite occurs as subidiomorphic roundish grains (avg 100  $\mu\text{m}$  diam), in part showing crystallographic faces and commonly replaced and overgrown by tetrahedrite-tennantite (Fig. 14D). Locally, tetrahedrite grains contain relics of famatinite, suggesting that the replacement of famatinite by tetrahedrite was nearly complete. Famatinite is close to stoichiometric, with arsenic contents less than 5 wt percent (Table 5). Pyrite occurs as euhedral grains, which average 80 to 200  $\mu\text{m}$  in diameter, and is in direct contact with famatinite and does not show any reaction rim. Late fine-grained (<20  $\mu\text{m}$ ) pyrite

is present, generally disseminated within kaolinite. In the core zone, Cu grades in hand specimens are up to 1 wt percent and locally up to 4.8 wt percent (Table 2).

Alunite, quartz, and kaolinite occur in the core zone; alunite is present as small idiomorphic crystals (10–40  $\mu\text{m}$ ) within famatinite and tetrahedrite (Fig. 14B, E). Quartz occurs as idiomorphic crystals, commonly within pyrite (20–60  $\mu\text{m}$ ; Fig. 14C). The presence of abundant kaolinite (10–30 vol % of the rock) is responsible for the rock being friable.

The core zone overprints an early quartz and pyrite assemblage which was deposited along the N 120° E and N 170° E faults present in the open pit (Fig. 3). Quartz occurs as euhedral grains with an average size of ~100  $\mu\text{m}$ , and pyrite occurs as subhedral to euhedral grains (up to 100  $\mu\text{m}$ ). Locally, pyrite contains rare inclusions of pyrrhotite (up to 20  $\mu\text{m}$ ), which could be part of the first stage. The quartz-pyrite assemblage appears to shield the vein walls and thereby may have promoted the development of a high-sulfidation assemblage in the core zone.

**Intermediate zone (tetrahedrite-pyrite + Bi minerals):** The transition between the core and the intermediate zones is gradual and is marked by the assemblage pyrite-tetrahedrite

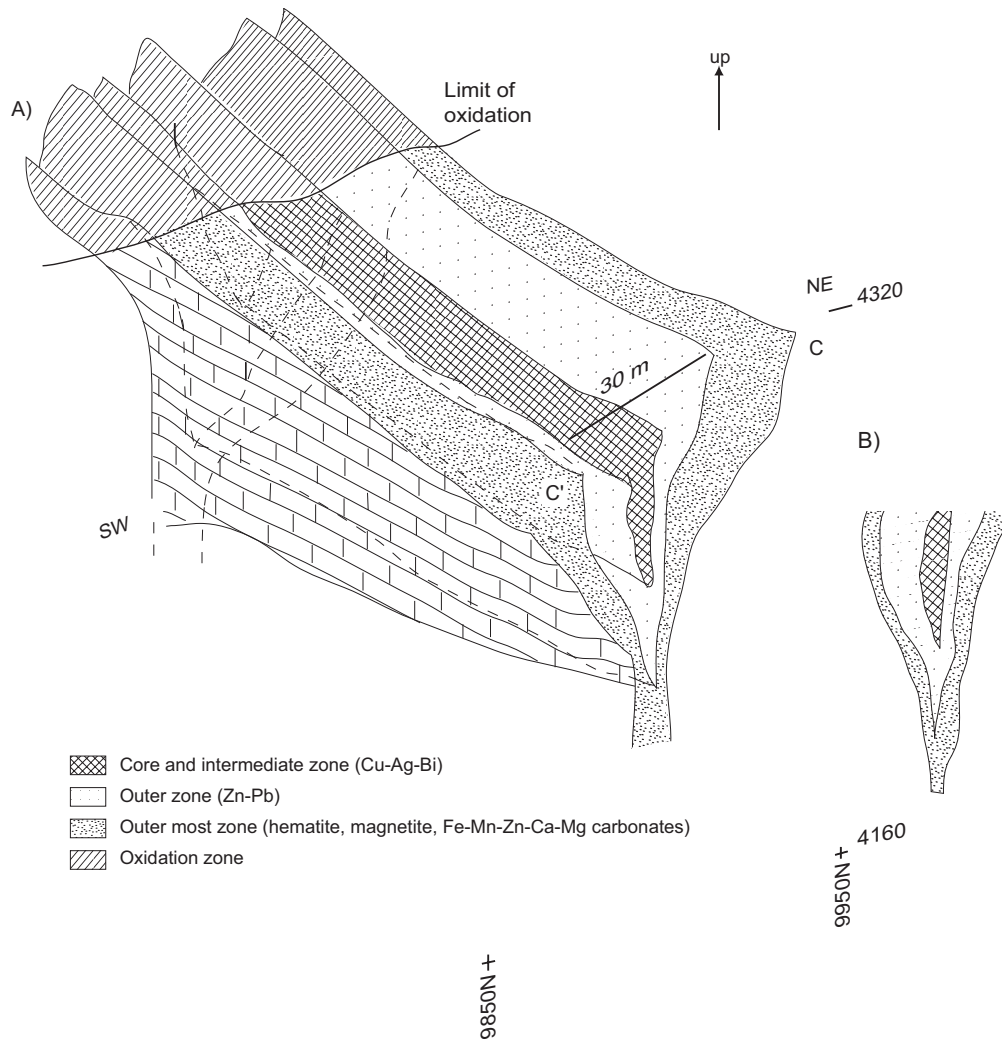


FIG. 10. Three-dimensional view of the Manto V orebody. The body has an upward-flaring pipelike shape as shown in the scheme B. Above 4,320 m, the body is oxidized to an Ag-rich material consisting mainly of Fe oxides and silica (pacos).

+ Bi minerals (Fig. 13). The intermediate zone has been observed in drill hole CP-00-108 and in the 4320 bench at Cuerpo Nuevo. The ore contains abundant pyrite (5–40 vol %) and kaolinite and/or dickite (5–50 vol %) and has a friable texture. The rock is generally fine grained (150–200  $\mu\text{m}$ ) but,

locally, pyrite and tetrahedrite are visible at macroscopic scale (rarely up to 1–2 mm; Fig. 14A). Grades in the intermediate zone can locally reach up to 2,000 g/t Ag, up to 1 wt percent Bi, up to 7 wt percent Cu, up to 5 wt percent Sb, up to 1 wt percent Zn, and up to 0.4 wt percent Pb (Table 2).

TABLE 3. Morphology Characteristics of the Second Mineralization Stage Main Orebodies at Cerro de Pasco

Orebodies	Trend	Plunge	Size (m)	Minimum down-plunge distance (m)	Zonation	Host rock
Matagente area						
Cuerpo Nuevo	N 120° E	60° S	400 × 100	400	Yes	Pucará carbonate
Manto V	E-W, N 60° W	30° W	500 × 80	160	Yes	Pucará carbonate
Diamante area						
Cayac Noruega	N 170° E	55° S	50 × 50	110	Yes	Pucará carbonate
San Alberto	N 35° E	50° SW	30 × 50	200	No	Breccia
East-west enargite-pyrite veins						
Central and north open pit	N 70°–90° E, N 120° E	80°–90° S, 80°–90° N	2 × 500	760	Yes	Diatreme breccia and pyrite-quartz body
Southern part	N 60°–70° E, E-W	80°–90° N			Yes	Excelsior phyllite

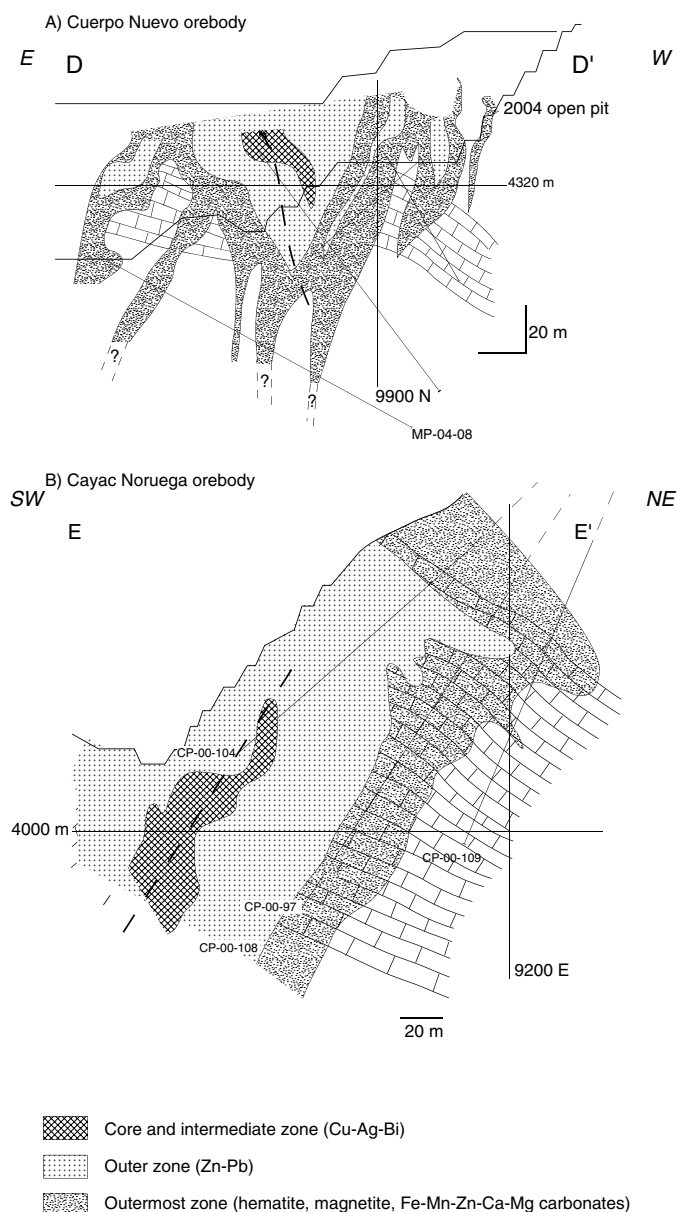


FIG. 11. A. Northeast-southwest cross section (D-D'), showing the geometry of zonation in the Cuerpo Nuevo orebody. Note that the lower part is unknown but appears to continue downdip of the body. Core and intermediate zones have been merged (drawn from surface and drill hole data). B. Northeast-southwest cross section (E-E') on the Cayac Noruega replacement orebody in the central part of the open pit (drawn from surface and drill hole data).

The main Ag-Bi-Cu sulfosalts include tetrahedrite, cuprobismutite, bismuthinite-stibnite solid solution series, matildite, emplectite, and chalcocopyrite. Tetrahedrite grains containing relicts of famatinite suggest nearly complete replacement of famatinite by tetrahedrite (Fig. 14E). In addition, single grains commonly show oscillatory As-Sb zoning, the cores being richer in Sb (Fig. 16A). Electron microprobe analyses indicate two populations of tetrahedrite (Fig. 15). Tetrahedrite replacing famatinite (Fig. 16C) falls in the compositional field of tetrahedrite (Nickel, 1992), whereas the other population falls in the field of tetrahedrite-tennantite

and Bi-bearing tetrahedrite. The latter occurs always in the presence of bismuth minerals. Copper contents in tetrahedrite range from 34 to 43 wt percent, Sb contents are 0.36 to 28.4 wt percent, and As contents are 0.79 to 9.8 wt percent (Table 5). On average, tetrahedrite contains 8 wt percent Bi (up to 18 wt %), 4 wt percent Zn, and 2 wt percent Fe (Table 5). Grains with bismuthinite-stibnite solid solution series occur as laths and, under crossed polars, are strongly anisotropic in reflected light.  $Sb_2S_3$  contents are between 16 and 26 wt percent. At the margin of grains of bismuthinite-stibnite solid solution, where it is replaced by tetrahedrite, a thin rim ( $<4 \mu\text{m}$ ) of an unknown mineral occurs (Fig. 16B). Emplectite ( $\sim 100 \mu\text{m}$ ) is greenish in plane-polarized reflected light, is generally replaced by cuprobismutite, and contains an average of 61.8 wt percent Bi and 19.9 wt percent Cu (Table 5). Cuprobismutite (up to 200  $\mu\text{m}$ ) occurs as laths and is characterized by a strong bright white color in reflected light. Cuprobismutite contains 65 wt percent Bi, 12 wt percent Cu, and between 2.9 and 4.7 wt percent Ag (Table 5). In places matildite forms an outer rim (5–10  $\mu\text{m}$ ) of bismuthinite-stibnite solid solutions, the whole being surrounded by tetrahedrite. Matildite is also present as xenomorphic grains within tetrahedrite; the xenomorphic grains average 50  $\mu\text{m}$  in diameter (Fig. 16D) and are close to stoichiometric in composition, with 54.8 wt percent Bi, 28 wt percent Ag, and 16.5 wt percent S (Table 5). Chalcocopyrite occurs in the tetrahedrite as small blebs (50–70  $\mu\text{m}$ ) and occurs locally with covellite. Traces of covellite replace along fractures most Cu-bearing minerals.

Additional sulfides that occur in the intermediate zone are minor antimonpearceite, colusite, and sphalerite. Antimonpearceite is present as inclusions (40–50  $\mu\text{m}$  diam) in tetrahedrite (Fig. 16D). Antimonpearceite contains between 64.8 and 67 wt percent Ag, 6.6 to 8 wt percent Cu, 5 to 7 wt percent Sb (one sample as low as 2 wt % Sb; Table 5), and between 1 and 2 wt percent As. Bismuth contents reach up to 4.8 wt percent (one sample up to 7.3 wt %, Table 5). Colusite was found in two samples as small crystals (50  $\mu\text{m}$ ) adjacent to tetrahedrite and lacks replacement textures. It is thus considered that pyrite-tetrahedrite-colusite is an equilibrium assemblage (Fig. 16E). Late pyrite occurs with kaolinite as small euhedral grains (10  $\mu\text{m}$ ) and cements brecciated sphalerite (Fig. 16F). Sphalerite compositions range from 0.1 to 4 mol percent FeS, although the average value is  $\sim 1$  mol percent.

Kaolinite, quartz, alunite, and hinsdalite, an aluminum phosphate sulfate (APS) mineral (Fig. 17A) occur in the intermediate zone. Alunite gives way to hinsdalite from the core to the intermediate zone. Hinsdalite and alunite occur locally as small euhedral grains (10  $\mu\text{m}$ ) within colusite. Barite is also present in the intermediate zone. Kaolinite and APS mineral contents vary in this zone from 5 to 50 vol percent. APS minerals normally have Sr contents between 5.5 to 7.4 wt percent, Pb contents of 6.4 to 8.4 wt percent, and Ca contents between 2.4 and 2.7 wt percent. Quartz occurs as euhedral grains in pyrite.

*Outer zone (sphalerite + galena + pyrite  $\pm$  Ag sulfosalts):* The transitions from core to intermediate zone and outer zone are gradual. The outer zone consists of a friable sphalerite-bearing material, and near the outermost zone it becomes

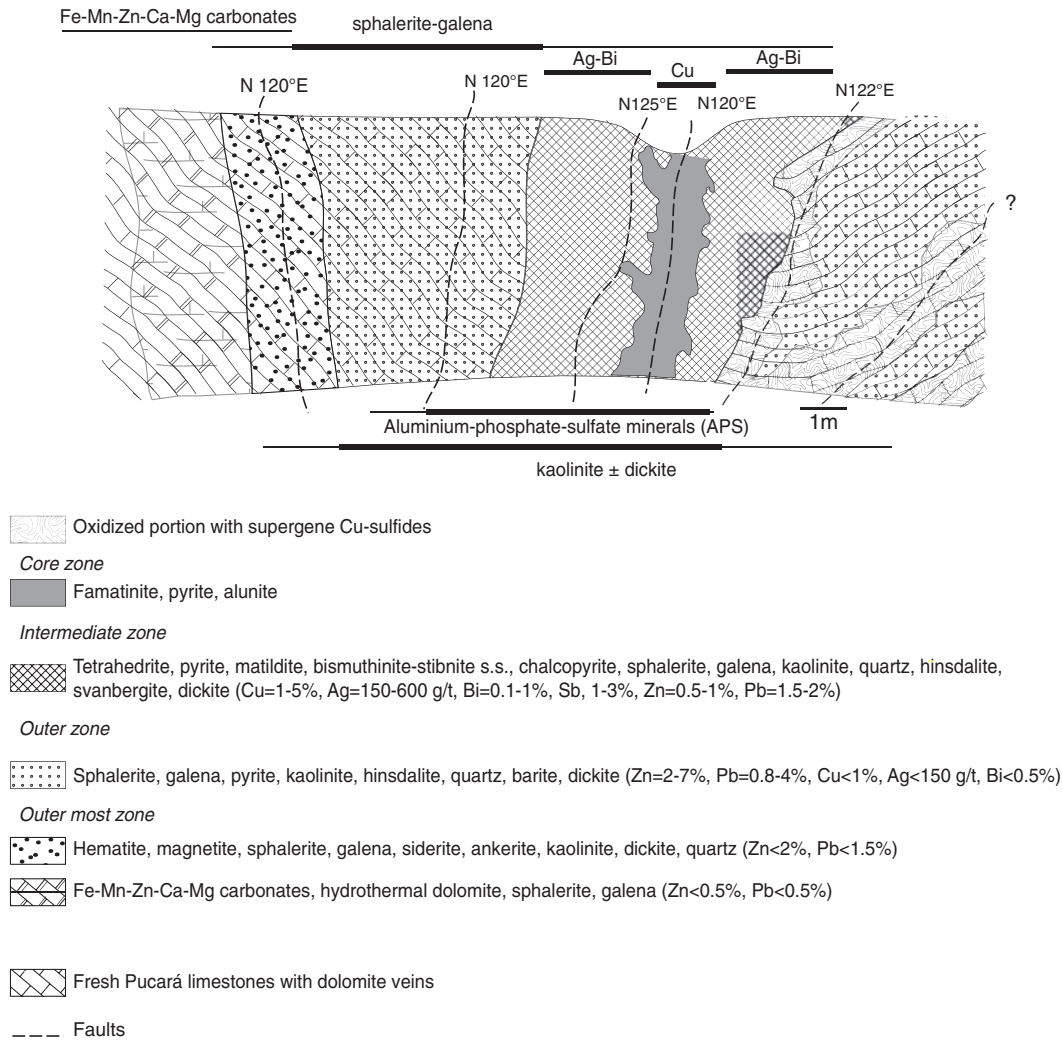


FIG. 12. Idealized zonation based on mapping of the 4320 bench and drill hole (CP-00-108) descriptions (modified from Baumgartner et al., 2003). For whole-rock analyses of typical mineralized samples (see Table 2).

TABLE 4. Chemical Formula of Uncommon Sulfosalts and Gangue Minerals Present at Cerro de Pasco

Minerals	Chemical formula
<b>Major ore minerals</b>	
Famatinite	$\text{Cu}_3\text{SbS}_4$
Tetrahedrite	$(\text{Cu}, \text{Fe})_{12}\text{Sb}_4\text{S}_{13}$
Bi tetrahedrite-tennantite	$(\text{Cu}, \text{Fe}, \text{Bi}, \text{Zn}, \text{Ag})_{12}(\text{Sb}, \text{As})_4\text{S}_{13}$
Bismuthinite-stibnite solid solution series <sup>1</sup>	$(\text{Bi}, \text{Sb})\text{S}_2$
Cuprobismutite	$\text{Cu}_{10}\text{Bi}_{12}\text{S}_{23}$
<b>Subordinate ore minerals</b>	
Matildite	$\text{AgBiS}_2$
Emplectite	$\text{CuBiS}_2$
Antimonpearcite	$(\text{Ag}, \text{Cu})(\text{Sb}, \text{As})_2\text{S}_{11}$
Colusite	$\text{Cu}_{26}\text{V}_2(\text{As}, \text{Sn}, \text{Sb})\text{S}_{32}$
Proustite	$\text{Ag}_3\text{AsS}_3$
Jordanite	$\text{Pb}_{14}(\text{As}, \text{Sb})_6\text{S}_{23}$
<b>Gangue minerals</b>	
Alunite	$\text{KAl}_3(\text{SO}_4)_2(\text{OH})_6$
Hinsdalite	$(\text{Pb}, \text{Sr})\text{Al}_3(\text{PO}_4)(\text{SO}_4)(\text{OH})_6$
Svanbergite	$(\text{SrAl}_3(\text{PO}_4)(\text{SO}_4)(\text{OH})_6)$

<sup>1</sup> Bi content: 64.3-69.0%,  $\text{Bi}_2\text{S}_2$  between 73.6 and 83.2

more massive. Sphalerite is light brown or colorless and occurs mainly as small grains (avg 50  $\mu\text{m}$  to 1 mm, rarely up to 2 mm in size). FeS contents in sphalerite are low, from 0.01 to 3.5 mol percent. In the intermediate to outer zones the average FeS content in sphalerite is less than 2 mol percent, whereas in the outermost zone it is slightly higher (up to 4.7 mol %).

Galena is also present (50  $\mu\text{m}$  to 1 mm, up to 5 mm in size) and generally replaces, or less commonly is replaced by, sphalerite. Locally, it overgrows sphalerite and pyrite. Whole-rock analyses of typical ore indicate Zn contents up to 45 wt percent, Pb up to 6 wt percent, and Ag up to 300 ppm (Table 2).

Where Ag sulfosalts are present, they occur near the contact with the intermediate zone and only in minor amounts. Silver and Pb sulfosalts, such as proustite and jordanite, are present as ~50- to ~30- $\mu\text{m}$  inclusions in galena replacing pyrite (Fig. 17B). Sphalerite abundance diminishes through the outer to the outermost zone, and galena is the main constituent of massive galena-bearing ores on the external margins of the outer zone. Hinsdalite and svanbergite abundances

SECOND MINERALIZATION STAGE IN CARBONATE REPLACEMENT BODIES

		Assemblages or associations typical for a zone			
		famatinite-pyrite	pyrite-tetrahedrite + Bi-minerals	pyrite + galena + sphalerite	hematite+magnetite+ Mn-Fe-Zn
Zone	Early quartz and pyrite	Core zone	Intermediate zone	Outer zone	Outer most zone
Minerals					
pyrrhotite	---	---			
pyrite	---	---	---	---	---
famatinite		---	---		
tetrahedrite			---		
Bi <sub>2</sub> S <sub>3</sub> -Sb <sub>2</sub> S <sub>3</sub> ss.			---		
antimonpearcite			---		
colusite			---		
cuprobismuthite			---		
emplectite			---		
chalcopyrite			---		
sphalerite			---	---	
matildite			---	---	
galena			---	---	
proustite				---	
jordanite				---	
stephanite				---	
magnetite					---
hematite					---
quartz	---	---	---	---	
carbonates				---	---
kaolinite		---	---	---	---
hinsdalite		---	---	---	
alunite		---	---	---	
woodhouseite			---		
svanbergite			---		
barite			---		
mole% FeS in sphalerite			0-2.5 mole % FeS	0-3 mole % FeS	0-6.5 mole % FeS

Key Minerals present in the association  
 Major, ubiquitous  
 Common  
 Uncommon  
 Local, in minor amounts  
 Rare

FIG. 13. Paragenetic sequence of the Cordilleran base metal replacement orebodies. This sequence reflects the evolution of a fluid in time and space; therefore, minerals precipitating in the outer zones (right part of the diagram) may be contemporaneous with other minerals in the inner zones (left part of the diagram).

decrease from the intermediate to the outer zone. Kaolinite is abundant in the outer zone and is responsible for the friable texture of the Zn-Pb ore.

**Outermost zone (magnetite + hematite + Fe-Mn-Zn-Ca-Mg carbonates):** The outermost zone contains magnetite, hematite (typically blades of 50–100 μm length), and, adjacent to Pucará limestones, Fe-Mn-Zn-Ca-Mg carbonates and hydrothermal dolomite. Sphalerite and galena are subordinate and constitute less than 2 vol percent of the outer zone. These minerals occur intergrown with hematite and magnetite grains (up to 100 μm in size) and, rarely, with Fe-Mn-Zn-Ca-Mg carbonates. Sphalerite has a slightly higher FeS content than in the outer zone (up to 4.7 mol %). Textural relationships between hematite and magnetite are complex. Locally, hematite is replaced by magnetite and subsequently replaced by pyrite

(Fig. 17C-D). Late euhedral pyrite occurs with Fe-Mn-Zn-Ca-Mg carbonates. The external margins of the outermost zone locally consist of massive Fe-Mn-Zn-Ca-Mg carbonates, typically (Fe<sub>0.4-0.9</sub>, Mn<sub>0.1-0.4</sub>, Zn<sub>0.1-0.25</sub>, Ca<sub>0.01-0.09</sub>, Mg<sub>0.01-0.018</sub>) CO<sub>3</sub>, that are easily recognized in the field because of their high specific gravity. These carbonate minerals contain euhedral pyrite grains that are up to 50 μm in size.

Second Mineralization Stage Enargite-Pyrite Veins

Enargite-pyrite veins in the western part of the deposit

The irregular, up to 2-m-wide Cu-Ag-Au-(Zn-Pb) veins in the western part of the deposit strike N 70–90° E and dip steeply to the south in the central and northern parts of the open pit and strike N 120° E with steep dips to the north in

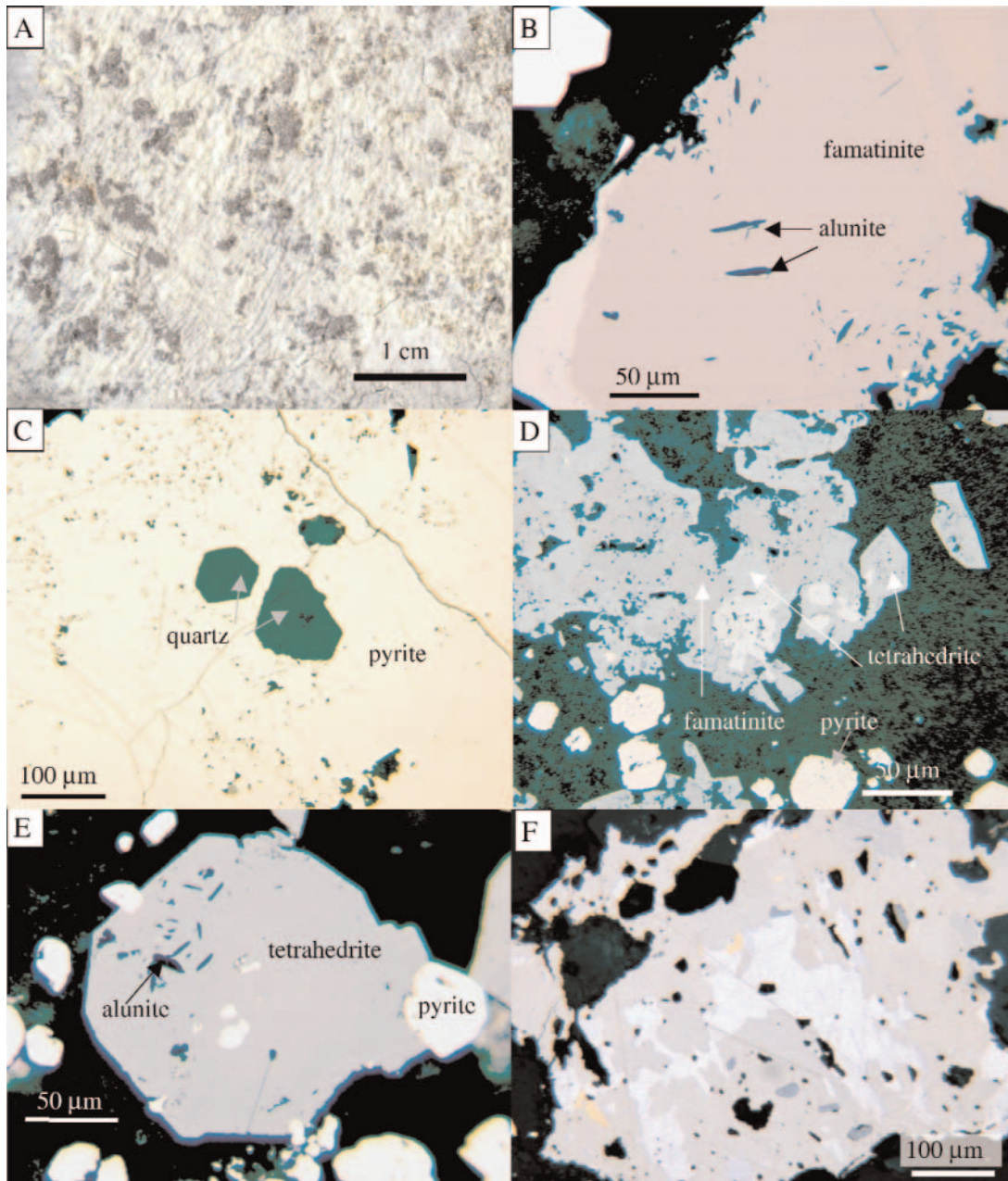


FIG. 14. A. Hand specimen of the intermediate zone with abundant kaolinite and tetrahedrite (CPR 82). B-E. Typical views of the Cu-rich core and the Ag-Bi-rich intermediate zone in reflected light (plane-polarized light, except where noted otherwise). B. Idiomorphic alunite within famatinite, Cuerpo Nuevo, oil immersion, CPR 149. C. Idiomorphic quartz within early pyrite, Diamante, CPR 84. D. Tetrahedrite as subidiomorphic overgrowth on famatinite and partly as replacement, Cuerpo Nuevo, CPR 149. E. Idiomorphic alunite within pseudomorphic tetrahedrite after famatinite, oil immersion, CPR 149, Cuerpo Nuevo. F. Emplectite (gray), bismuthinite-stibnite (white), and chalcopyrite (yellow). Note the presence of supergene covellite (CPR81).

its southern part (Fig. 18). They are anamostosing veins with a maximum strike length of 500 m and extend to a depth of at least 760 m (Fig. 18). The veins are mainly hosted by the diatreme breccia. Where they enter the adjacent pyrite-quartz body, they form horsetails which terminate to the east before entering the carbonate rocks (Fig. 3). In places, they crosscut the Zn-Pb ores of the first mineralization stage. Ward (1961) reported that some veins in the footwall of "vein 43" were mined for enargite in their deeper levels and for

galena and sphalerite in their upper portions, suggesting a vertical zonation.

The veins individually show a less well-developed zonation than the carbonate-replacement orebodies and consist of an enargite-pyrite core, an intermediate zone of tennantite, stibnite, and Bi minerals, and a poorly developed outer zone with small amounts of Fe-poor sphalerite and galena. The best developed ore, the enargite-bearing zones, were exploited for copper until 1950. In the following, as well as in Figure 19,

TABLE 5. Electron Microprobe Analyses on Complex Sulfosalts from the Second-Stage Replacement Bodies and Veins

Mineral	Sample no.	S (wt %)	Fe (wt %)	Cu (wt %)	Zn (wt %)	As (wt %)	Ag (wt %)	Sn (wt %)	Sb (wt %)	Pb (wt %)	Bi (wt %)	Total
Core zone												
Famatinite (avg <i>n</i> = 3)	cpr 149	29.84	0.02	43.72	0.02	3.66	0.02	0.18	22.67	b.d.l.	0.03	100.13
Enargite	cpr 109	32.79	0.06	48.04	0.02	17.76	0.03	b.d.l.	0.49	n.a.	1.57	100.87
Luzonite	cpr 137	31.07	0.38	45.23	b.d.l.	11.76	0.03	n.a.	10.15	n.a.	0.03	98.74
Intermediate zone												
Tetraedrite	cpr 149	24.98	0.15	37.07	7.73	0.79	0.39	0.20	28.45	b.d.l.	b.d.l.	99.77
Bi tetrahedrite	cpr 149	23.29	1.22	36.91	6.82	2.67	1.38	0.14	22.97	b.d.l.	4.24	99.64
Tennantite	cpr 109	28.15	1.64	43.82	6.12	18.00	0.00	n.a.	2.33	b.d.l.	b.d.l.	100.08
Cuprobismutite	cpr 81	18.41	0.10	12.70	0.07	b.d.l.	3.30	0.00	0.34	b.d.l.	65.62	100.55
Emplectite	cpr 81	18.36	0.08	19.81	0.06	b.d.l.	0.12	0.00	0.14	b.d.l.	62.07	100.68
Matildite	cpr 82	16.55	0.09	1.25	0.15	b.d.l.	27.90	0.00	0.00	b.d.l.	54.65	100.59
Antimonpearcite	cpr 82	15.07	0.05	7.77	0.14	0.65	65.70	0.00	7.54	b.d.l.	3.38	100.31
Bismutinite-stibnite ss. series	cpr 149	20.27	0.04	0.52	0.11	b.d.l.	0.07	0.15	11.20	b.d.l.	67.95	100.31
Proustite (avg <i>n</i> = 3)	cpr 77	18.02	0.07	0.12	0.46	12.73	64.99	0.00	0.66	b.d.l.	b.d.l.	97.00

Notes: b.d.l. = below detection limits, Cd was always below detection limits, n.a. = not analyzed

observations on veins 25, 43, 44, and 79 (Fig. 3) are synthesized, in part integrating results of Jobin (2004).

*Core zone of veins (enargite+ pyrite):* Prior to the deposition of enargite, minor amounts of early pyrite-quartz were precipitated. This pyrite is well crystallized and can be compared to pyrite I of the pyrite-quartz bodies, although no pyrrhotite or pyrrhotite inclusions have been observed. Enargite grains form massive aggregates and also are found in vuggy quartz (>90–95% SiO<sub>2</sub>, Fig. 20A) developed in the diatreme breccia. Luzonite typically replaces enargite, but in one sample the opposite was observed. A later pyrite replaces, coats, and is replaced by enargite and luzonite, indicating that

pyrite was deposited throughout the paragenesis. Repeated banding of pyrite and enargite occurs locally.

In the innermost part of the veins, enargite occurs as xenomorphic grains (100–800 μm), which can reach up to 2 mm in size (Fig. 20B). Arsenic contents in enargite range from 15 to 18.3 wt percent, and Sb contents are less than 4 wt percent (Table 5). Antimony contents in luzonite reach 10 wt percent, and As ranges from 11.7 to 17.3 wt percent. Copper and As grades in hand specimens are ~8 and ~2.6 wt percent, respectively (Table 2). Several enargite- and tennantite-bearing samples have high Au concentrations (up to 16 g/t; Table 2).

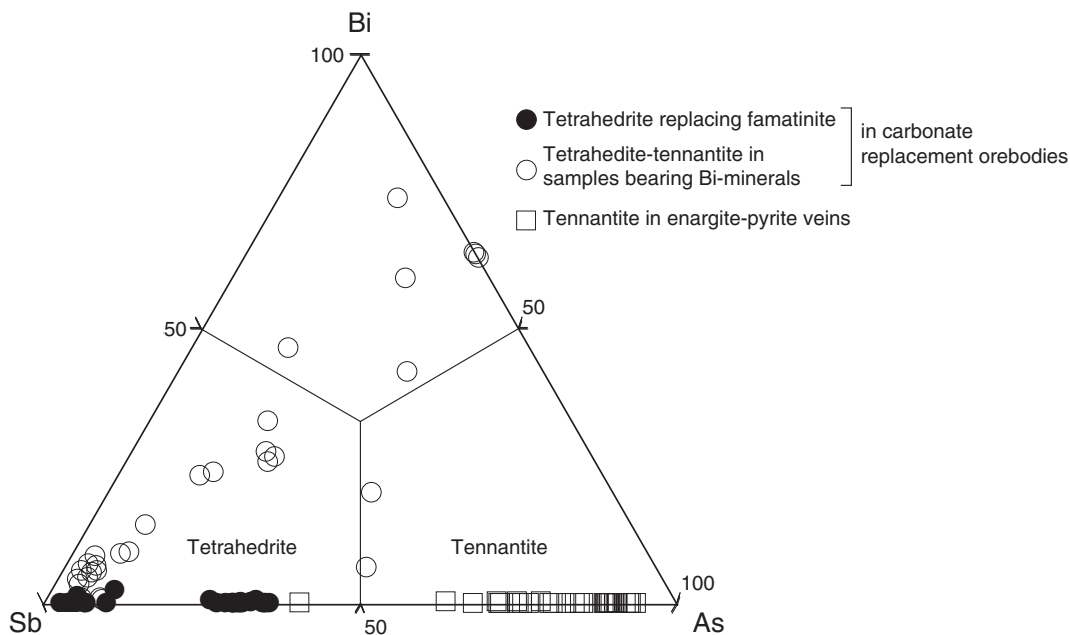


FIG. 15. Tetrahedrite-tennantite composition in second-stage veins and replacement orebodies. There are two tetrahedrite-tennantite populations in replacement orebodies, one Bi poor (solid circles) and another Bi rich (note the positive Bi-As correlation). Bi-rich tetrahedrite-tennantite occurs only in samples carrying Bi minerals, such as bismuthinite-stibnite solid solution, emplectite, or cuprobismuthite. Classification based on Nickel (1992).

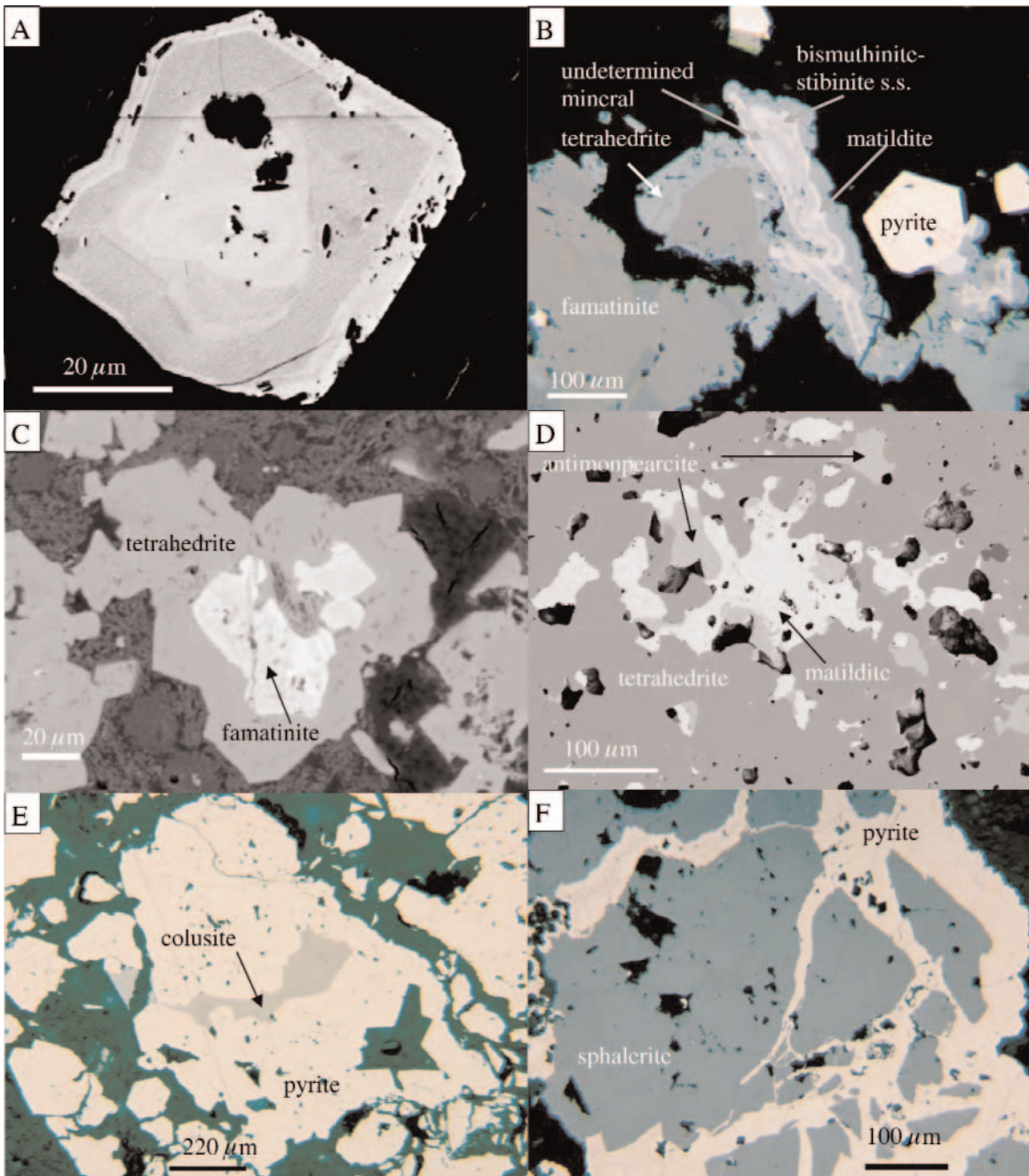


FIG. 16. Photomicrographs from the core and intermediate zones. A. Famatinite crystal showing compositional variations (backscattered electron (BSE) image, CPR 149). B. Overgrowths of tetrahedrite and bismuthinite-stibnite solid solution series on famatinite. A rim of matildite is observed. Note reflection anisotropy of famatinite. The undetermined mineral (gray) is too small to identify, Cuerpo Nuevo, plain-polarized reflected light, CPR 149. C. Famatinite replaced and overgrown by idiomorphic tetrahedrite (BSE, CPR 149). D. BSE image showing blebs of antimonpearcite and matildite within tetrahedrite. Without BSE, antimonpearcite is difficult to distinguish from tetrahedrite; the BSE image reveals the texture of antimonpearcite. Matildite may also be mistaken for galena without BSE (BSE image, CPR 82). E. Local assemblage of pyrite-tetrahedrite-colusite (plain-polarized reflected light, CPR 84). F. Brecciated sphalerite cemented by late pyrite, plain-polarized reflected light, CPR 74.

Alunite occurs in the veins and is, in places, coated by pyrite (Fig. 20C). Alunite has not been observed in contact with enargite. Quartz, zunyite, and alunite form an assemblage (typical of advanced argillic alteration), accompanied by diasporite and APS minerals (e.g., svanbergite and woodhouseite; Table 4) in a 2- to 10-cm-wide halo around the veins.

Barite plates, up to 1 cm, occur in the veins and overgrow enargite and pyrite, for example, in vein 25.

*Intermediate zone of veins (tennantite-pyrite + chalcocopyrite + bornite + chalcocite):* Tennantite, pyrite, chalcocopyrite, bornite, chalcocite, and minor stibnite and bismuthinite, as well as bismuthinite-stibnite solid solution, are present in the

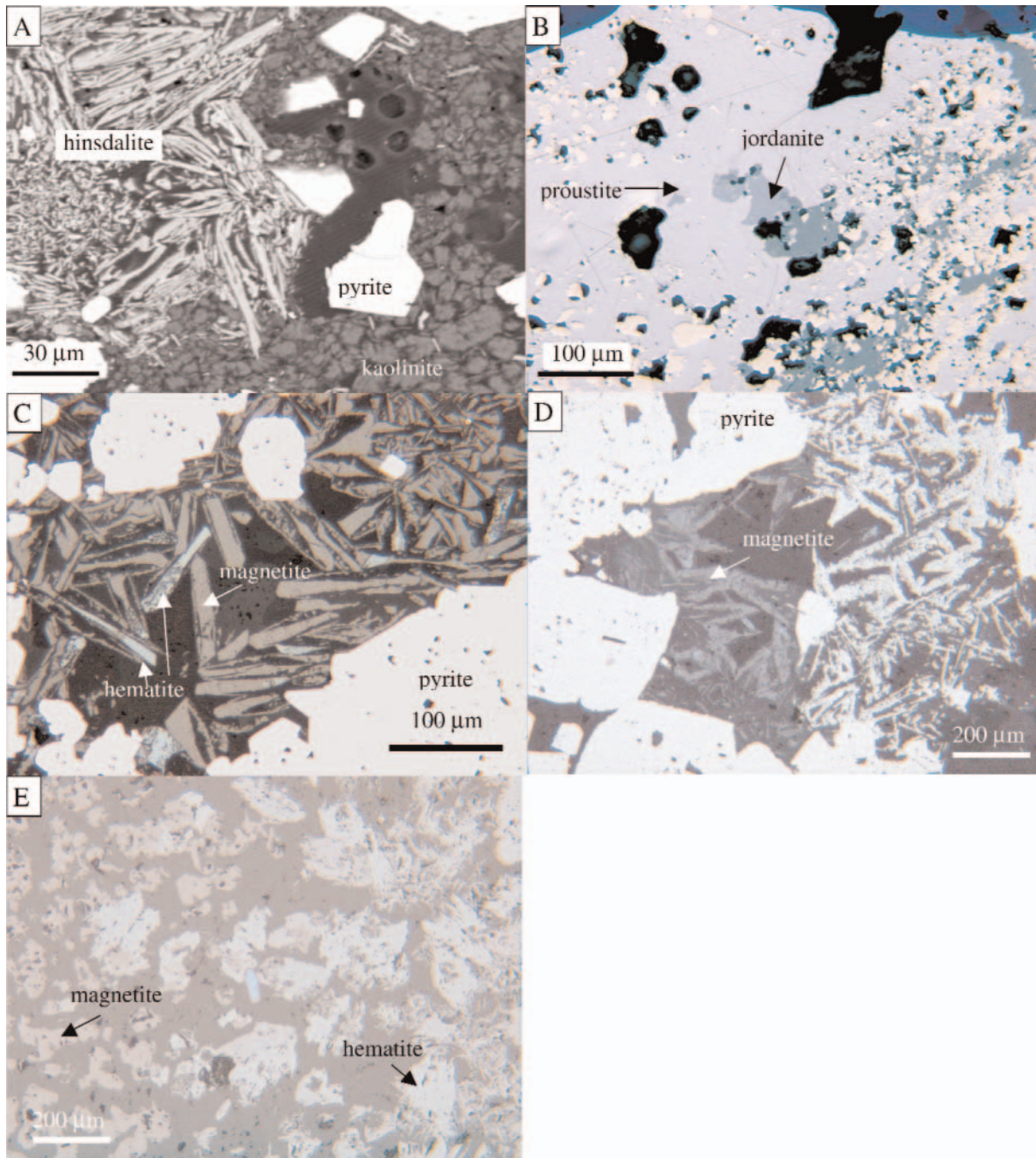


FIG. 17. A. Backscattered electron image showing hinsdalite, kaolinite, and pyrite from the intermediate zone, CPR 81. B. Proustite and jordanite as inclusions in galena, Cayac Noruega, (plain-polarized reflected light, CPR 77. C-E. Photomicrographs of the outermost zone. C. Hematite replaced by magnetite (plain-polarized reflected light, CPR 433). D. Pyrite replacing magnetite, magnetite replacing hematite (plain-polarized reflected light, CPR 433). E. Magnetite replaced by hematite (plain-polarized reflected light, CPR 439).

intermediate zone and are accompanied by APS minerals. Tennantite replaces grain boundaries as well as whole grains of enargite and luzonite. In turn, tennantite grain boundaries are replaced by iron-poor sphalerite (0.2–2.6 mol % FeS). Chalcopyrite occurs as tiny grains (<150 μm) replacing enargite and luzonite and overgrows tennantite. Chalcopyrite also replaces bornite along crystallographic planes (Fig. 20D). Although ubiquitous, chalcopyrite is less abundant than tennantite and

locally fills brecciated pyrite (Fig. 20E). Stibnite, bismuthinite, and bismuthinite-stibnite solid solution generally consist of minute grains (<20 μm) within enargite and luzonite (Jobin, 2004). Arsenic and Sb contents in tennantite range from 13.3 to 18.8 and 1.2 to 8 wt percent Sb, respectively (Table 5).

The APS minerals, svanbergite and hinsdalite, occur in the intermediate zone and are accompanied by kaolinite and, locally, sericite.

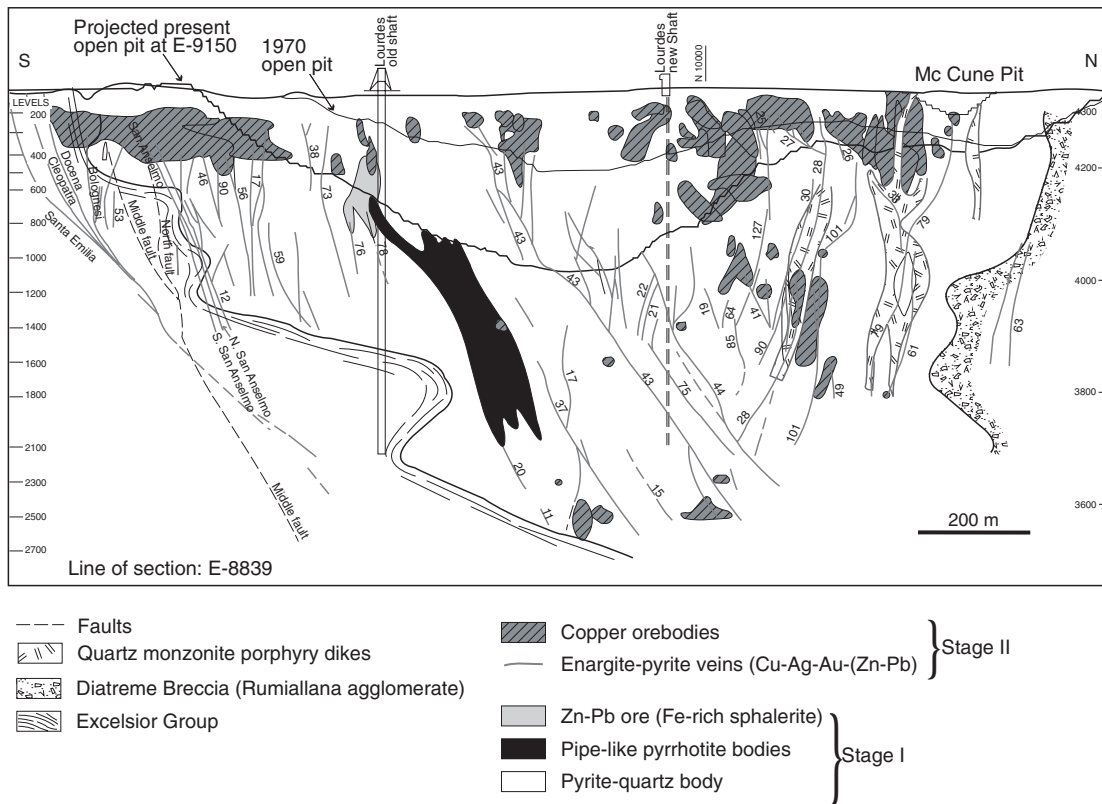


FIG. 18. North-south cross section, showing the limits of the pyrite-quartz body and relative position (projection) of all estimated copper veins and orebodies. Modified from Rivera (1970).

*Outer zones of veins (sphalerite + galena + pyrite):* Sphalerite and galena occur in the outer zone which has a typical width of a few millimeters to centimeters and is weakly developed. They are present as small grains (50–200  $\mu\text{m}$ ), generally replacing tennantite. FeS contents of sphalerite are low (0.2–2.6 mol % FeS). Zinc and Pb were only economic in the upper portions of vein 43 (Ward, 1961).

Small amounts of kaolinite and sericite are the only observed alteration minerals. Sericite in the outer zone is difficult to distinguish from that of the muscovite-pyrite-quartz alteration halo developed in the diatreme breccia at the contact with the pyrite-quartz body.

#### *Enargite-pyrite veins in the southern part of the deposit*

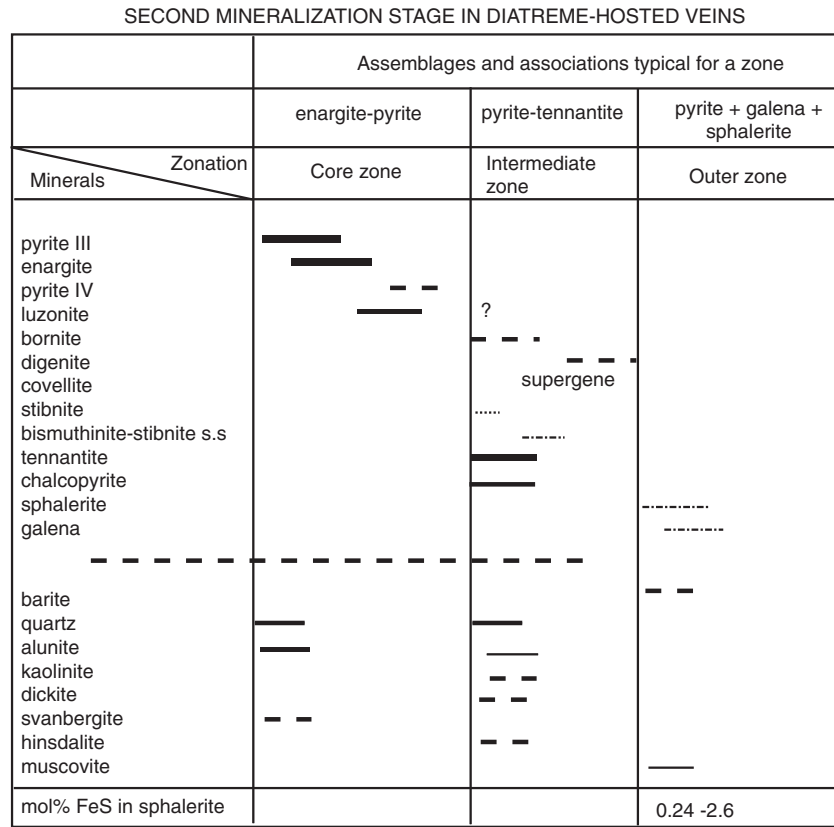
In the southern part of the diatreme, a series of large enargite-pyrite veins, which are presently inaccessible, occupy curved and branched fractures (San Anselmo vein system; Fig. 3). These veins strike from N 60°–70° E through east-west (Ward, 1961). According to previous descriptions (Bowditch, 1935; Ward, 1961), the vein mineral assemblage is similar to the western east-west enargite-pyrite veins hosted by the diatreme breccia and the pyrite-quartz body. However, in the enargite-pyrite veins in the southern part of the open pit, silver minerals such as Ag-rich tetrahedrite are more abundant and chalcopyrite is present. Gold contents are “high” (Ward, 1961), although no values are published. Native gold has been reported by Lacy (1949).

South of the main open pit, in the Santa Rosa pit (Fig. 4), high Au grades (up to 90 ppm; Henry, 2006) occur in strongly

oxidized enargite-pyrite veins in the diatreme breccia and phyllite and shale of the Excelsior Group. These strongly oxidized veins contain goethite and earthy hematite accompanied by alunite, zunyite, diasporite, and quartz. Pervasively advanced argillic-altered porphyritic rocks (probably quartz monzonite dikes) are present in the Santa Rosa open pit. Alunite crystals are commonly mantled with Fe oxides and crystals do not exceed 300  $\mu\text{m}$  in size. Petrographic observations reveal that inclusions of woodhouseite, an APS mineral, are abundant in this zone. The oxidized portions occur along the extension of the southern Excelsior phyllite-hosted enargite-pyrite veins (San Anselmo, Bolognesi, and Cleopatra veins).

#### *Copper orebodies within the pyrite-quartz body*

Graton and Bowditch (1936) and Ward (1961) reported more than 50 copper orebodies in the pyrite-quartz body (Fig. 18), but they were not observed in our study. The copper bodies in the eastern extremity of the pyrite-quartz body were described as pipes, possibly indicating the replacement of limestones (Ward, 1961). The copper bodies are reported to contain enargite and tennantite (i.e., a mineral association similar to that in the east-west-trending enargite-pyrite veins in the diatreme-dome complex) rather than famatinite and tetrahedrite, which is more typical of the carbonate-replacement orebodies. Tennantite is reported to be argentiferous, and hypogene chalcocite replaces chalcopyrite and bornite (Ward, 1961).



**Key** Minerals present in the assemblage

- Always
- - - - Commonly, but not always
- Uncommonly
- ..... Not always and, where present, only in minor amounts
- ..... Rarely

FIG. 19. Paragenetic sequence of the second-stage veins hosted in the diatreme breccia. This sequence reflects the evolution of a fluid in time and space; therefore, minerals precipitating in the outer zones (right part of the diagram) may be contemporaneous with other minerals in the inner zones (left part of the diagram).

*Oxidized veins at Venencocha*

In the Venencocha area, located 2.5 km northwest of the Cerro de Pasco open pit, oxidized veins are observed in the diatreme breccia and mainly controlled by ring structures around the north and northwestern margins of the diatreme (possibly subsidence faults; Fig. 2). They contain massive goethite-jarosite and minor hematite and have an alteration halo consisting of alunite, quartz, zunyite, and diaspore, typical of advanced argillic alteration. Gold anomalies have been detected in the center of the oxidized veins (up to 1 g/t) and decrease toward their borders. Although oxidized, these veins are similar to the enargite-pyrite veins in the western part of the open pit; therefore, they are considered to be part of the second mineralization stage. Advanced argillic-altered dacitic domes with alunite and quartz and with small amounts of zunyite, diaspore, and pyrite are also present. This advanced argillic alteration may be related to the second-stage enargite-pyrite veins or an earlier hydrothermal pulse.

**Supergene Oxidation**

Supergene oxidation locally reaches down to a depth of 100 m below surface. In the eastern part of the deposits, supergene oxidation of carbonate-replacement orebodies produced Ag- and Pb-rich oxidized ores (“pacos”) of economic importance in the past, mainly in the Matagente area. These ores consist of quartz, calcite, limonite, native silver, cerussite, jarosite, calamine, smithsonite, and anglesite (Bowditch, 1935; Amstutz and Ward, 1956).

**Cathodoluminescence and Fluid Inclusion Petrography and Microthermometry**

All fluid inclusions measured are two-phase (liquid + vapor) aqueous inclusions and have sizes between 10 and 45 μm; the microthermometric results are summarized in Table 6 and the results for different fluid inclusion assemblages plotted in Figure 23. Microthermometric measurements were conducted on fluid inclusions belonging to the same fluid inclusion assemblage, as defined by Goldstein and

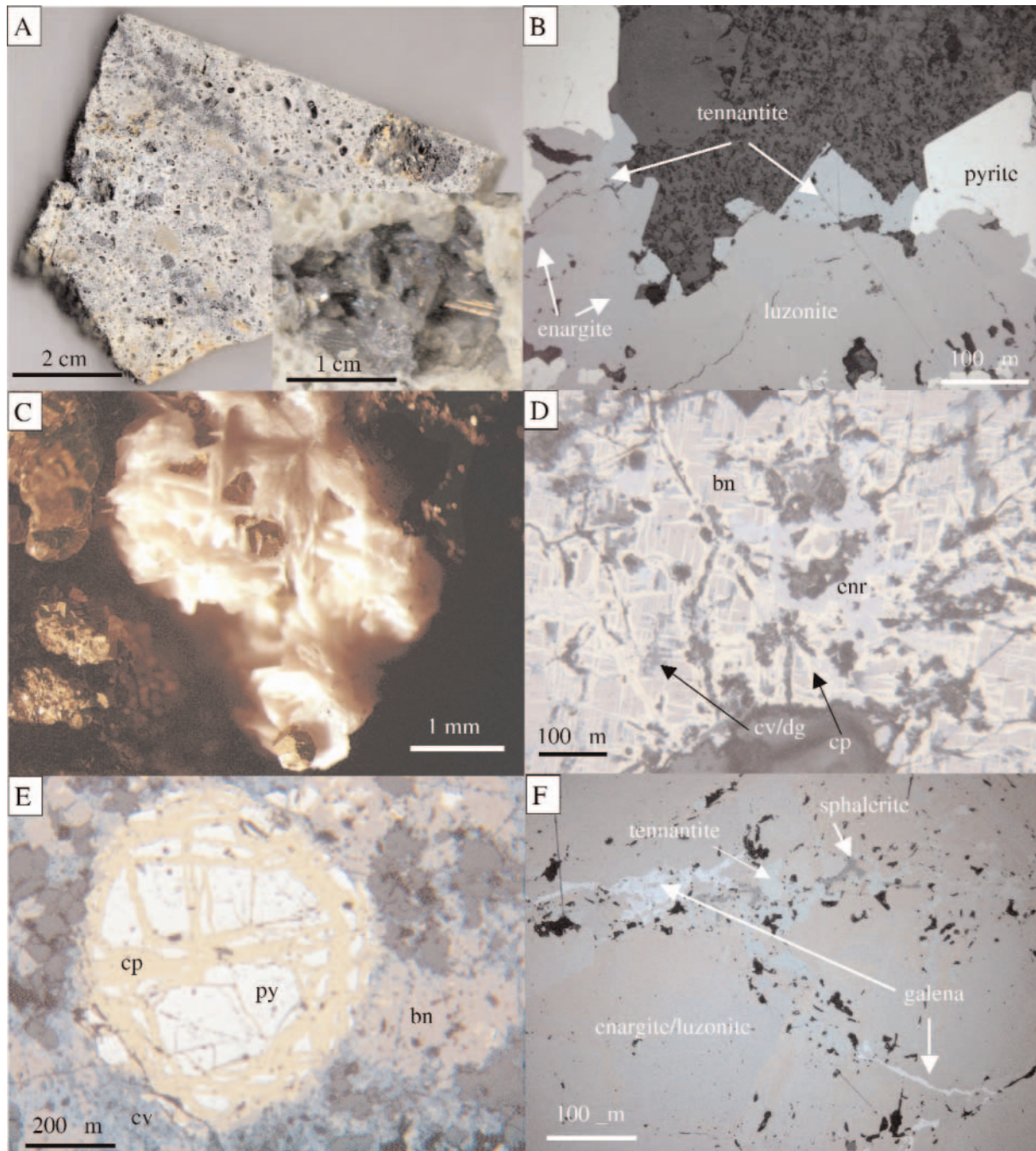


FIG. 20. A. Vuggy quartz in the diatreme breccia with enargite filling the open spaces. B. Enargite-pyrite vein with luzonite replacing enargite and tennantite replacing luzonite (plain-polarized reflected light, CPR 139). C. Alunite in pyrite-quartz body with pyrite coating alunite, indicating a hypogene origin of the latter (CPR 199). D. Chalcopyrite replacing bornite along crystallographic planes (plain-polarized reflected light, CPR 607). E. Brecciated pyrite cemented by chalcopyrite. F. Tennantite, sphalerite, and galena replacing luzonite along grain boundaries in an enargite-pyrite veins (plain-polarized reflected light, Fpe-131-4). Abbreviations: bn = bornite, cp = chalcopyrite, cv = covellite, dg = digenite, enr = enargite, py = pyrite.

Reynolds (1994), and occurring in a single and distinguishable growth zone or defining a single healed microfracture. Raman spectroscopy on selected samples failed to detect  $\text{CO}_2$  or other condensed gases (detection limit of 0.13 mol %: Rosso and Bodnar, 1995). In addition, no clathrate formed during freezing, indicating that  $\text{CO}_2$ , if present, must be in very low concentrations (Rosso and Bodnar, 1995). Because

the hydrothermal system formed close to the present surface, and therefore was likely under hydrostatic conditions, no pressure corrections have been applied.

#### *Pyrite-quartz body (first mineralization stage)*

Cathodoluminescence imaging in quartz grains from the pyrite-quartz body shows only one dull luminescing quartz

TABLE 6. Summary of Fluid Inclusion Types, Morphology, and Characteristics at Cerro de Pasco (data in App. 2, Figs. 9, 10)

Mineralization	Mineral	Stage	Fluid inclusions				Stable isotopes			
			Homogenization temperature min to max (median) (°C)	Salinity min to max (median) (wt % NaCl equiv)	Paleodepth range estimate <sup>3</sup> (m)	δ <sup>34</sup> S (‰)	δ <sup>18</sup> O (‰)	δH (‰)	δ <sup>13</sup> C (‰)	Isotopic fractionation temperature (°C)
Pyrite-quartz body (first stage)	Quartz	I <sub>py-qtz</sub>	200–275 <sup>1</sup> (251)	0.2–6.8 (2.4)	100–600	py: 0.4 (n = 2)	qtz: 13.3–16.5 (n = 3)			qtz : 250
Pyrrhotite bodies (first stage)	Quartz	I <sub>po-qtz</sub>	192–250 (210)	1.1–4.3 (3.4)	100–600	Occurs with pyrrhotite				
Fe-rich sphalerite-bearing Zn-Pb ore (first stage)	Quartz	I <sub>sl-qtz</sub>	183–212 (200)	3.2–4.0 (3.5)	100–600	Occurs with Fe-rich sphalerite	py: 2.8–3.3 (n = 2) sl: 1.9–2.1 (n = 7) py: 0–1.5 (n = 7) sl: -1.6–0.2 (n = 12) gn: 0.8–3.5			
Pre- or syn-second stage?	Quartz	II <sub>qtz</sub>	220–280 (239)	0.7–22.3 (if hydrohalite is present, up to 26.3) (11.9)	n.d.	In cracks within magmatic quartz core; vapor-rich inclusions.				
Second stage enargite veins	Quartz	II <sub>qtz-en</sub>	187–293 (227)	0.2–5.2 (1.1)	200–700	In quartz overgrowths of magmatic quartz	en: 0 (n = 1) py: 2.5 (n = 1) ba: 31.2 (n = 1)	qtz: 10.8–13.3 (n = 3)		qtz: 250
Replacement orebodies (second stage)	Enargite	II <sub>enpy</sub>	195–270 (239)	3.5–9.3 <sup>2</sup> (6.4)	n.d.	Data from Jobin (2004)				
	Quartz	II <sub>qtz-en</sub>	178–265 (234)	0.2–7.5 (4.2)	200–500	In growth zones	sl: -0.7–4.2 (n = 16) gn: -0.7–3.1 (n = 9) ba: 18.1–31.2 (n = 6) and 4.2–10.5 (n = 3)	ba: -1.0–10.4 (n = 8) qtz: 10.1–17.8 (n = 6) kao: 5.3–10.9 (n = 14) cal: 18.8–21.3 (n = 3) Fe-Mn-Zn carb: 9.5–19.5 (n = 14)	kao: -82 to -114 (n = 14)	kao: 250–200 qtz: 250 carb: 200
	Sphalerite	II <sub>sl</sub>	168–222 (196)	3–11.8 (7.1)	n.d.	Isolated inclusions along growth zones				
Veins at Venecocha and Santa Rosa	Quartz	II	245–261 (260)	3.23–7.7 (5.7)	In growth zones	In growth zones	al: 21.5–6.9 (n = 5)	qtz: 14.5–17.5 (n = 2) al: 1.9–6.9 (n = 5)	al: -56–-73 (n = 5)	al: 250

Notes: All inclusions are two-phase, liquid + vapor and have a size between 10 and 45 μm

<sup>1</sup> Two fluid inclusion assemblages with a total of 5 measurements yielding homogenization temperatures between 340° and 375°C and salinities ranging from 0.8 to 5.71 wt percent NaCl equiv have not been considered; they occur in a part of a growth zone (in sample CPR 23a) which could be a relict, alternatively former quartz or these high temperatures are due to necking down because several inclusions in the same zone show necking

<sup>2</sup> Homogenization temperature values are probably underestimated and salinity values over estimated (see text)

<sup>3</sup> Minimum pressures were estimated using the L-V curve calculated with Flincor applying the equation of Brown and Lamb (1989) and converted to depth assuming hydrostatic pressure

generation with locally brightly luminescing growth zones (Fig. 21B). Primary fluid inclusion assemblages in quartz growth zones (Table 6, Figs. 21C, 22A), here termed  $I_{py-qtz}$ ,

have homogenization temperatures and calculated salinities in the range of 200° to 275°C and between 0.2 and 11 wt percent NaCl equiv, respectively (Fig. 23). Within single fluid

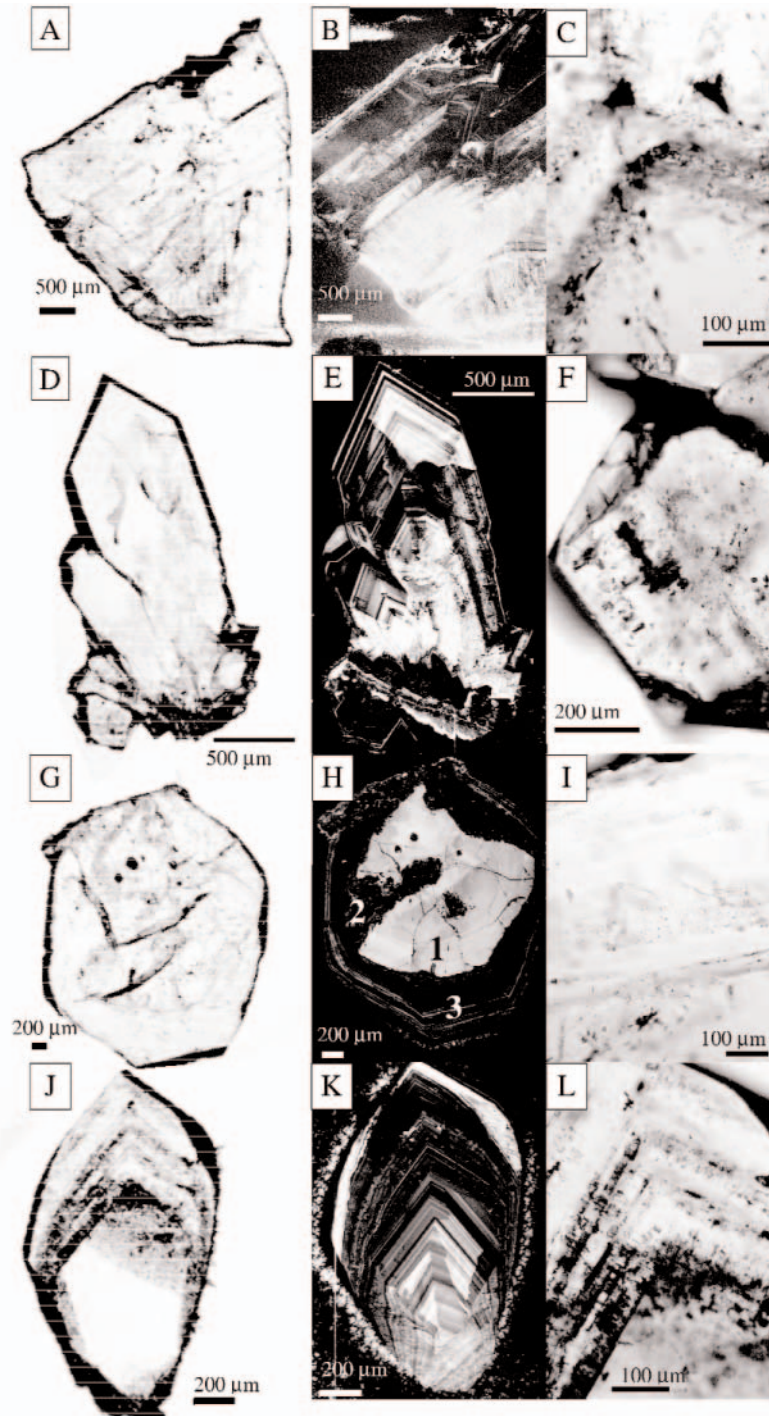


FIG. 21. Transmitted light, cathodoluminescence (CL), and transmitted light images from growth zones in quartz grains used for the microthermometric measurements of fluid inclusions from the pyrite-quartz body (A and B, sample CPR 23c; C, sample 23a, first mineralization stage), from the Venencocha area (D, E, and F, sample CPR 365, second mineralization stage), from quartz grains in the enargite-pyrite veins in the western part of the open pit (G, H, and I, sample CPR 439b, second mineralization stage), and from the carbonate-replacement orebodies in the Matagente area (J, K, and L, sample CPR 480c, second mineralization stage). Note that in (H), CL imaging reveals a magmatic quartz core (1) that shows dissolution borders, overgrown by texturally irregular hydrothermal quartz (2) also showing dissolution textures. This quartz is in part overgrown by oscillating growth zones under CL in hydrothermal quartz (3).

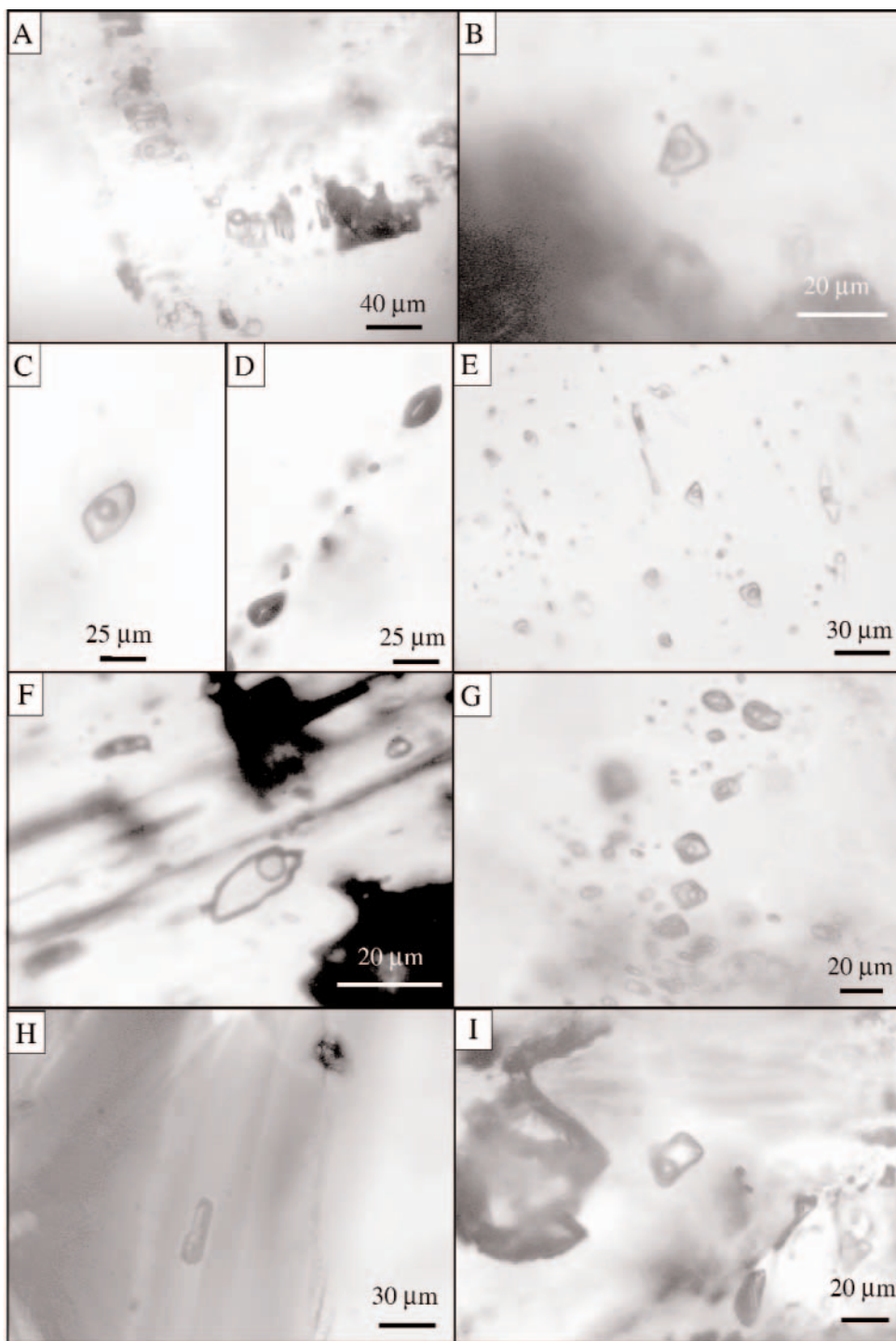


FIG. 22. Selected images of typical fluid inclusion occurrences from the Cerro de Pasco district. A. Fluid inclusions along a growth zone in quartz from the pyrite-quartz body (stage  $I_{py-qtz}$ , sample CPR 23a). B. Isolated fluid inclusion in quartz within pyrrhotite from the first mineralization stage (stage  $I_{po}$ , sample fpe 131-1). C. Saline fluid inclusion along a fracture in the core of magmatic quartz (stage  $IIA1$ , sample CPR 439b). D. Vapor-rich fluid inclusions along healed cracks in the core of magmatic quartz (stage  $IIA1$ , sample CPR 439b). E. Fluid inclusions in a growth zone in quartz from the enargite veins, second mineralization stage (stage  $II_{en-py}$ , sample CPR 439b). F. Infrared image of a fluid inclusion along a growth zone in enargite (stage  $II_{en-py}$ , image from Jobin, 2004). G. Fluid inclusions in growth zone of a quartz crystal from the carbonate-replacement orebodies (stage  $II_{qtz}$ , sample CPR 608a3). H. Fluid inclusions along growth zones in sphalerite from carbonate-replacement orebodies from the second stage (stage  $II_{qtz}$ , sample CPR 480). I. Isolated fluid inclusion in a growth zone in quartz from carbonate-replacement orebodies (stage  $II_{sl}$ , sample CPR 325).

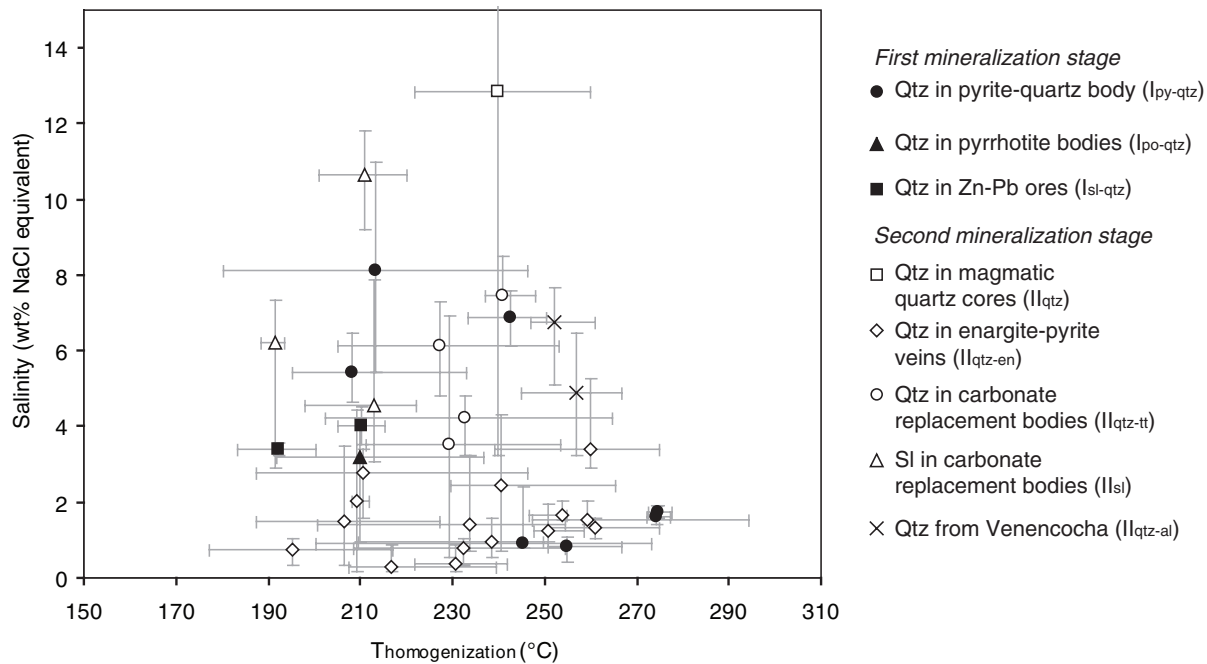


FIG. 23. Homogenization temperature ( $T_h$ ) vs. salinity (wt % NaCl equiv) of fluid inclusion assemblages, mainly in quartz from the first and second mineralization stages and in sphalerite from the carbonate-replacement orebodies (second mineralization stage).

inclusion assemblages, variations in the homogenization temperature are small, whereas salinities are variable (see digital supplement to this paper available at <www.geoscience-world.org>; members and subscribers, <www.segweb.org>). The highest salinities (from 9–11 wt % NaCl equiv) are found in fluid inclusion assemblages that also contain low-salinity inclusions (1.0 wt %; digital supplement). Two explanations can be given for the wide-salinity variation within single assemblages: what is defined as an assemblage is incorrect and fluids were trapped at different times, or the assemblage is real but the inclusions have been opened after trapping and partly reequilibrated with another fluid (e.g., Foley et al., 1989; Simmons, 1991). We therefore consider only fluid inclusion assemblages with limited salinity variations, mostly <7 wt percent NaCl equiv; assemblages that meet this criterion have salinities from 0.2 to 7.5 wt percent NaCl equiv for the pyrite-quartz body. Minimum pressures range from 10 to 55 bars, corresponding to minimum depths of approximately 100 to 600 m below the water table, assuming hydrostatic pressure.

#### *Pipelike pyrrhotite bodies and related Zn-Pb ores (first mineralization stage)*

Quartz grains ( $\leq 500 \mu\text{m}$ ) within pyrrhotite from the pyrrhotite bodies and within sphalerite from related Zn-Pb ores are the only material available for the fluid inclusion study in the pipelike pyrrhotite bodies; a CL study was not conducted on these samples. Fluid inclusion assemblages and isolated inclusions in growth zones in quartz (stage  $I_{\text{po-qtz}}$ ) within pyrrhotite have homogenization temperatures between 192° and 250°C and salinities between 3.7 and 12 wt percent NaCl equiv (Table 6, Fig. 22B). Again, the higher salinities may be the result of reopened inclusions. The salinities of assemblages considered reliable range from 1.1 to 4.3 wt percent

NaCl equiv Stage  $II_{\text{sl-qtz}}$  fluid inclusion assemblages in quartz within Fe-rich sphalerite have homogenization temperatures between 183° to 212°C, with salinities ranging from 3.2 to 7.5 wt percent NaCl equiv. The minimum estimated pressures range between 10 and 60 bars and correspond to minimum depths of 100 to 600 m, which agree with the minimum estimates for the pyrite-quartz body.

#### *Western enargite pyrite veins (second mineralization stage)*

Cathodoluminescence imaging on single quartz grains from the western veins indicates the presence of multiple quartz generations. All analyzed euhedral quartz grains associated with enargite in the core of the veins have a bright luminescing core in CL with complex oscillatory growth zones typical of magmatic quartz and irregular margins indicating dissolution (1, Fig. 21H). These magmatic cores contain melt inclusions ( $\sim 50\text{-}\mu\text{m}$  glass inclusion with a shrinkage bubble) as well as two-phase inclusions (liquid and vapor) and vapor-rich inclusions (stage  $II_{\text{qtz}}$ ) along cracks. The magmatic quartz cores are overgrown by hydrothermal quartz characterized by marked oscillation with predominantly dull to dark luminescence in CL and rare brightly luminescing growth zones (3, Fig. 21H). This hydrothermal quartz contains abundant aqueous inclusions in growth zones (stage  $II_{\text{qtz-en}}$ , Figs. 21I, 22I). Healed fractures are present in the hydrothermal quartz, but fluid inclusions present in those fractures have not been measured because of their small size. In one sample, between the magmatic quartz core and the hydrothermal quartz with growth zones, irregularly luminescing hydrothermal quartz occurs, containing minute inclusions of pyrite and anatase; the texture is characterized by both dark and bright luminescent areas. The external borders of this irregularly luminescing quartz show dissolution borders (Fig. 21H) and contain aqueous inclusions of various shapes and

sizes, commonly with evidence for necking down; therefore, they were not selected for microthermometric measurements.

The two-phase fluid inclusion assemblages coexisting with vapor-rich inclusions along cracks within the magmatic quartz core in diatreme-hosted veins (stage II<sub>qtz</sub>; Table 6, Fig. 22C-D) have homogenization temperatures between 220 and 280°C and highly variable salinities, from 1 up to 22.3 wt percent NaCl equiv (Fig. 23). These cracks do not extend into the hydrothermal quartz, suggesting that the associated inclusions, in part moderately saline (up to 21 wt % NaCl equiv), record a previous hydrothermal pulse. Rare stage II<sub>qtz</sub> fluid inclusions contain hydrohalite that disappears after ice melting, indicating an apparent salinity between 23.2 and 26.3 wt percent NaCl equiv (Goldstein and Reynolds, 1994). Vapor-rich inclusions (>80 vol %) contain no detectable CO<sub>2</sub> and freezing temperatures were not obtained due to unobservable phase changes.

The aqueous stage II<sub>qtz-en</sub> fluid inclusion assemblages in growth zones from hydrothermal quartz have homogenization temperatures from 187° to 293°C and salinities between 0.2 and 5.2 wt percent NaCl equiv. In one sample, fluid inclusions within a growth zone coexist with a small number of vapor-rich inclusions, for which homogenization or freezing measurements were not possible. The minimum pressure estimates from stage II<sub>en-qtz</sub> fluid inclusions range from 20 to 70 bars and correspond to a depth of 200 to 700 m below the water table at hydrostatic pressures.

The fluid inclusions in single enargite grains from enargite-pyrite veins of the second mineralization stage (stage II<sub>en-py</sub>; Table 6, Fig. 22F), measured by Jobin (2004) using an infrared microthermometry stage, have homogenization temperatures between 195° and 270°C with variable salinity (3.5–9.3 wt % NaCl equiv; Jobin, 2004). The above results should be viewed with caution because, according to Moritz (2006), homogenization and melting temperatures obtained by infrared light depend on the light intensity and can result in an overestimation of fluid salinities and underestimation of trapping temperatures. According to the measurements on enargite by Moritz (2006), the trapping temperatures may be underestimated by 15° to 25°C (i.e., 220°–295°C instead of the reported 195°–270°C). Taking into account the temperature uncertainty, the obtained homogenization temperatures are in agreement with the measured temperatures obtained in quartz (220°–290°C) from the quartz-enargite assemblage. The true salinities are difficult to evaluate, because the light intensity may dramatically affect the final ice-melting temperatures (Moritz, 2006).

#### *Carbonate-replacement orebodies (second mineralization stage)*

Several quartz crystals from the center and intermediate zone of carbonate-replacement orebodies show only one generation of hydrothermal quartz based on CL imaging; they are characterized by bright oscillatory luminescence in the center of the crystal that becomes darker toward the borders (Fig. 21K). Some bands contain pyrite inclusions. Fluid inclusions in quartz from the pyrite-tetrahedrite intermediate zone are designated as assemblage II<sub>qtz-tt</sub>, whereas those in sphalerite from the outer zone are termed II<sub>sl</sub>. The abundant stage II<sub>qtz-tt</sub> fluid inclusions contained in this quartz are present in discrete growth zones (Figs. 21L, 22G) and have homogenization temperatures between 178° and 265°C and

salinities from 0.2 to 10.6 wt percent NaCl equiv (Fig. 23). As for the first mineralization stage, the inclusions with a salinity ~10 wt percent coexist in the same assemblage with inclusions having a salinity of ~2 wt percent. For the reasons explained above, the measurements obtained on fluid inclusion assemblages with highly variable salinities are discarded; the remainder salinities vary from 0.2 to 7.5 wt percent NaCl equiv. Pressure estimates vary between 20 and 50 bars, corresponding to a minimum depth of 200 to 500 m below water table at hydrostatic pressure.

Stage II<sub>sl</sub> fluid inclusions in sphalerite from the outer zone of carbonate-replacement orebodies have homogenization temperatures between 168° and 222°C and salinities between 3 and 11.8 wt percent NaCl equiv (Table 6, Fig. 22H). These microthermometric measurements on sphalerite that contains 1 to 2 mol percent FeS could also be affected by the limitations described above for enargite, although the Linkam stage was equipped with an infrared filter.

#### *Venencocha*

One quartz crystal from oxidized veins in the northwestern Venencocha area was studied and shows bright oscillatory luminescence in the center and darker quartz in the external part (Fig. 21E). Stage II<sub>qtz-al</sub> fluid inclusion assemblages have a narrow range of homogenization temperatures between 245° and 265°C and salinities between 3.2 and 7.4 wt percent NaCl equiv (Table 6, Fig. 22B). Minimum hydrostatic pressures have been estimated between 30 and 45 bars, which is equivalent to depths of 300 to 450 m.

### Stable Isotope Results

#### *Pyrite-quartz body (first mineralization stage)*

Oxygen and sulfur isotope compositions of quartz and pyrite from the pyrite-quartz body were analyzed. The δ<sup>18</sup>O values range from 13.3 to 16.5 per mil and δ<sup>34</sup>S values are about 0.4 per mil (Table 6, digital supplement).

Pyrite and sphalerite from the first-stage Zn-Pb mineralization have a narrow range of δ<sup>34</sup>S values from 2.8 to 3.3 and 1.9 to 2.1 per mil, respectively (Table 6). Published δ<sup>34</sup>S data of Austria (1975) reported in Einaudi (1977) for pyrite, sphalerite, and galena from the Zn-Pb ores in underground levels from the mine (digital supplement) range from 0 to 1.5 per mil for pyrite, between -1.6 to -0.2 per mil for galena, and from 0.8 to 3.5 per mil for Fe-rich sphalerite.

#### *Western enargite-pyrite veins (second mineralization stage)*

Quartz from the enargite-pyrite core zone and isolated in vuggy quartz vugs has δ<sup>18</sup>O values between 10.8 and 13.3 per mil (Table 6). Enargite and pyrite from the core zone, both in the pyrite-enargite-quartz assemblage, have δ<sup>34</sup>S values of 0 and 2.5 per mil, respectively. Barite from the intermediate zone of western veins hosted by the diatreme breccia has a δ<sup>34</sup>S value of 31.2 per mil (Fig. 24, Table 6).

#### *Carbonate-replacement orebodies (second mineralization stage)*

Quartz from the core zone of carbonate-replacement orebodies, occurring with pyrite have δ<sup>18</sup>O values from 10.1 to 17.8 per mil (Table 6). Barite samples have δ<sup>18</sup>O values between -1.0 and +10.4 per mil (Table 6).

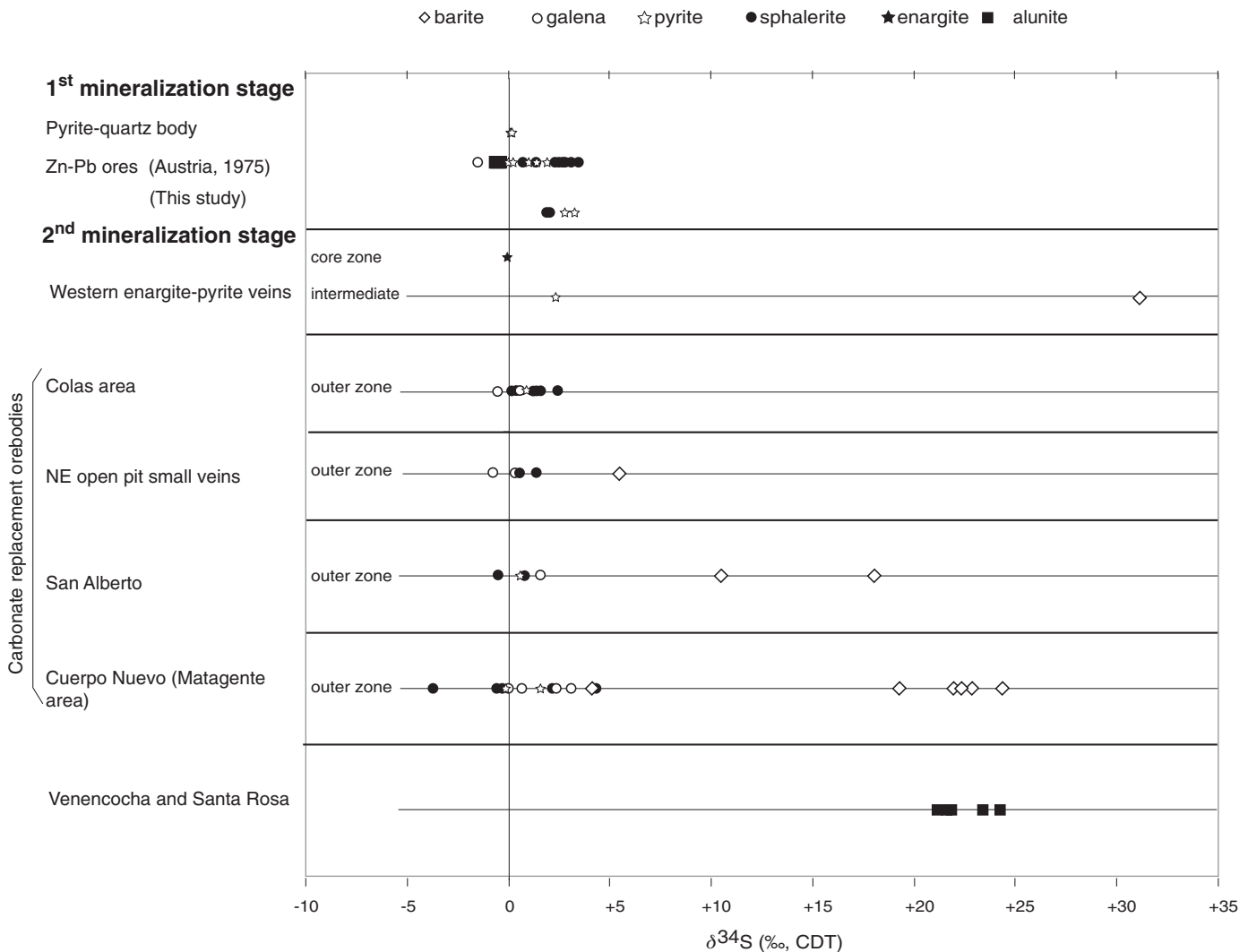


FIG. 24. The  $\delta^{34}\text{S}$  values of sulfides and sulfates from the first and second mineralization stages at Cerro de Pasco.

Hydrogen and oxygen isotope compositions of kaolinite samples from the carbonate-replacement orebodies at Cuerpo Nuevo and the Colas area (Fig. 3) are given in Table 6 and the digital supplement. Kaolinite samples from the intermediate zone occur with hinsdalite, tetrahedrite, and pyrite, whereas in the outer zone, kaolinite is intergrown with sphalerite and galena. The  $\delta^{18}\text{O}$  and  $\delta\text{D}$  values of kaolinite are plotted in Figure 25 and show two populations with respect to the intermediate and outer zones, ranging from  $\delta\text{D} = -85$  to  $-97$  and  $\delta^{18}\text{O} = 5.3$  to  $10.5$  per mil and between  $\delta\text{D} = -114$  to  $-106$  and  $\delta^{18}\text{O} = 9.2$  to  $10.8$  per mil, respectively (Table 6).

Sulfur isotope compositions of pyrite, sphalerite, galena, and barite have been measured in orebodies at Cuerpo Nuevo, Colas, and San Alberto (Table 6). The small veins in the northeastern part of the open pit were also analyzed (Fig. 3). The  $\delta^{34}\text{S}$  values for pyrite from the intermediate and outer zones of the bodies vary from  $-0.1$  to  $+1.6$  per mil. The  $\delta^{34}\text{S}$  values for sphalerite from the outer zone range between  $-3.7$  and  $+4.2$  per mil, and those for galena range from  $-0.7$  to  $+3.1$  per mil. Barite  $\delta^{34}\text{S}$  values fall into two groups. The first group comprises barite with high  $\delta^{34}\text{S}$

values ( $18.1$ – $31.2$ ‰), including samples from Cuerpo Nuevo ( $19.3$ – $24.4$ ‰), one from San Alberto ( $18.1$ ‰), and the only available sample for the western enargite-pyrite veins ( $31.2$ ‰). The second group has lower  $\delta^{34}\text{S}$  values ( $4.2$ – $10.5$ ‰) and includes the single analyzed sample from the uneconomic veins in the northeastern part of the open pit ( $5.5$ ‰), a sample from Cuerpo Nuevo ( $4.2$ ‰), and one from San Alberto ( $10.5$ ‰).

Carbon and oxygen isotopes values were measured in Fe-Mn-Zn-Ca-Mg carbonates from the outermost zone, from late calcite veins close to the orebodies in weakly altered Pucará limestone, and from unaltered Pucará Group rock (Fig. 26). The measured Fe-Mn-Zn-Ca-Mg carbonates include grains overgrowing sphalerite and/or galena and idiomorphic crystals filling voids. The  $\delta^{13}\text{C}$  values for unaltered Pucará Group carbonate rocks range from  $1.4$  to  $2.7$  per mil and the  $\delta^{18}\text{O}$  values from  $19.2$  to  $25.3$  per mil. Late calcite veins have  $\delta^{13}\text{C}$  values ranging from  $0.7$  to  $1.0$  per mil and  $\delta^{18}\text{O}$  values from  $18.8$  to  $21.3$  per mil. Fe-Mn-Zn-Ca-Mg carbonates have a wide range of  $\delta^{13}\text{C}$  values from  $-8.1$  to  $+1.0$  per mil and  $\delta^{18}\text{O}$  values from  $9.5$  to  $19.5$  per mil.

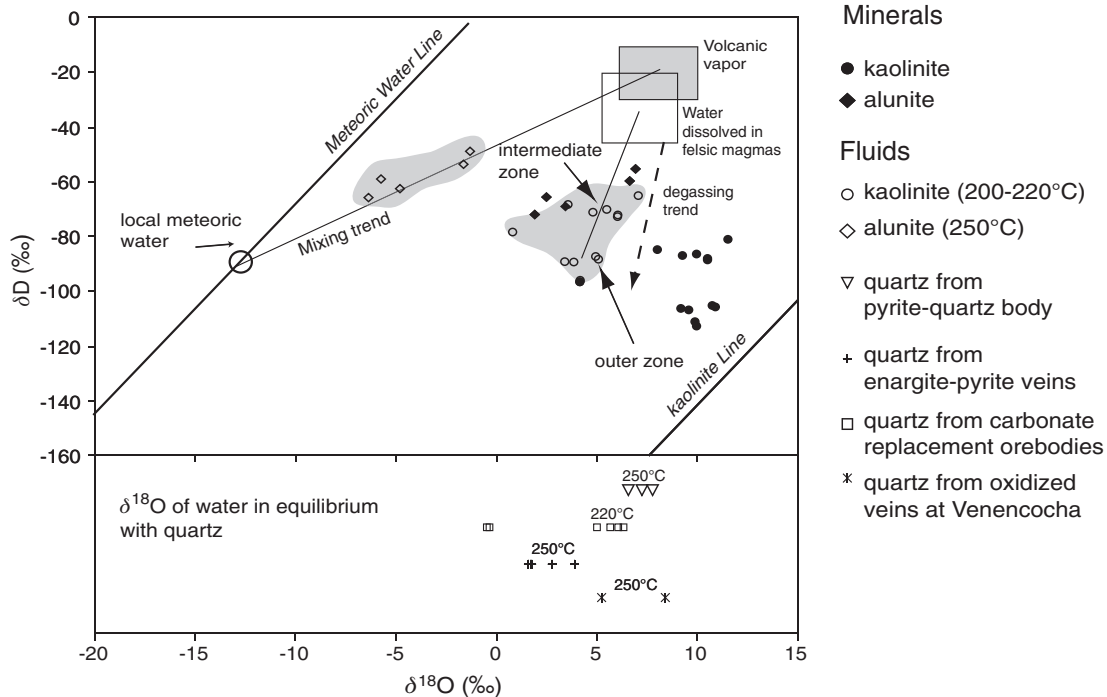


FIG. 25.  $\delta D$  and  $\delta^{18}O$  plot of alunite and kaolinite with corresponding fluids in equilibrium with those minerals. The  $\delta D$  and  $\delta^{18}O$  values of fluid in equilibrium with alunite (from oxidized veins at Venenococha and Santa Rosa) were calculated using the equation of Stoffregen et al. (1994) at 250°C. A mixing trend line shows the two fluid end members responsible for the formation of alunite. This mixing trend intersects the meteoric water line (Craig, 1961) at the  $\delta D$  and  $\delta^{18}O$  values estimated for middle Miocene meteoric water at Cerro de Pasco ( $\delta D = -90 \pm 10\text{‰}$  and  $\delta^{18}O$  close to  $-12 \pm 1\text{‰}$ ). The  $\delta D$  and  $\delta^{18}O$  values of fluids in equilibrium with kaolinite were calculated using fractionation factors of Sheppard and Gilg (1996) for O, and Gilg and Sheppard (1996) for H, at 220°C for kaolinite from the intermediate zone and at 200°C for kaolinite from the outer zone of carbonate replacement orebodies. The kaolinite-equilibrated fluids lie on a mixing trend between meteoric and magmatic water. The magmatic end member corresponds to a fluid characteristic of those of late sericitic alteration fluids. In the lower part of the diagram,  $\delta^{18}O$  values of fluids in equilibrium with quartz are presented, calculated using equation of Zhang et al. (1989) at 250°C in the pyrite-quartz body, 220°C for quartz occurring in the cores of carbonate-replacement orebodies, 250°C for quartz in the enargite-pyrite veins, and 250°C for quartz in oxidized veins at Venenococha. Other fields and lines are the kaolinite line after Sheppard et al. (1969), water dissolved in felsic magmas (Taylor, 1986, 1988) and volcanic vapor after Giggenbach (1992).

### Venenococha and Santa Rosa

Quartz samples from advanced argillic alteration halos around oxidized veins in Venenococha have  $\delta^{18}O$  values of 14.5 and 17.5 per mil. Alunite samples occurring in the association alunite + quartz + zunyite + diaspore from advanced argillic altered halos in oxidized veins at Venenococha also have been analyzed (Table 6). The  $\delta^{34}S_{SO_4}$  values were measured because the sulfate site is more reliable than the hydroxyl site for the retention of primary oxygen isotope compositions in alunite (Bethke et al., 2005). The  $\delta^{18}O_{SO_4}$  values range from 2.5 to 6.9 per mil, the  $\delta D$  values from -56 to -69 per mil, and the  $\delta^{34}S_{SO_4}$  values from 21.1 to 24.2 per mil (Table 6).

In the Santa Rosa area, alunite has a  $\delta^{18}O_{SO_4}$  value of 1.9 per mil, a  $\delta D$  value of -73 per mil, and a  $\delta^{34}S_{SO_4}$  value of 21.5 per mil.

The  $\delta^{18}O_{SO_4}$  and  $\delta D$  values of the alunite samples (CPR 347, Venenococha) and (CPR 351, Santa Rosa) may be disturbed by postdepositional isotope exchange, as suggested by the fact that these samples yield distinctly younger (and unrealistic)  $^{40}Ar/^{39}Ar$  ages (12.3 Ma) than the other analyzed alunite samples (14.5 Ma) and the interpreted 14.5 to 14.4 Ma age of mineralization (Baumgartner, 2007).

### Discussion

A time-space diagram for the magmatic-hydrothermal system at Cerro de Pasco, including the geochronological data of Baumgartner (2007), is shown in Figure 27. The diatremedome complex has been dated at  $15.4 \pm 0.07$  Ma and stage II (enargite-pyrite veins and carbonate replacement orebodies) at  $14.5 \pm 0.08$  to  $14.4 \pm 0.07$  Ma. The age of stage I (pyrite-quartz body and pyrrhotite pipes zoned to Zn-Pb ores) is constrained by crosscutting relationships which indicate that it took place between these two events; the possibility that stages I and II were close in time cannot be excluded.

A first stage with pyrite-dominated mineral assemblages and Fe-rich sphalerite and a second stage with Fe-poor sphalerite also have been recognized in other Cordilleran base metal deposits (Table 1), including the Miocene Peruvian deposits of San Cristobal, Huanzalá, Morococha, and Colquijirca. At San Cristobal, an early stage with pyrite-quartz-wolframite and arsenopyrite and Fe-rich sphalerite is followed by late minor Fe-poor sphalerite, sulfosalts, and galena (Campbell et al., 1984). At Huanzalá (Imai et al., 1985), pyrrhotite appears with pyrite as well as arsenopyrite and Fe-rich sphalerite, which is followed by a late stage with

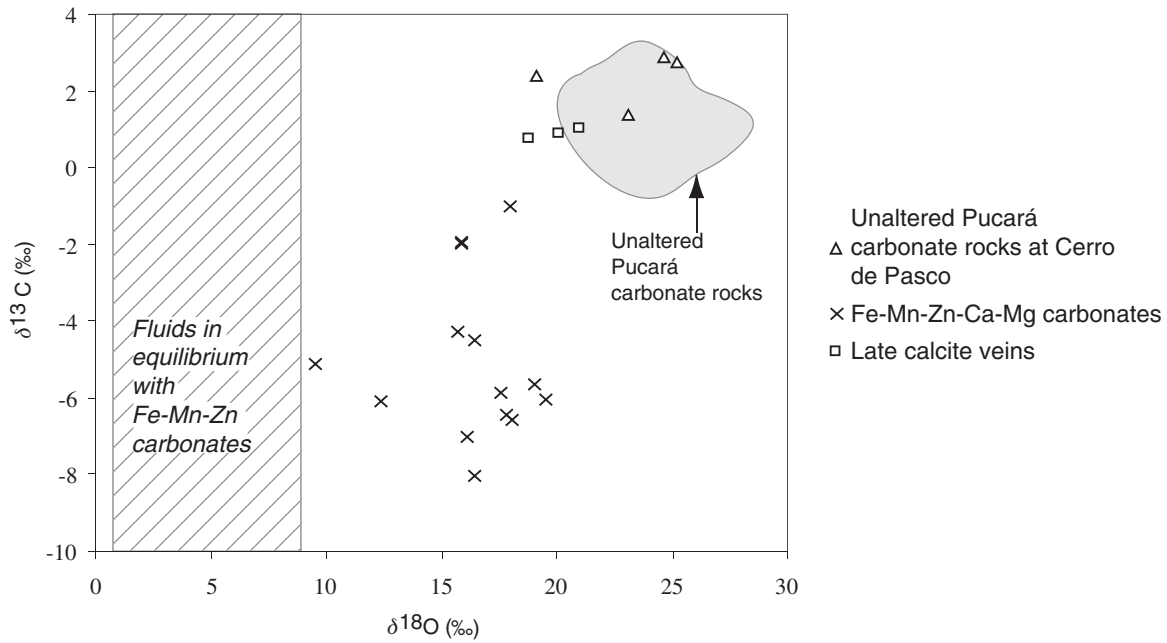


FIG. 26. Plot of  $\delta^{13}\text{C}$  vs.  $\delta^{18}\text{O}$  values of Fe-Mn-Zn-Ca-Mg carbonates and late calcite veins from the carbonate-replacement orebodies (second mineralization stage). Gray field representing  $\delta^{13}\text{C}$  vs.  $\delta^{18}\text{O}$  of unaltered Pucarà carbonate rocks after Moritz et al. (1996). The hatched field represents  $\delta^{18}\text{O}$  values of fluids calculated in equilibrium with Fe-Mn-Zn-Ca-Mg carbonates, using the equation of Zheng (1999) for siderite at 200°C.

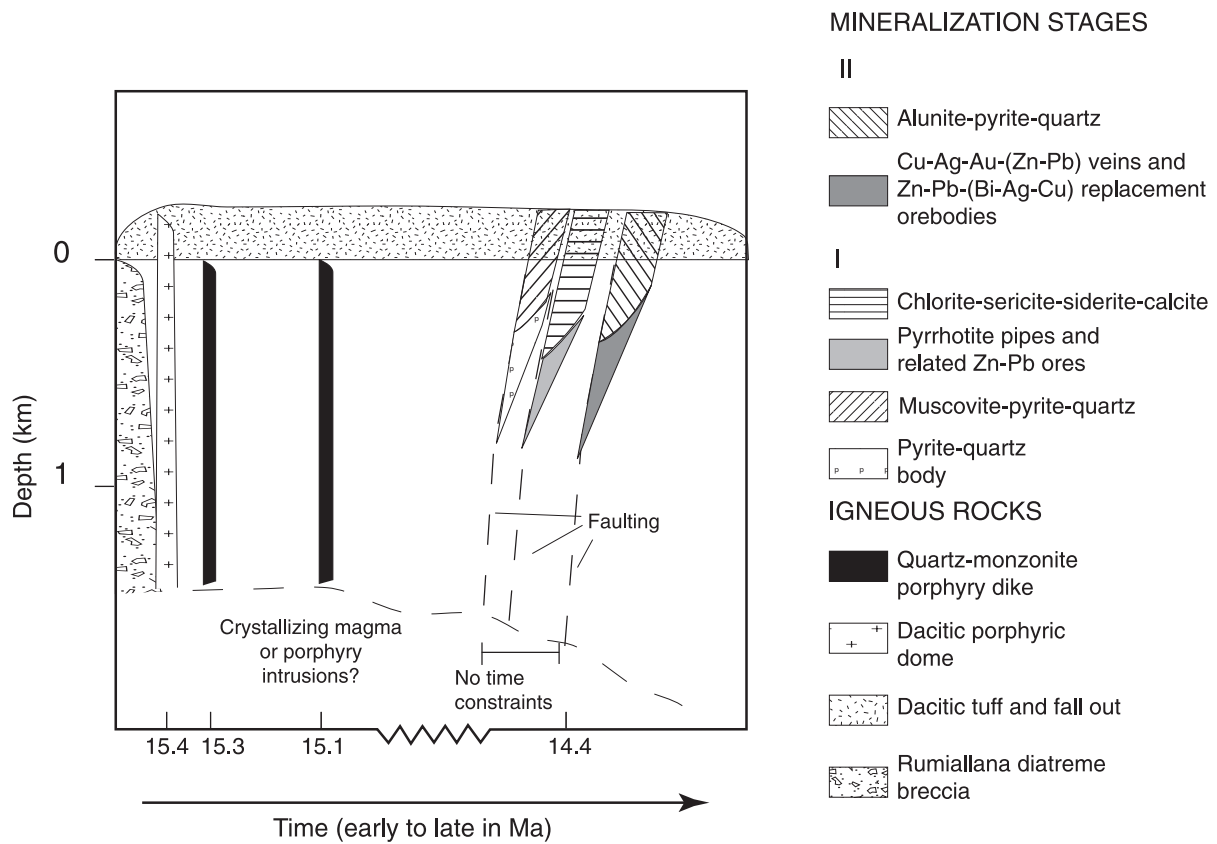


FIG. 27. Time-space diagram for the magmatic-hydrothermal system of Cerro de Pasco. Geochronological data from Baumgartner (2007).

tennantite, enargite, and Fe-poor sphalerite. At Morococha (Petersen, 1965; K. Kouzmanov et al., 2006, unpub. report for Pan American Silver Corp.), the mineralogy of the Italia manto consists of pyrrhotite, magnetite, sphalerite, and galena, and a later stage of mineralization consists of enargite, and/or tennantite, and Fe-poor sphalerite. Most of the Peruvian Cordilleran deposits show an early event with pyrrhotite, arsenopyrite, and Fe-rich sphalerite, although at Colquijirca (Bendezú, 2007), pyrrhotite and Fe-rich sphalerite are not abundant.

#### *Origin of zoning*

The fluid evolution in time and space responsible for the zoning in the second-stage base metal deposits can be explained in terms of advance and retreat of the hydrothermal activity in the sense of Bartos (1989) and Hemley and Hunt (1992). In the core zones of the western enargite-pyrite veins, enargite replaces luzonite, suggesting a slight temperature increase (Maske and Skinner, 1971). This is interpreted to reflect fluid advances, with the inner zones prograding outward and overprinting minerals in the intermediate and/or the outer zones. At Cerro de Pasco, the preexisting minerals are destroyed and relicts are scarce.

At Cuerpo Nuevo, famatinite is replaced and overgrown by tetrahedrite and tetrahedrite by Fe-poor sphalerite, suggesting that the intermediate zone encroached on the core zone and the outer zone encroached on the intermediate zone in a retrograde fashion (i.e., fluid retreat). This late reversal of the overall temporal sequence is interpreted to occur during the cooling of the hydrothermal system (Meyer et al., 1968; Einaudi, 1982; Einaudi et al., 2003).

The spatial and temporal extent of mineral zoning in the veins and replacement orebodies is also a function of the host rock. In the western enargite-pyrite veins, sulfide deposition occurs within an irregular body of leached rocks (residual vuggy quartz), which may have been initially guided by a fault. The residual vuggy quartz was the site of high permeability. In the enargite-pyrite veins, which are hosted by the diatreme breccia and siliciclastic rocks, only the core zone is well developed, whereas the intermediate zone is less developed and the outer zone only almost nonexistent. This may be due to the nonreactive and relatively impermeable nature of the diatreme breccia and siliciclastic host rock. The more porous and reactive carbonate rocks permit percolation and formation of larger replacement orebodies with a well-developed intermediate and outer zone.

#### *Ore-forming fluids and minimum pressures*

Results of the fluid inclusion study in quartz from the first mineralization stage pyrite-quartz body (stage I<sub>py-qtz</sub>) point to the presence of moderate- to low-salinity fluids at temperatures ranging from 200° to 275°C. These temperatures are compatible with the formation of the quartz-muscovite alteration halo adjacent to the pyrite-quartz body. The relatively large range of the fluid inclusion salinities (0.2–6.8 wt % NaCl equiv) can be explained by mixing of a moderately saline fluid (~10 wt %) with a low-salinity fluid. The latter, probably meteoric water, was likely hot because of the lack of correlation between salinity and homogenization temperature (Fig. 23).

The fluid inclusion results obtained in the pipelike pyrrhotite bodies (192°–250°C, 1.1–4.3 wt % NaCl equiv), zoned to Zn-Pb mineralization (183°–212°C, 3.2–4 wt % NaCl equiv), show a slight temperature decrease with decreasing salinity (Fig. 23). This suggests mixing between a hot, moderately saline fluid (10 wt % NaCl equiv) with a slightly cooler and lower salinity fluid, possibly meteoric water, as suggested for the pyrite-quartz body. Overall, there was a decrease in temperature from the pyrite-quartz body and the pyrrhotite pipes outward to the Zn-Pb ores.

From paragenetic observations and fluid inclusions in enargite in the second-stage enargite-pyrite veins in the western part of the open pit, the enargite was precipitated at temperatures from 187° to 293°C and salinities from 0.2 to 5.2 wt percent NaCl equiv (Table 6, Fig. 23). The slightly higher temperatures obtained from fluid inclusions in stage II<sub>qtz-al</sub> quartz from the Venencocha area (245°–261°C, with salinities of 3.2 to 7.7 wt % NaCl equiv) agree with temperature estimates for the formation of diaspore (220°–300°C) and zunyite (250°–300°C) in active geothermal systems (Reyes, 1990).

In the stage II carbonate-replacement orebodies, the temperature decreases from the core zone (178°–265°C, median 234°C, and 0.2–7.5 wt % NaCl equiv in fluid inclusions in quartz) to the outer zone (168°–222°C, median 196°C, and 3–11.8 wt % NaCl equiv in fluid inclusions in sphalerite), but the temperatures are similar to those of the western enargite-pyrite veins (235° and 227°C, respectively). The temperatures correspond to those expected for the dickite and kaolinite stability (upper stability limit of kaolinite at 270°C) in active geothermal systems (Hemley et al., 1980; Reyes, 1990), minerals that are abundant in the intermediate zone of the carbonate-replacement orebodies. According to Hemley et al. (1980) and Reyes (1990), the upper temperature stability limit of dickite is 270°C.

In summary, all fluid inclusions trapped during the second mineralization stage are characterized by salinities of 7.5 to 5.2 wt percent NaCl equiv for the carbonate-replacement orebodies and enargite-pyrite veins, respectively. The variation in salinity most likely resulted from variable mixing of a 10 wt percent NaCl equiv magmatic fluid with a low-salinity fluid (possibly meteoric water). The range of salinities in exsolved water from deep magmas, 2 to 10 wt percent, is in agreement with those obtained for the magmatic end member interpreted for both mineralization stages. The relatively high salinities encountered in fluid inclusions along fractures within the cores of magmatic quartz (up to 26.3 wt % NaCl equiv and 220°–280°C) may have been caused by extreme boiling (cf. Simmons and Browne, 1997) and may not represent a fluid that originally had higher salinities. Alternatively, as reported by Simmons (1991) and Albinson et al. (2001) at Fresnillo, the variations in salinity may have been caused by discrete pulses of saline fluids, boiling at 250° to 330°C. The presence of numerous vapor inclusions favors a boiling scenario which would also be consistent with the observed salinity variations without temperature change. The formation of stage II<sub>qtz</sub> fluid inclusions along the cracks in magmatic quartz might be related to the texturally irregular zone of hydrothermal quartz (2, Fig. 21H) deposited between the magmatic quartz core (1, Fig. 21H) and zoned quartz (3, Fig. 21H). Boiling can take place when the pressure decreases abruptly

and fractures within the magmatic quartz core could be the result of this pressure decrease.

Depths of ore formation for the two mineralization stages using minimum trapping pressures on the L-V curve are estimated to be on the order of 200 to 700 m below water table (Table 6). More precise pressure estimations cannot be made because of the absence of coexisting liquid and vapor inclusions. These depths are consistent with estimates of erosion based on geologic evidence (i.e., on the order of 500 m; see above).

### Stable isotopes

Sulfur isotope compositions measured in sulfides from the first and second stage are compatible with a magmatic source for sulfur ( $-3.7$  to  $+4.2\text{‰}$ ; Table 6; cf. Ohmoto, 1986). Temperature estimates based on sulfur isotope compositions of pyrite-sphalerite, pyrite-galena, and galena-sphalerite pairs from the first-stage pyrrhotite bodies and related Zn-Pb ores range between  $197^\circ$  and  $260^\circ\text{C}$ , using the fractionation equations of Kajiwara and Krouse (1971). These estimates agree with temperatures obtained from fluid inclusions from the first stage ( $192^\circ$ – $250^\circ\text{C}$ ). The mineral pairs pyrite-sphalerite, galena-sphalerite, and barite-pyrite from the second-stage carbonate-replacement orebodies indicate temperatures between  $195^\circ$  and  $271^\circ\text{C}$  (digital supplement), which are in the same range as those obtained by microthermometric measurements ( $178^\circ$ – $265^\circ\text{C}$ ).

Alunite oxygen and hydrogen isotope compositions at Venencocha and Santa Rosa provide an estimate of the composition of meteoric water in the ore-forming fluids. Similar data have been obtained from several epithermal intrusion-centered base metal deposits, including Colquijirca (Bendezú

2007), Julcani (Deen et al., 1994), San Cristobal (Campbell et al., 1984; Beuchat et al. 2004), and Main Tintic (Hildreth and Hannah, 1996; App.), and for epithermal high-sulfidation precious metal deposits such as Summitville (Bethke et al., 2005), Pierina (Fifarek and Rye, 2005), the El-Indio-Pascua belt (Deyell et al., 2005), and Lepanto (Hedenquist et al., 1998), as well as volcanic systems. The presence of magmatic vapor, in addition to meteoric water, has been confirmed at Cerro de Pasco according to the  $\delta^{34}\text{S}_{\text{SO}_4}$  and  $\delta^{18}\text{O}_{\text{SO}_4}$  values of alunite from Venencocha and Santa Rosa. The alunite samples have high  $\delta^{34}\text{S}$  values, characteristic of magmatic-hydrothermal alunite samples as defined by Rye et al. (1992) and also show a large variation in  $\delta^{18}\text{O}$  values (Fig. 28) extending toward  $^{18}\text{O}$ -depleted compositions, which suggests that magmatic vapor with HCl and  $\text{SO}_2$  condensed into meteoric water. The  $\text{SO}_2$  disproportionated to  $\text{HSO}_4^-$  and  $\text{H}_2\text{S}$  (Rye et al., 1992; Arribas et al., 1995), with the  $\text{H}_2\text{S}$  oxidizing to  $\text{SO}_4^{2-}$  in the vadose zone, above the water table (i.e., steam-heated) to form paragenetically late barite at Cerro de Pasco (Fig. 25). The isotopically heavy sulfate in barite (Fig. 25) is thought to be representative of the magmatic sulfur source.

In a  $\delta\text{D}$  versus  $\delta^{18}\text{O}$  diagram (Fig. 25), fields and lines for original water dissolved in felsic magmas prior to exsolution (FMW of Taylor, 1986, 1988) and for meteoric water (Craig, 1961) and kaolinite (Savin and Epstein, 1970) are plotted. The isotopic fractionation of magmatic fluids, which takes place on crystallization (Dobson et al., 1989; Hedenquist and Richards, 1998), is also shown. Values of  $\delta\text{D}$  and  $\delta^{18}\text{O}$  for fluids in equilibrium with alunite (Table 6; digital supplement) were calculated using the fractionation factors from Stoffregen et al. (1994) at  $250^\circ\text{C}$ , which was the temperature estimated from the mineral assemblages and from

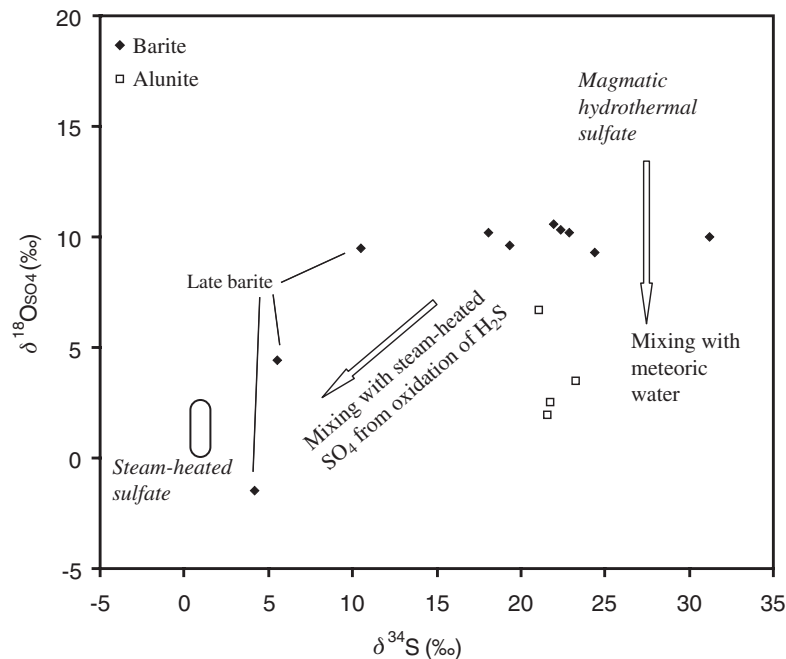


FIG. 28. Summary of  $\delta^{34}\text{S}$  and  $\delta^{18}\text{O}_{(\text{SO}_4)}$  values for alunite (from oxidized veins at Venencocha) and barite (from carbonate-replacement orebodies and enargite-pyrite veins) at Cerro de Pasco, with arrows showing mixing of magmatic-hydrothermal sulfate with meteoric water (recorded by alunite) and with steam-heated sulfate from oxidation of magmatic  $\text{H}_2\text{S}$  (recorded by barite). Steam-heated sulfate field from Rye (2005).

the microthermometric data on quartz occurring with alunite (stage II<sub>qtz-al</sub>). The isotopic composition of meteoric water at Cerro de Pasco can be evaluated by extrapolating the trend obtained for fluids in equilibrium with alunite at Venenococha and Santa Rosa. The two alunite samples which appear to have experienced postdepositional isotopic exchange (Baumgartner, 2007) are not included in the mixing line (Fig. 25). Meteoric water in the middle Miocene had a  $\delta D$  of  $-90 \pm 10$  per mil and a  $\delta^{18}O$  of  $-13 \pm 1$  per mil (Fig. 25), which are higher values than the isotopic composition of local meteoric waters at Julcani during the middle Miocene ( $\delta D = -120$  to  $-138‰$  and  $\delta^{18}O = -17.5$  to  $-18.8‰$ ; Deen et al., 1994) and also higher than those proposed for Colquijirca ( $\delta D = -140 \pm 10‰$  and  $\delta^{18}O = -18 \pm 1‰$ ; Bendezú, 2007). Colquijirca is now located at a similar altitude (4,000–4,300 m) but the deposit is slightly younger (10–12 Ma). The mixing line between meteoric water and the fluids that formed alunite intersects the field of volcanic vapors ( $\delta D = -20‰$  and  $\delta^{18}O = 8‰$ ). In high-sulfidation deposits where a magmatic-hydrothermal genetic model is proposed (Hedenquist et al., 1998; Bethke et al., 2005; Deyell et al., 2005; Fifarek and Rye, 2005; Bendezú, 2007), two end-member fluids are commonly identified, and alunite forms after the magmatic vapor condenses into meteoric water.

Oxygen and hydrogen isotope compositions of fluids in equilibrium with kaolinite were calculated at 220°C for the intermediate zone and at 200°C (based on fluid inclusions) for the outer zone of the carbonate-replacement orebodies, using fractionation factors of Sheppard and Gilg (1996) for  $\delta^{18}O$  and of Gilg and Sheppard (1996) for  $\delta D$ . The intermediate zones of the veins are characterized by higher  $\delta D$  values ( $-71$  to  $-79‰$ ) that lie closer to the magmatic end member than those from the outer zones ( $-83$  to  $-97‰$ ), whereas the  $\delta^{18}O$  values for both zones are similar ( $\delta^{18}O = 2.0$ – $7.3$  and  $4.6$ – $6.3‰$ , respectively). The fluids in equilibrium with kaolinite are interpreted to have formed from mixing of waters of meteoric and magmatic origin (Fig. 25). The results suggest that the magmatic end member is similar to the fluid that produces late phyllic alteration in the porphyry environment (e.g., Beane, 1983; Hedenquist and Richards, 1998). The scatter and low  $\delta D$  values (down to  $-97‰$ ) of the fluids responsible for kaolinite at Cerro de Pasco can be explained by magma degassing, a process which decreases  $\delta D$  in the aqueous liquid, as proposed for other deposits (e.g., Shinohara and Hedenquist, 1997; Hedenquist and Richards, 1998).

Isotopic compositions of water in equilibrium with quartz from the core zones of carbonate-replacement orebodies and enargite-pyrite veins were calculated using equations of Zhang et al. (1989) at 250°C and are plotted in Figure 25. Most measured quartz values in the carbonate-replacement orebodies ( $\delta^{18}O = -1.78$  to  $-0.80‰$ ) and enargite-pyrite veins ( $\delta^{18}O = 1.5$ – $3.8‰$ ) agree with the calculated  $\delta^{18}O$  values estimated for fluids in equilibrium with kaolinite. At the San Alberto carbonate-replacement orebodies, where only the outer zone is present, the  $\delta^{18}O$  value of water in equilibrium with quartz is much lower, perhaps due to a larger proportion of meteoric water in the ore fluid. The  $\delta^{18}O$  values of fluids in equilibrium with quartz from enargite-pyrite veins must be interpreted with caution because they are derived from analyses of quartz grains

which contain magmatic cores, as discussed above. Nevertheless, because the  $\delta^{18}O$  values are similar to those from the replacement orebodies, it is believed that the enargite-pyrite veins were also formed from mixed magmatic-meteoric fluids. For the pyrite-quartz body, the  $\delta^{18}O$  values calculated for fluids in equilibrium with quartz at 250°C (6.6–7.8‰) are slightly heavier than those from the second mineralization stage (Fig. 25) but still compatible with the  $\delta^{18}O$  values of the kaolinite-precipitating fluids. Thus, the latter fluids, which plot close to the magmatic degassing line (Fig. 25), are interpreted to represent slightly diluted fluids (up to ~30%), as shown by the fluid inclusions in quartz from the second-stage carbonate-replacement orebodies. This would also be the case for the first stage based on similar fluid inclusions in quartz. The fluids from the enargite-pyrite veins would have been diluted to at least 50 percent of the magmatic fluid by meteoric water (because fluid inclusions in quartz reach 5.3 wt % NaCl equiv) or they represent an undiluted but more degassed magmatic fluid.

Marine carbonates at Cerro de Pasco (Fig. 26), which are the host rocks of the replacement orebodies, have  $\delta^{13}C$  values (1.3–2.8‰) and  $\delta^{18}O$  values (19.1–24.7‰) similar to those of Pucará limestone reported by Moritz et al. (1996). Hydrothermal Fe-Mn-Zn-Ca-Mg carbonates have  $\delta^{13}C$  values ( $-6.6$  to  $-4.5‰$ ) and  $\delta^{18}O$  values (9.5–19.5‰) that differ from the  $\delta^{13}C$  and  $\delta^{18}O$  values of Pucará limestone. The lower  $\delta^{13}C$  values indicate a stronger contribution of magmatic carbon. Using oxygen isotope fractionation equations for water in equilibrium with siderite, magnesite, and smithsonite (Zheng, 1999), the  $\delta^{18}O$  values of water in equilibrium with Fe-Mn-Zn-Ca-Mg carbonates at 200°C (1.0–8.0‰) are similar to the  $\delta^{18}O$  values of the quartz and kaolinite fluids (2.0–7.3‰). The late vein calcite samples ( $\delta^{13}C = 0.7$ – $0.9‰$  and  $\delta^{18}O = 18.8$ – $21.0‰$ ) lie close to the field of marine limestone, suggesting that the late calcite veins recycled carbonate from the Pucará Group rocks and/or formed at much lower temperatures from fluids that equilibrated with the wall rocks.

Two different mixing trends have been identified based on the microthermometric and stable isotope data: mixing of magmatic and meteoric waters for the second- and first-stage fluids and condensation of magmatic vapor into meteoric water, forming the alunite in oxidized polymetallic veins at Venenococha and at Santa Rosa, with a proportion of magmatic vapor between 70 and 40 percent.

Fluids with characteristics similar to those found at Cerro de Pasco have been described in other intrusion-centered or diatreme-related base metal deposits (App.). Fluid inclusion studies in quartz from these deposits indicate homogenization temperatures between 170° and 350°C and salinities ranging from 0.2 to 8 wt percent NaCl equiv (one generation at Tintic up to 17 wt %), similar to those obtained at Cerro de Pasco. The  $\delta^{18}O$  and  $\delta D$  values are variable from one deposit to another, but for all, both magmatic and meteoric end-member fluids are recognized, and both fluids were involved in mineralization. At Julcani (Deen et al., 1994), San Cristóbal (Campbell et al., 1984; Beuchat et al., 2004), and Colquijirca (Bendezú, 2007), there is evidence for meteoric water as a diluent. At Lepanto, there is strong evidence that meteoric water both condensed and diluted the vapor that leached the

rock and formed alunite (Hedenquist et al., 1998). Mancano and Campbell (1995) showed that the likely cause of enargite deposition at Lepanto was mixing and cooling and/or dilution of the deep magmatic fluid (around 5 wt % NaCl equiv: Hedenquist et al., 1998) with heated ground water.

### Evolution of the Hydrothermal System at Cerro de Pasco

#### First mineralization stage

Mineral reactions and assemblages, temperature of fluids, estimated redox conditions and pH, and FeS content of sphalerite are used to determine the environment of deposition for the first mineralization stage (Table 7). The presence of pyrrhotite is characteristic of low-sulfidation states at 192° to 250°C. Low-sulfidation states are also indicated by the high FeS content of sphalerite in equilibrium with pyrite in Zn-Pb ores from the first stage.

The depositional environment for the first mineralization stage has been plotted on an  $R_H - 1000/T$  diagram [ $R_H = \log(f_{H_2}/f_{H_2O})$  and on a  $\log f_{S_2} - 1,000/T$  (Fig. 29A-B, respectively). The first-stage evolutionary path is represented by a black arrow labeled “ $I_{py-qtz}$ ” for the pyrite-quartz body and “ $I_{po-sl}$ ” for the pyrrhotite pipes and Zn-Pb ores (Fig. 29A-B). Pyrite precipitated at slightly acidic pH (4–5), constrained by the alteration assemblage quartz-muscovite-pyrite in the pyrite-quartz body at 200° to 275°C. The size of the pyrite-quartz body probably reflects a substantial hydrothermal system providing sulfur-rich fluids. The presence of hematite in red chalcidonic clasts within the pyrite-quartz body indicates that conditions were locally oxidizing, possibly due to low rock buffering. However, the presence of pyrrhotite inclusions within pyrite suggests that at higher temperatures (>275°C), the conditions were more reducing. Later, the precipitation of Zn-Pb ores (183°–212°C) was favored at lower  $R_H$  values. The position of the rock buffer, which at Cerro de Pasco included the Excelsior shale and phyllite at depth, is estimated to be lower than the Giggenbach “rock buffer” (an approximation for fresh andesite: Giggenbach, 1987; Fig. 29A). These rocks contain carbonaceous components that would have contributed to more reduced conditions.

#### Second mineralization stage

The mineral reactions and assemblages of the core zones of the enargite-pyrite veins and carbonate-replacement orebodies (Table 7), and in particular the presence of enargite and famatinitite, indicate high-sulfidation states. This is confirmed by the low FeS contents in sphalerite from the carbonate-replacement orebodies which range from 0.02 to 5 mol percent FeS (avg 1 mol % FeS) at 178° to 265°C, as well as in the enargite-pyrite veins, where sphalerite FeS contents are from 0.2 and 2.6 mol percent at 293° to 187°C. Furthermore, the alteration assemblages with development of residual vuggy quartz in the diatreme and deposition of alunite both in the enargite-pyrite veins and carbonate-replacement orebodies indicate very acidic, oxidizing fluids (pH below 2), consistent with a high-sulfidation state (e.g., Einaudi et al., 2003). In the external zones of the carbonate-replacement orebodies, the sulfidation state is intermediate (indicated by the mineral reaction hematite + pyrite => magnetite at 168° to 222°C; Table 7), probably due to interaction of the fluid with the

TABLE 7. Reactions and Assemblages Used for Determining the Sulfidation State of the Two Mineralization Stages at Cerro de Pasco (Fig. 29)

Mineralization	Zones	Reactions	Mineral assemblages	FeS content (% mol) in sphalerite	T (°C) estimate <sup>1</sup>	Sulfidation state <sup>2</sup>
First stage						
Pyrite quartz body with blebs of pyrrhotite ( $I_{py-qtz}$ )		$2FeS + S_2 = 2FeS_2$ pyrrhotite pyrite	Hematite-quartz		250–200	Low
Pyrrhotite pipes ( $I_{po-sl}$ )		$2FeS + S_2 = 2FeS_2$ pyrrhotite pyrite	Sphalerite-pyrite	6–23.9	250–295	Low
Zn-Pb ores (IB)					212–183	Low
Second stage						
Enargite-pyrite veins ( $I_{en-py}$ )	Core	$0.67Cu_3AsS_4 + S_2 = 2.67Cu_2As_2S_{13}$ enargite tetraminitite $Cu_3FeS_4 + 4FeS_2 = 5Cu_4FeS_2 + S_2$ bornite pyrite chalcopyrite	Alunite-quartz		293–187	High
	Intermediate		Sphalerite-pyrite	No data	No data	High-intermediate
Carbonate replacement bodies ( $I_{Zn-Pb}$ )	Core zone	$0.67Cu_3SbS_4 + S_2 = 2.67Cu_2Sb_2S_{13}$ famatinitite tetrahedrite	Alunite-quartz		265–178	High
	Intermediate		Kaolinite-quartz-APS <sup>3</sup>			Intermediate
	Outer		Sphalerite-pyrite	0.1–2.5	222–168	Intermediate
	Outermost	$4Fe_2O_3 + FeS_2 = 3Fe_3O_4 + S_2$ hematite pyrite magnetite	Sphalerite-pyrite	0.4–4.5	No data	Intermediate

<sup>1</sup> Temperature estimates in Baumgartner (2007) from fluid inclusions in quartz, except for those in outer zone of carbonate-replacement bodies which were measured in sphalerite

<sup>2</sup> Einaudi et al. (2003)

<sup>3</sup> APS = aluminum phosphate sulfate minerals, such as himsdalite, svanbergite, and woodhouseite

carbonate host rock, and indicates a decrease in sulfidation states compared to the core zones. This is supported by the fact that the second-stage sphalerite from the outermost zone yields slightly higher FeS contents (up to 4.7 mol %).

The evolution of the second mineralization stage is shown on a log  $f_{S_2}$ -T diagram (Fig. 29B), symbolized by two gray arrows. Arrow  $\Pi_{en-py}$  corresponds to the path for enargite-pyrite veins, whereas the  $\Pi_{Zn-Pb}$  arrow represents the path for the carbonate-replacement orebodies.

The ore mineral zonation suggests that in both carbonate and diatreme host rocks, vein walls were largely sealed due to early quartz and pyrite deposition, which lowered the wall-rock buffering potential during the formation of the core zone, as reported by Bartos (1989) for Yauricocha and Quiruvilca (Peru), Butte, and Main Tintic (United States). Even in the outer zone, characterized by the precipitation of sphalerite and galena at 168° to 265°C (arrow  $\Pi_{Zn-Pb}$ , Fig. 29B), a significant shielding effect by the outermost zones has to be assumed to explain the low pH fluids, indicated by the presence of minerals like hinsdalite and kaolinite. On entering fresh carbonate rocks, a drastic decrease in sulfidation state occurred as a response to pH increase ( $f_{S_2}$  is pH and sulfur content dependent) and resulted in the precipitation of Fe-Mn-Zn-Ca-Mg carbonates. Although the evolutionary paths of the enargite-pyrite veins and carbonate-replacement

ores in  $f_{S_2}$ -T space are similar, the slopes are different, which reflect the contrasting effects of the different host rocks, buffering being a more important control in carbonate rocks.

**Geologic Model**

A geologic model for Cerro de Pasco is proposed in Figure 30 that is consistent with the available geochronological results (Baumgartner, 2007), mineral assemblages, redox conditions, microthermometric, and isotopic results discussed above. Explosive volcanism took place in the middle Miocene and a diatreme-dome complex, >2 km in diameter, was emplaced along the longitudinal fault (Fig. 30A). According to current models for the evolution of porphyry copper systems (e.g., Fournier, 1999; Einaudi et al., 2003), exsolving magmatic fluids accumulated in apophyses, in the brittle-ductile transition zone at around 450°C. Following a pressure decrease near the brittle-ductile transition, phase separation into a coexisting dense brine phase and a low density vapor phase occurred (Ulrich et al., 1999; Harris et al., 2003).

The low-density vapor ascended along fractures (Fig. 30B), and a portion condensed into ground water. The SO<sub>2</sub> disproportionated and, along with the HCl, generated acidic fluids that leached the rocks of the diatreme-dome complex. Only advanced argillic alteration related to the second mineralization stage has been preserved. Hydrothermal fluids derived

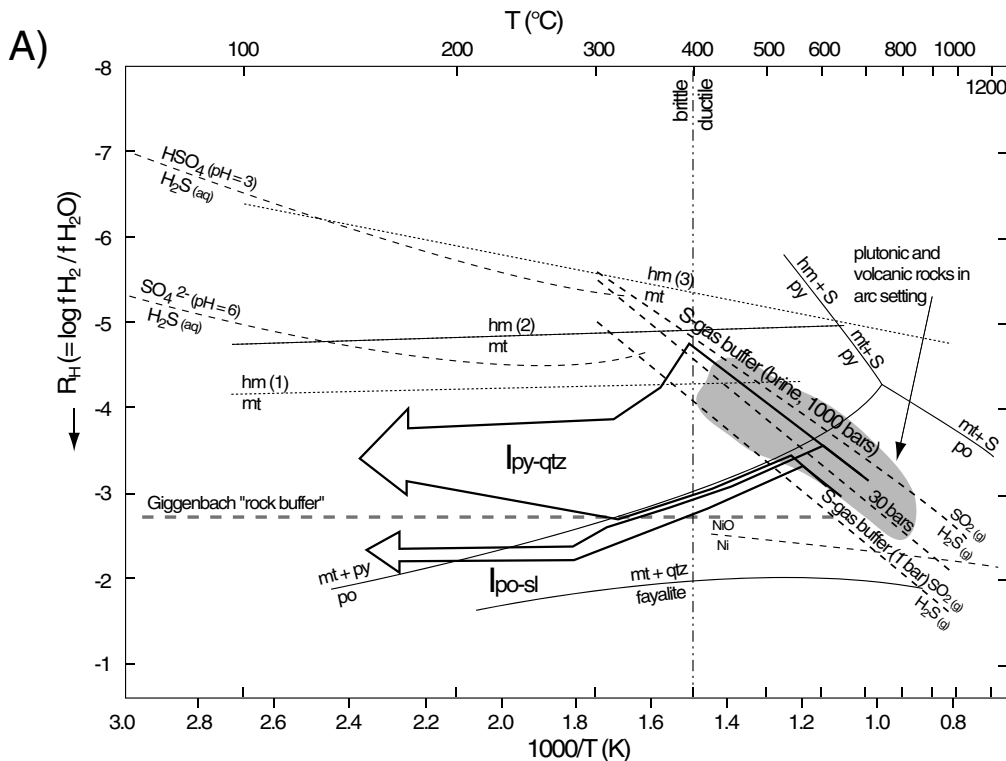


FIG. 29. A.  $R_H$ -1000/T diagram, showing phase boundaries in the system Fe-S-H<sub>2</sub>O and the position of the main redox buffers (after Einaudi et al., 2003).  $R_H = \log (f_{H_2}/f_{H_2O})$ . Mineral abbreviations: hm = hematite, mt = magnetite, po = pyrrhotite, py = pyrite, qtz = quartz. The large unfilled arrow  $I_{py-qtz}$  represents the general path followed by the fluids forming the first mineralization stage pyrite-quartz body. The other arrow ( $I_{po-sl}$ ) represents the pyrrhotite pipes zoned to Zn-Pb ores. The first mineralization stage fluid probably follows the S gas buffer at high temperature and water/rock ratios and at lower temperatures (approx 300°C) precipitates the pyrite-quartz body. At lower water/rock ratios, the fluid reacts with the wall rocks so that the  $R_H$  drops until the “rock buffer” line is reached. At Cerro de Pasco, the rock buffer line was probably lower than the one of Giggenbach (1987), which is based on a fresh andesite, whereas at Cerro de Pasco the rock buffers are shale and phyllite (containing organic matter) from the Excelsior Group.

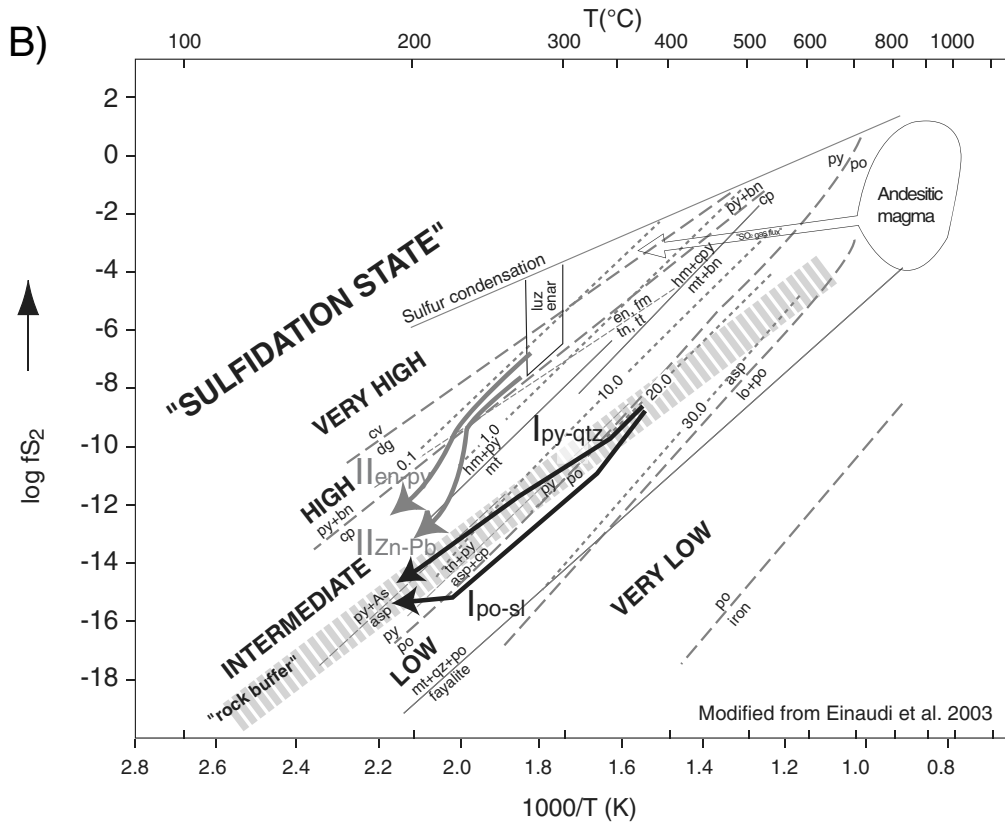


FIG. 29 (Cont.). B.  $\log f_{S_2}$ - $1000/T$  diagram (modified from Einaudi et al., 2003), illustrating fluid environments for the first stage (stage I) and second stage (stage II) for veins hosted by diatreme breccia ( $II_{en-py}$ ) and for replacement orebodies in carbonate rocks ( $II_{Zn-Pb}$ ). Fluid environment is based on sulfide assemblages described in the text, temperatures based on fluid inclusions from Baumgartner (2007), and sulfidation reactions from Barton and Skinner (1979). Mineral abbreviations: asp = arsenopyrite, bn = bornite, cp = chalcopyrite, cv = covellite, dg = digenite, en = enargite, fm = famatinite, hm = hematite, lo = lollingite, mt = magnetite, po = pyrrhotite, py = pyrite, qtz = quartz. Contours of mol percent FeS in sphalerite coexisting with pyrite or pyrrhotite are from Scott and Barnes (1971) and Czamanske (1974). The fluids from the second mineralization stage follow, at high temperatures and water/rock ratios, the  $SO_2$  gas flux. At lower temperatures (around 300°C), the minerals from the core zone precipitate (famatinite and/or enargite with pyrite). Because the vein walls are sealed with an early deposition of pyrite and quartz, the  $\log f_{S_2}$  decreases only slightly. In the diatreme-hosted veins (arrow  $II_{en-py}$ ), this slight decrease continues in the intermediate and outer zones because of partial wall-rock buffering. In contrast, fluids from the replacement orebodies (arrow  $II_{Zn-Pb}$ ) have much lower  $f_{S_2}$  due to wall-rock buffering. The black arrows show the fluid environment of the first mineralization stage  $I_{py-qtz}$  and  $I_{po-sl}$ , which is characteristic of low-sulfidation states. Enargite luzonite inversion between 275° and 300°C is after Maske and Skinner (1971). Brittle-ductile transition from Fournier (1999). The position of the hematite-magnetite phase boundary is after (1) De Haller et al. (2006), (2) Myers and Eugster (1983), and (3) Einaudi et al. (2003).

from the same magmatic source as for the low-density vapor were released and channeled upward along fractures and faults. These fluids mixed with meteoric water and ore deposition took place below 300°C. In the core zones of the second stage, alunite that is related to magmatic vapor condensation into ground water and quartz plus ore minerals related to a magmatic liquid with up to 10 wt percent NaCl coincided and overprinted one another (Fig. 30C).

Most of the carbonate-replacement orebodies show an upward-flaring pipelike morphology with inclined plunge (between 25° and 60°) in the direction of the diatremedome complex, suggesting that the hydrothermal fluids ascended from deeper levels and that no significant lateral feeding from the veins to the carbonate-replacement orebodies took place (Fig. 9). Rather, both veins in the diatreme breccia and carbonate-replacement orebodies may be the result of parallel and divergent ascending fluid paths

within the same hydrothermal system (Fig. 30). The replacement orebodies in carbonate rocks contain Sb-bearing ores, which are virtually As and Au free, with only minor amounts of copper, whereas enargite-pyrite veins contain Cu-As and Au. The enargite-pyrite veins were controlled by east-west faults and the carbonate-replacement orebodies along N 35° E, N 120° E and N 170° E, whereas the pyrite-quartz-body and the pyrrhotite pipes zoned to Zn-Pb ores were channeled mainly along a north-south direction, probably along the longitudinal fault.

The first and the second stages were formed by similar fluids at similar temperatures but the earlier stage that had formed the large W- and Sn-bearing pyrite-quartz body had a lower sulfidation state. A similar early W- and/or Sn-bearing pyrite and/or pyrrhotite-quartz stage has been described in several other Cordilleran deposits (Table 1), and this may be a typical part of the evolution of this class of deposit.

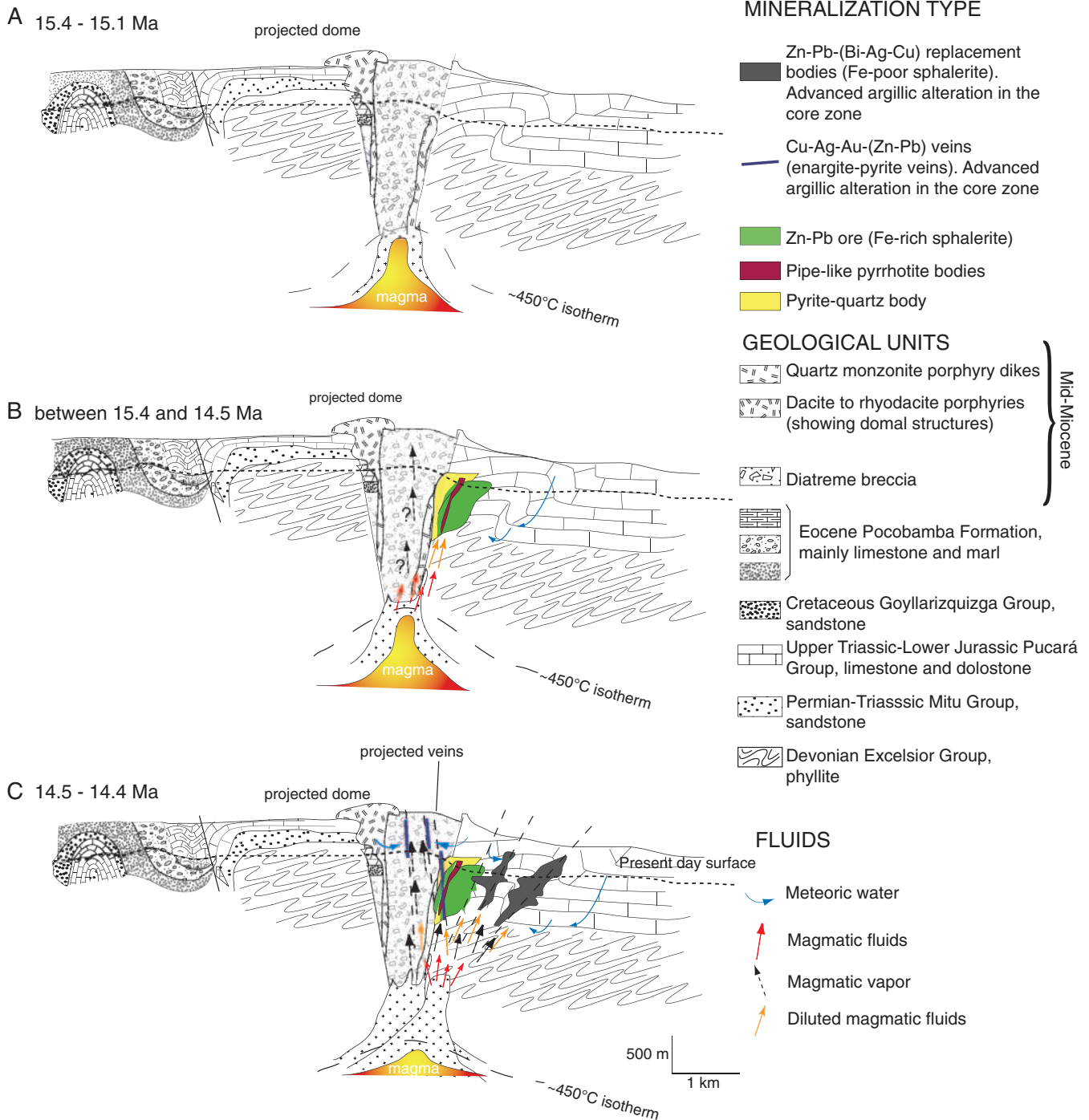


FIG. 30. Time and space evolution of the geologic setting and mineralization setting at Cerro de Pasco. Geology based on Jenks (1951) and Angeles (1999). A. Magmatic activity between 15.4 and 15.1 Ma was characterized by successive intrusions of the diatreme, dacitic domes, and quartz-monzonite dikes (Baumgartner, 2007). B. Hydrothermal activity formed the first mineralization stage (including the pyrite-quartz body and pyrrhotite pipes zoned to Zn-Pb ores). This stage formed from moderate-salinity fluid (orange arrows) formed by mixing between a magmatic water (end-member salinity ~10 wt % NaCl; red arrow) and meteoric water (blue arrows). Magmatic vapors (dashed arrows) were present in the system prior and/or during the first mineralization stage, although erosion has removed the likely associated advanced argillic. C. Formation of the second mineralization stage (between 15.5 and 14.4 Ma, Baumgartner, 2007). The carbonate-replacement orebodies in the eastern part of the open pit were formed by magmatic water (orange arrow) and partially diluted by meteoric water (blue arrow). The alunite of the advanced argillic altered halos of oxidized veins at Venenocha and Santa Rosa (second mineralization stage) formed by a magmatic vapor (dashed arrow) that condensed into meteoric water (blue arrow).

The similarity of the hydrothermal fluids identified at Cerro de Pasco and in the upper parts of other porphyry copper systems (e.g., Butte, Morococha, and Yauricocha), and the superposition of base metal veins on other large porphyry copper deposits raises the question whether Cerro de Pasco conceals a deeper porphyry deposit. The available evidence does not allow this question to be answered.

### Conclusions

In this study, it is confirmed that two stages of mineralization took place at Cerro de Pasco. The first stage was emplaced along north-south structures, following the longitudinal fault and the Cerro anticline, and consists of a pyrite-quartz body and vertical pyrrhotite pipes zoned outward to Zn-Pb-Fe-rich sphalerite-bearing ores. The predominant mineral assemblages are characteristic of low-sulfidation states. However, the presence of hematite within quartz from the pyrite-quartz body suggests that the fluids were locally oxidized, which is typical for exsolving magmatic fluids. The second stage comprises western enargite-pyrite veins hosted in diatreme breccia and in the pyrite-quartz body as well as carbonate-replacement orebodies, which are located on the eastern and central part of the present open pit. The enargite-pyrite veins are controlled by east-west faults, whereas the carbonate-replacement orebodies occur along N 35° E, N°120 E, and N°170 E. There is a marked mineral zonation in the carbonate-replacement orebodies and less well developed in the enargite-pyrite veins. It consists of a core zone (famatinitite and/or enargite-pyrite), an intermediate zone (tetrahedrite and/or tennantite, pyrite, and Bi minerals), an outer zone (Fe-poor sphalerite-galena), and an outermost zone (magnetite-hematite-Fe-Mn-Zn-Ca-Mg carbonates). The outermost zone is absent in the enargite-pyrite veins. The mineral assemblages, with Fe-poor sphalerite, are characteristic of high- to intermediate-sulfidation states. Alteration minerals in the first (quartz-muscovite-pyrite) and second (alunite and other APS minerals, kaolinite) stages are consistent with other evidence of the environment of deposition temperatures of fluids, redox conditions, pH, and FeS content of sphalerite determined from mineral assemblages. High-sulfidation states and very acidic and oxidizing conditions were achieved and maintained in the cores of the second-stage orebodies, even in those replacing carbonate rocks. This suggests that each successive increment of fluid was shielded from the rock buffer due to the effects of the wall-rock alteration itself. The progression with time in single veins and orebodies was from relatively low oxidation and/or sulfidation states to higher oxidation and/or sulfidation states and then returning to lower oxidation and/or sulfidation states.

The fluids forming the first and second mineralization stages at Cerro de Pasco had similar temperatures (200°–250°C and 196°–230°C, respectively) as well as comparable salinities (2.4–3.5 and 4.2–7.1 wt % NaCl equiv). The stable isotope results coupled with the microthermometric data support the existence of a magmatic ore-forming fluid of 10 wt % NaCl equiv diluted by a heated meteoric water (0 wt % NaCl equiv). The advanced argillic alteration bearing alunite of the second stage in the Venenococha and Santa Rosa areas indicates condensation of volcanic vapor into ground water.

Cerro de Pasco was emplaced at a relatively shallow level (200–500 m), corresponding to the upper parts of the porphyry environment; however, porphyry copper mineralization has not been found so far. According to the fluid inclusion study and the stable isotope studies, both mineralization stages are linked and represent successive mineralizing events. This is also indicated by the morphology of Fe-poor sphalerite-bearing carbonate-replacement orebodies of the second mineralization stage, which show an upward-flaring pipelike form with inclined plunge (between 25° and 60°) in the direction of the diatreme-dome complex, suggesting that the hydrothermal fluids ascended from deeper levels and that no lateral feeding from the veins to the carbonate-replacement orebodies took place.

### Acknowledgments

This work was conducted as part of the senior author's Ph.D. dissertation at the University of Geneva. The present investigation was carried out with the support of the Swiss National Science Foundation (FN 200020-108026). We thank Jacob Timmers and Victor Gobitz from the Vólcan Compañía Minera S.A. for providing financial and logistical support. Special thanks to Hugo Alvarez, Romulo Sunny, Enrique Lopez, Luis Fuentes, and Carlos Vera from the Cerro de Pasco Geology staff. We gratefully acknowledge Ronner Bendezú for fruitful discussions as well as Kalin Kouzmanov for the CL images. Jorge Spangenberg is thanked for the sulfur isotope measurements, and Benita Putlitz kindly helped with the analyses of the silicates. We thank M. Einaudi, R. Moritz, and S. Garwin for reviewing an early version of this manuscript. Two *Economic Geology* reviewers, J. Hedenquist and D. John, are thanked for their reviews which helped to clear ideas and M. Hannington for review, comments, and editorial improvements.

April 18, 2007; March 26, 2008

### REFERENCES

- Albinson, T., Norman, D.I., Cole, D., and Chomiak, B., 2001, Controls on formation of low-sulfidation epithermal deposits in Mexico: Constraints from fluid inclusion and stable isotope data: *Society of Economic Geologist Special Publication* 8, p. 1–32.
- Alvarez, A.A., and Noble, D.C., 1988, Sedimentary rock-hosted disseminated precious metal mineralization at Purisima Concepcion, Yauricocha district, central Peru: *ECONOMIC GEOLOGY*, v. 83, p. 1368–1378.
- Amstutz, C., and Ward H., J., 1956, Geología y mineralización del depósito de plomo de Matagente, Cerro de Pasco: *Boletín de la Sociedad Geológica del Perú*, v. 30, p. 13–31.
- Angeles, C., 1999, Los sedimentos Cenozoicos de Cerro de Pasco: Estratigrafía, sedimentación y tectónica, in Machare, J., Benavides-Caceres, V., and Rosas, S., eds., *Sociedad Geológica del Perú*, v. 5, p. 103–118.
- Arribas, A., Cunningham, C.G., Rytuba, J.J., Rye, R.O., Kelly, W.C., Podwysocki, M.H., McKee, E.H., and Tosdal, R.M., 1995, Geology, geochronology, fluid inclusions, and isotope geochemistry of the Rodalquilar gold alunite deposit, Spain: *ECONOMIC GEOLOGY*, v. 90, p. 795–822.
- Austria, B.S., 1975, Geochemical implications of iron in sphalerite: Unpublished Ph.D. thesis, Cambridge, MA, Harvard University, 280 p.
- Barrantes, E.T., 1970, Geología y estructura de la zona del proyecto Morococha [abs.]: Primer congreso latinoamericano de geología, Lima, Resúmenes, p. 97–100.
- Bartlett, M.W., 1984, Petrology and genesis of carbonate-hosted lead-zinc-silver ores, San Cristobal district, Department of Junin, Peru: Unpublished Ph.D. thesis, Oregon State University, 287 p.
- Barton, P.B., and Skinner, B.J., 1979, Sulfide mineral stabilities, in Barnes, H.L., ed., *Geochemistry of hydrothermal ore deposits*, 2nd ed.: New York, NY, Wiley, p. 278–403.

- Barton, P.B.J., Bethke, P.M., and Toulmin, P.I., 1963, Equilibrium in ore deposits: Mineralogical Society of America Special Paper 1, p. 171–185.
- Bartos, P.J., 1987, Quiruvilca, Peru: Mineral zoning and timing of wall-rock alteration relative to Cu-Pb-Zn-Ag vein-fill deposition: *ECONOMIC GEOLOGY*, v. 82, p. 1431–1452.
- 1989, Prograde and retrograde base metal lode deposits and their relationship to underlying porphyry copper deposits: *ECONOMIC GEOLOGY*, v. 84, p. 1671–1683.
- Batchelder, J.N., O'Neil, J.R., Morris, H.T., and Mogensen, A.P., 1978, Geochemistry of fluid inclusions in selected ores from the East Tintic district, Utah: International Association on the Genesis of Ore Deposits Quadrennial Symposium and Field Excursions, 5th, Snowbird, Utah, August, 1978, Proceedings, p. 13–19.
- Baumgartner, R., 2007, Sources and evolution in space and time of hydrothermal fluids at the Cerro de Pasco Cordilleran base metal deposit, Central Peru: *Terre and Environnement*, v. 66, 167 p.
- Baumgartner, R., Fontboté, L., and Bendeziú, R., 2003, Low temperature, late Zn-Pb-(Bi-Ag-Cu) mineralization and related acid alteration replacing carbonate rocks at Cerro de Pasco, Central Peru: Mineral Exploration and Sustainable Development Conference, Athens, 2003, Proceedings, p. 441–444.
- Beane, R.E., 1983, The magmatic-meteorite transition: Geothermal Resources Council Special Report 13, p. 245–253.
- Bendeziú, R., 2007, Shallow polymetallic and precious metal mineralization associated to a Miocene diatreme-dome complex of the Peruvian Andes: The Colquijirca district: *Terre and Environnement*, v. 64, 221 p.
- Bendeziú, R., and Fontboté, L., 2002, Late timing for high-sulfidation Cordilleran base metal lode and replacement deposits in porphyry-related districts: the case of Colquijirca, central Peru: *Society for Geology Applied to Mineral (SGA) News* 13, p. 9–13.
- Bendeziú, R., Fontboté, L., and Cosca, M., 2003, Relative age of Cordilleran base metal lode and replacement deposits, and high-sulfidation Au-(Ag) epithermal mineralization in the Colquijirca mining district, central Peru: *Mineralium Deposita*, v. 38, p. 683–694.
- Bendeziú, R., Page, L., Spikings, R., Pecskey, Z., Fontboté, L., 2007, New  $^{40}\text{Ar}/^{39}\text{Ar}$  alunite ages from the Colquijirca District, Peru. Evidence of long period of magmatic  $\text{SO}_2$  degassing during formation of epithermal Au-Ag and Cordilleran polymetallic ores: *Mineralium Deposita*, in press.
- Bethke, P.M., Rye, R.O., Stoffregen, R.E., and Vikre, P.G., 2005, Evolution of the magmatic-hydrothermal acid-sulfate system at Summitville, Colorado: Integration of geological, stable-isotope, and fluid-inclusion evidence: *Chemical Geology*, v. 215, p. 281–315.
- Beuchat, S., 2003, Geochronological, structural, isotopes, and fluid inclusion constrains of the polymetallic Domo de Yauli district: *Terre and Environnement*, v. 41, 130 p.
- Beuchat, S., Moritz, R., and Pettko, T., 2004, Fluid evolution in the W-Cu-Zn-Pb San Cristobal vein, Peru: Fluid inclusion and stable isotope evidence: *Chemical Geology*, v. 210, p. 201–224.
- Bodnar, R.J., 2003, Reequilibration of fluid inclusions: *Mineralogical Association of Canada Short Course*, v. 32, p. 213–230.
- Bowditch, S.I., 1935, The geology and ore deposits of Cerro de Pasco, Peru: Unpublished Ph.D. thesis, Cambridge, MA, Harvard University, 160 p.
- Brimhall, G.H., 1979, Lithologic determination of mass transfer mechanisms of multiple-stage porphyry copper mineralization at Butte, Montana: Vein formation by hypogene leaching and enrichment of potassium-silicate protore: *ECONOMIC GEOLOGY*, v. 74, p. 556–589.
- Brown, P.E., and Lamb, W.M., 1989, P-V-T properties of fluids in the system  $\text{H}_2\text{O} \pm \text{CO}_2 \pm \text{NaCl}$ : New graphical presentations and implications for fluid inclusion studies: *Geochimica et Cosmochimica Acta*, v. 53, p. 1209–1221.
- Bryant, D.G., 1964, Intrusive breccias and associated ore of the Warren (Bisbee) mining district, Cochise county, Arizona: Unpublished Ph.D. thesis, Stanford, CA, Stanford University, 149 p.
- Campbell, A.R., 1983, Genesis of the tungsten-base metal ores at San Cristobal, Peru: Unpublished Ph.D. thesis, Cambridge, MA, University of Harvard, 176 p.
- Campbell, A.R., Rye, D., and Petersen, U., 1984, A hydrogen and oxygen isotope study of the San Cristobal mine, Peru: Implications of the role of water to rock ratio for the genesis of wolframite deposits: *ECONOMIC GEOLOGY*, v. 79, p. 1818–1832.
- Clark, A.H., Archibald, D.A., Lee, A.W., Farrar, E., and Hodgson, C.J., 1998, Laser probe  $^{40}\text{Ar}/^{39}\text{Ar}$  ages of early- and late-stage alteration assemblages, Rosario porphyry copper-molybdenum deposit, Collahuasi district, I Region, Chile: *ECONOMIC GEOLOGY*, v. 93, p. 326–337.
- Craig, H., 1961, Isotopic variations in meteoric waters: *Science*, v. 133, p. 1702–1703.
- Czamaske, G.K., 1974, The FeS content of sphalerite along the chalcopyrite-pyrite-bornite sulfur fugacity buffer: *ECONOMIC GEOLOGY*, v. 69, p. 1328–1334.
- Deen, J.A., Rye, R.O., Munoz, J.L., and Drexler, J.W., 1994, The magmatic hydrothermal system at Julcani, Peru: Evidence from fluid inclusions and hydrogen and oxygen isotopes: *ECONOMIC GEOLOGY*, v. 89, p. 1924–1938.
- De Haller, A., 2006, The Raúl-Condestable iron oxide copper-gold deposit, central coast of Peru: *Terre and Environnement*, v. 58, 123 p.
- Deyell, C.L., Leonardson, R., Rye, R.O., Thompson, J.F.H., Bissig, T., and Cooke, D.R., 2005, Alunite in the Pasqua-Lama high-sulfidation deposit: Constraints on alteration and ore deposition using stable isotope geochemistry: *ECONOMIC GEOLOGY*, v. 100, p. 131–148.
- Dick, L.A., Chavez, W.X.J., Gonzalez, A., and Bisso, C., 1994, Geologic setting and mineralogy of the Cu-Ag-(As) Rosario vein system, Collahuasi district, Chile: *Society of Economic Geologists Newsletter* 19, p. 6–11.
- Dobson, P.F., Epstein, S., and Stolper, E.M., 1989, Hydrogen isotope fractionation between coexisting vapor and silicate glasses and melts at low pressure: *Geochimica et Cosmochimica Acta*, v. 53, p. 2723–2730.
- Einaudi, M.T., 1968, Pyrrhotite-pyrite-sphalerite relations at Cerro de Pasco, Peru: Unpublished Ph.D. thesis, Cambridge, MA, Harvard University, 381 p.
- 1977, Environment of ore deposition at Cerro de Pasco, Peru: *ECONOMIC GEOLOGY*, v. 72, p. 893–924.
- 1982, Description of skarns associated with porphyry copper plutons, in Titley, S., ed., *Advances in geology of the porphyry copper deposits southwestern North America*: Tucson, AZ, University of Arizona Press, p. 139–183.
- Einaudi, M.T., Hedenquist, J.W., and Inan, E., 2003, Sulfidation state of hydrothermal fluids: The porphyry-epithermal transition and beyond: *Society of Economic Geologists and Geochemical Society Special Publication* 10, p. 285–313.
- Emmons, S.F., 1910, Cananea mining district of Sonora, Mexico: *ECONOMIC GEOLOGY*, v. 5, p. 312–356.
- Field, C.W., Zhang, L., Dilles, J.H., Rye, R.O., and Reed, M.H., 2005, Sulfur and oxygen isotopic record in sulfate and sulfide minerals of early, deep, pre-Main Stage porphyry Cu-Mo and late Main stage base-metal mineral deposits, Butte district, Montana: *Chemical Geology*, v. 215, p. 61–93.
- Fifarek, R.H., and Rye, R.O., 2005, Stable isotope geochemistry of the Pierina high-sulfidation Au-Ag deposit, Peru: Influence of hydrodynamics on  $\text{SO}-\text{H}_2\text{S}$  sulfur isotopic exchange in magmatic-steam and steam-heated environments: *Chemical Geology*, v. 215, p. 253–279.
- Fischer, J., 1977, Silver mines and silver miners in Colonial Peru 1776–1824: Centre for Latin-American Studies, University of Liverpool Monograph 7, 150 p.
- Fontboté, L., and Bendeziú, R., 1999, The carbonate hosted Zn-Pb San Gregorio deposit, Colquijirca district, central Peru, as part of a high sulfidation epithermal system, in Stanley et al., eds., *Mineral deposits: Processes to processing*, v. 1, p. 495–498.
- 2001, The carbonate-hosted San Gregorio and Colquijirca (Zn-Pb-Ag) deposits (central Peru) as products of an epithermal high sulfidation system: *Proexplo 2001*, Lima, Perú, 2001, CD-ROM, 19 p.
- Foley, N.K., Bethke, P.M., Rye, R.O., 1989, A reinterpretation of the delta  $\delta\text{H}_2\text{O}$  of inclusion fluids in contemporaneous quartz and sphalerite, Creede mining district, Colorado: A generic problem for shallow orebodies?: *ECONOMIC GEOLOGY*, v. 84, p. 1966–1977.
- Fournier, R.O., 1999, Hydrothermal processes related to movement of fluid from plastic into brittle rock in the magmatic-epithermal environment: *ECONOMIC GEOLOGY*, v. 94, p. 1193–1211.
- Friehauf, K., 1998, Geology and geochemistry of porphyry-related, carbonate-hosted, massive replacement Cu-Au deposits—a case study of the Superior district, Arizona: Stanford, CA, University of Stanford, 253 p.
- Geological Staff of Cerro de Pasco Corporation, 1950, Lead and zinc deposits of the Cerro de Pasco Corporation in Central Peru: International Geological Congress, 18<sup>th</sup>, Great Britain, 1948, Proceedings, p. 154–186.
- Giesemann, A., Jager, H.-J., Norman, A.L., Krouse, H.R., and Brand, W.A., 1994, On-line sulfur-isotope determination using an elemental analyzer coupled to a mass spectrometer: *Analytical Chemistry*, v. 66, p. 2816–2819.
- Giggenbach, W.F., 1987, Redox processes governing the chemistry of fumarolic gas discharges from White Island, New Zealand: *Applied Geochemistry*, v. 2, p. 143–161.

- 1992, The composition of gases in geothermal and volcanic systems as a function of tectonic setting: *Water-Rock Interaction*, v. 7, p. 873–878.
- Gilbert, J.M., and Park, J.R., 1986, The geology of ore deposits: New York, NY, 750 p.
- Gilg, H.A., 1996, Fluid inclusion and isotope constraints on the genesis of high-temperature carbonate-hosted Pb-Zn-Ag deposits: *Society of Economic Geologists Special Publication*, 4, p. 501–514.
- Gilg, H.A., and Sheppard, S.M.F., 1996, Hydrogen isotope fractionation between kaolinite and water revisited: *Geochimica et Cosmochimica Acta*, v. 60, p. 529–533.
- Goldstein, R.H., and Reynolds, T.J., 1994, Systematics of fluid inclusions in diagenetic minerals: *Society for Sedimentary Geology (SEPM) Short Course Notes* 31, 199 p.
- Graton, L.C., and Bowditch, S.I., 1936, Alkaline and acid solutions in hypogene zoning at Cerro de Pasco, Peru: *ECONOMIC GEOLOGY*, v. 31, p. 651–698.
- Gustafson, L.B., 1961, Paragenesis and hypogene zoning at the Magma mine, Arizona: Unpublished Ph.D. thesis, Cambridge, MA, Harvard University, 88 p.
- Hammer, D.F., and Peterson, D.W., 1968, Geology of the Magma mine area, Arizona, in Ridge, J.D., ed., *Ore deposits of the United States, 1933–1967* (Graton Sales volume): New York, American Institute of Mining and Metallurgical Engineers (AIME), p. 1282–1310.
- Harris, A.C., Kamenetsky, V.S., Van-Achterbergh, E., White, N.C., and Ryan, C.G., 2003, Melt inclusions in veins: Linking magmas and porphyry Cu deposits: *Science*, v. 302, p. 2109–2111.
- Hedenquist, J.W., and Richards, J., 1998, The influence of geochemical techniques on the development of genetic models for porphyry copper deposits: *Reviews in Economic Geology*, v. 10, p. 235–256.
- Hedenquist, J.W., Arribas, A., and Reynolds, T.J., 1998, Evolution of an intrusion-centered hydrothermal system: Far Southeast-Lepanto porphyry and epithermal Cu-Au deposits, Philippines: *ECONOMIC GEOLOGY*, v. 93, p. 373–404.
- Heinrich, C.A., 2005, The physical and chemical evolution of low-salinity magmatic fluids at the porphyry to epithermal transition: A thermodynamic study: *Mineralium Deposita*, v. 39, p. 864–889.
- Hemley, J.J., and Hunt, J.P., 1992, Hydrothermal ore-forming processes in the light of studies in rock-buffered systems: II. Some general geologic applications: *ECONOMIC GEOLOGY*, v. 87, p. 23–43.
- Hemley, J.J., Montoya, J.W., Marinenko, J.W., and Luce, R.W., 1980, Equilibria in the system  $Al_2O_3$ - $SiO_2$ - $H_2O$  and some general implications for alteration-mineralization processes: *ECONOMIC GEOLOGY*, v. 75, p. 210–228.
- Henry, M., 2006, The Marcapunta Oeste prospect, Colquijirca district, and the Santa Rosa prospect, Cerro de Pasco district, Peru: Gold occurrence types: Unpublished M.Sc. thesis, Switzerland, University of Geneva, 132 p.
- Hildreth, S.C., and Hannah, J.L., 1996, Fluid inclusion and sulfur isotope studies of the Tintic mining district, Utah: Implications for targeting fluid sources: *ECONOMIC GEOLOGY*, v. 91, p. 1270–1281.
- Hunt, J.P., 1985, Applied geology at Quebrada Blanca and Collahuasi, Chile, and in the future of United States metal mining: *ECONOMIC GEOLOGY*, v. 80, p. 794–800.
- Imai, H., 1986, Mineralization and paragenesis on the Huanzala mine, central Peru—a reply: *ECONOMIC GEOLOGY*, v. 81, p. 196–199.
- Imai, H., Kawasaki, M., Yamaguchi, M., and Takahashi, M., 1985, Mineralization and paragenesis of the Huanzala mine, central Peru: *ECONOMIC GEOLOGY*, v. 80, p. 461–478.
- Inan, E.E., and Einaudi, M.T., 2002, Nukundamite ( $Cu_{3.38}Fe_{0.62}S_4$ )-bearing copper ore in the Bingham porphyry deposit, Utah: Result of upflow through quartzite: *ECONOMIC GEOLOGY*, v. 97, p. 499–515.
- Jankovic, S., Terzic, M., Aleksic, D., Karamata, S., Spasov, T., Jovanovic, M., Milicic, M., Miskovic, V., Grubic, A., and Antonijevic, I., 1980, Metallogenic features of copper deposits in the volcano-intrusive complexes of the Bor district, Yugoslavia: *Society for Geology Applied to Mineral Deposits Special Publication* 1, p. 42–49.
- Jenks, W.F., 1951, Triassic to Tertiary stratigraphy near Cerro de Pasco, Peru: *The Geological Society of America Bulletin*, v. 62, p. 203–219.
- Jiménez, C., 1924, Síntesis de la minería peruana en el centenario de Ayacucho: *Ministerio de fomento, Minas y Petróleo*, p. 3–71.
- Jobin, Y., 2004, High-sulfidation enargite-pyrite veins at Cerro de Pasco, Peru. A mineralogical study of ore and alteration minerals and an infra-red fluid inclusion study on enargite: Unpublished M.Sc. thesis, Switzerland, University of Geneva, 139 p.
- Kajiwara, Y., and Krouse, H.R., 1971, Sulfur isotope partitioning in metallic sulfide systems: *Canadian Journal of Earth Sciences*, v. 8, p. 1397–1408.
- Kasemann, S., Meixner, A., Rocholl, A., Vennemann, T., Rosner, M., Schmitt, A.K., and Wiedenbeck, M., 2001, Boron and oxygen isotope composition of certified reference materials NIST SRM 610/612 and reference materials JB-2 and JR-2: *Geostandards Newsletter* 12, p. 405–416.
- Kelley, V.C., 1935, Paragenesis of the Colorado copper sulphides, Cananea, Mexico: *ECONOMIC GEOLOGY*, v. 30, p. 663–688.
- Lacy, W.C., 1949, Types of pyrite and their relations to mineralization at Cerro de Pasco, Peru: Unpublished Ph.D. thesis, Cambridge, MA, Harvard University, 193 p.
- Landis, G.P., and Rye, R.O., 1974, Geologic, fluid Inclusion, and stable Isotope studies of the Pasto Buena tungsten-base metal ore deposit, northern Peru: *ECONOMIC GEOLOGY*, v. 69, p. 1025–1059.
- Landtwing, M., 2004, Fluid evolution and ore mineral precipitation at the Bingham porphyry Cu-Au-Mo deposit, Utah, deduced from cathodoluminescence imaging and LA-ICPMS microanalysis of fluid inclusions: Unpublished Ph.D. thesis, Switzerland, ETH Zürich, 260 p.
- Macfarlane, A.W., and Petersen, U., 1990, Pb isotopes of the Hualgayoc area, northern Peru: Implications for metal provenance and genesis of a Cordilleran polymetallic mining district: *ECONOMIC GEOLOGY*, v. 85, p. 1303–1327.
- Macfarlane, A.W., Prol-Ledesma, R., and Conrad, M.E., 1994, Isotope and fluid inclusion studies of the geological and hydrothermal evolution of the Hualgayoc district, northern Peru: *International Geology Review*, v. 36, p. 645–677.
- Mancano, D.P., and Campbell, A.R., 1995, Microthermometry of enargite-hosted fluid inclusions from the Lepanto, Philippines high-sulfidation Cu-Au deposit: *Geochimica et Cosmochimica Acta*, v. 59, p. 3909–3916.
- Maske, S., and Skinner, B.J., 1971, Studies of the sulfosalts of copper: I. Phases and phase relations in the system Cu-As-S: *ECONOMIC GEOLOGY*, v. 66, p. 901–918.
- Masterman, Glenton J., Cooke, David R., Berry, Ron F., Walshe, John L., Lee, Andrew W., and Clark, Alan H., 2005, Fluid chemistry, structural setting, and emplacement history of the Rosario Cu-Mo porphyry and Cu-Ag-Au epithermal veins, Collahuasi district, northern Chile: *ECONOMIC GEOLOGY*, v. 100, p. 835–862.
- McLaughlin, D.H., 1924, Geology and physiography of the Peruvian Cordillera, Department of Junin and Lima: *Geological Society of America Bulletin*, v. 35, p. 591–632.
- Mégard, F., 1978, Etude géologique des Andes du Pérou central-Contribution à l'étude écologique des Andes: Paris, Office de la Recherche Scientifique et Technique Outre-Mer (ORSTOM) Mémoire 86, 310 p.
- Meinert, L.D., 1982, Skarn, manto, and breccia pipe formation in sedimentary rocks of the Cananea mining district, Sonora, Mexico: *ECONOMIC GEOLOGY*, v. 77, p. 919–949.
- Meyer, C., Shea, E.P., Goddard, C., and Staff, 1968, Ore deposits at Butte, Montana, in Ridge, J.D., ed., *Ore deposits of the United States, 1933–1967* (Graton Sales volume): New York, American Institute of Mining and Metallurgical Engineers (AIME), p. 1372–1416.
- Moritz, R., 2006, Fluid salinities obtained by infrared microthermometry of opaque minerals: Implications for ore deposit modeling—a note of caution: *Journal of Geochemical Exploration*, v. 89, p. 284–287.
- Moritz, R., Fontboté, L., Spangenberg, J., Rosas, S., Z., S., and Fontignie, D., 1996, Sr, C and O isotope systematics in the Pucará basin, central Peru: Comparison between Mississippi Valley-type deposits and barren areas: *Mineralium Deposita*, v. 31, p. 147–162.
- Morris, H.T., 1968, The Main Tintic mining district, Utah, in Ridge, J.D., ed., *Ore deposits of the United States, 1933–1967* (Graton Sales volume): New York, American Institute of Mining and Metallurgical Engineers (AIME), p. 1043–1073.
- Myers, J., and Eugster, H.P., 1983, The system Fe-Si-O: Oxygen buffer calibrations to 1,500K: *Contributions to Mineralogy and Petrology*, v. 82, p. 75–90.
- Nickel, E.H., 1992, Solid solutions in mineral nomenclature: *Canadian Mineralogist*, v. 30, p. 231–234.
- Ohmoto, H., 1986, Stable isotope geochemistry of ore deposits: *Reviews in Mineralogy*, v. 16, p. 491–559.
- Ossandón, C., Freraut, C.R., Gustafson, L.B., Lindsay, D.D., and Zentilli, M., 2001, Geology of the Chuquicamata mine: A progress report: *ECONOMIC GEOLOGY*, v. 96, p. 249–270.
- Padilla Garza, R.A., Tittley, S.R., and Pimentel B., F., 2001, Geology of the Escondida porphyry copper deposit, Antofagasta region, Chile: *ECONOMIC GEOLOGY*, v. 96, p. 307–324.

- Paul, A.H., and Knight, M.J., 1995, Replacement ores in the Magma mine, Superior, Arizona: Arizona Geological Society Digest, v. 20, p. 366–372.
- Perry, V.D., 1961, The significance of mineralized breccia pipes: Mining Engineering, v. 13, p. 367–376.
- Petersen, U., 1965, Regional geology and major ore deposits of central Peru: ECONOMIC GEOLOGY, v. 60, p. 407–476.
- Profett, J.M.J., 1979, Ore deposits of the western United States: A summary: Nevada Bureau of Mines and Geology, p. 13–32.
- Ransome, F.L., 1912, Copper deposits near Superior, Arizona: U.S. Geological Survey Bulletin, v. 540, p. 129–158.
- Reyes, A.G., 1990, Petrology of Philippine geothermal systems and the application of alteration mineralogy to their assessment: Journal of Volcanology and Geothermal Research, v. 43, p. 279–309.
- Rivera, N., 1970, Mina Cerro de Pasco, Geología de los yacimientos minerales operados por la Cerro de Pasco Corporation, La Oroya, Peru: Departamento de Geología de la Cerro de Pasco Corporation Internal Report, p. 12–40.
- 1997, The Pasco belt and the metallogenesis of the Cerro de Pasco mineral district: IX Congreso Geológico del Perú, 1997, Proceedings, p. 167–173.
- Rogers, R., 1983, Structural and geochemical evolution of a mineralized volcanic vent at Cerro de Pasco, Peru: Unpublished PhD thesis, Tucson, University of Arizona, 116 p.
- Rosas, S., Fontboté, L., and Tankard, A., 2007, Tectonic evolution and paleogeography of the Mesozoic Pucará basin, central Peru: Journal of South American Earth Sciences, v. 24, p. 1–24.
- Rosso, K.M. and Bodnar, R.J., 1995, Microthermometric and Raman spectroscopic detection limits of CO<sub>2</sub> in fluid inclusions and the Raman spectroscopic characterization of CO<sub>2</sub>: Geochimica et Cosmochimica Acta, v. 59, p. 3961–3975.
- Rubright, R.D., and Hart, O.J., 1968, Non-porphyry ores of the Bingham District, Utah, in Ridge, J.D., ed., Ore deposits of the United States 1933–1967 (Graton Sales volume): New York, American Institute of Mining and Metallurgical Engineers (AIME), p. 886–908.
- Rumble, D., and Hoering, T.C., 1994, Analysis of oxygen and sulfur isotope ratios in oxide and sulfide minerals by spot heating with a carbon dioxide laser in a fluorine atmosphere: Accounts of Chemical Research, v. 27, p. 237–241.
- Rye, R.O., 2005, A review of the stable-isotope geochemistry of sulfate minerals in selected igneous environments and related hydrothermal systems: Chemical Geology, v. 215, p. 5–36.
- Rye, R.O., Bethke, P.M., and Wasserman, M.D., 1992, The stable isotope geochemistry of acid-sulfate alteration: ECONOMIC GEOLOGY, v. 87, p. 225–262.
- Sales, R.H., and Meyer, C., 1949, Results from preliminary studies of vein formation at Butte, Montana: ECONOMIC GEOLOGY, v. 44, p. 465–484.
- Savin, S.M., and Epstein, S., 1970, The oxygen and hydrogen isotope geochemistry of clay minerals: Geochimica et Cosmochimica Acta, v. 34, p. 25–42.
- Sawkins, F.J., 1972, Sulfide ore deposits in relation to plate tectonics: Journal of Geology, v. 80, p. 377–397.
- Schwartz, G.M., and Park, C.F., 1932, A microscopic study of ores from the Campbell mine, Bisbee, Arizona: ECONOMIC GEOLOGY, v. 27, p. 39–51.
- Scott, S.D., and Barnes, H.L., 1971, Sphalerite geothermometry and geobarometry: ECONOMIC GEOLOGY, v. 66, p. 653–669.
- Sharp, Z.D., 1990, A laser-based microanalytical method for the in situ determination of oxygen isotope ratios of silicates and oxides: Geochimica et Cosmochimica Acta, v. 54, p. 1353–1357.
- Sharp, Z.D., Atudorei, V., and Durakiewicz, T., 2001, A rapid method for determination of hydrogen and oxygen isotope ratios from water and hydrous minerals: Chemical Geology, v. 178, p. 197–210.
- Shepard, W.M., Morris, H.T., and Cook, D.R., 1968, Geology and ore deposits of the East Tintic mining district, Utah, in Ridge, J.D., ed., Ore deposits of the United States, 1933–1967 (Graton Sales volume): New York, American Institute of Mining and Metallurgical Engineers (AIME), p. 941–965.
- Sheppard, S.M.F., and Gilg, H.A., 1996, Stable isotope geochemistry of clay minerals: the story of sloppy, sticky, lumpy and tough, Cairns-Smith (1971): Clay Minerals, v. 31, p. 1–24.
- Sheppard, S.M.F., Nielsen, R.L., and Taylor, H.P., 1969, Oxygen and hydrogen isotope ratios of clay minerals from porphyry copper deposits: ECONOMIC GEOLOGY, v. 64, p. 755–777.
- Shinohara, H., and Hedenquist, J.W., 1997, Constraints on magma degassing beneath the Far Southeast porphyry Cu-Au deposit, Philippines: Journal of Petrology, v. 38, p. 1741–1752.
- Short, M.N., and Ettlinger, I.A., 1926, Ore deposition and enrichment at the Magma mine, Superior, Arizona: American Institute of Mining, Metallurgical, and Petroleum Engineers Transactions, v. 74, p. 174–222.
- Short, M.N., Galbraith, F.W., Harshman, E.N., Kuhn, T.H., and Wilson, E.D., 1943, Geology and ore deposits of the Superior mining area, Arizona: Arizona Bureau of Mines Bulletin, v. 151, p. 139–154.
- Silberman, M.L., and Noble, D.C., 1977, Age of igneous activity and mineralization, Cerro de Pasco, central Peru: ECONOMIC GEOLOGY, v. 72, p. 925–930.
- Sillitoe, R.H., 1983, Enargite-bearing massive sulphide deposits high in porphyry copper systems: ECONOMIC GEOLOGY, v. 78, p. 348–352.
- 2000, Styles of high-sulfidation gold, silver and copper mineralization in porphyry and epithermal environments: PacRim '99, Bali, Indonesia, 2000, Proceedings, p. 29–44.
- Simmons, S.F., 1991, Hydrologic implications of alteration and fluid inclusion studies in the Fresnillo district, Mexico: Evidence for a brine reservoir and a descending water table during the formation of hydrothermal Ag-Pb-Zn orebodies: ECONOMIC GEOLOGY, v. 86, p. 1579–1601.
- Simmons, S.F., and Browne, P.R.L., 1997, Saline fluid inclusions in sphalerite from the Broadlands-Ohaaki geothermal system: A coincidental trapping of fluids being boiled toward dryness: ECONOMIC GEOLOGY, v. 92, p. 485–489.
- Soler, P., Carrascal, R., and Saez, J., 1986, Mineralization and paragenesis of the Huanzala mine, central Peru—a discussion: ECONOMIC GEOLOGY, v. 81, p. 195–196.
- Spoeltl, C., and Vennemann, T.W., 2003, Continuous-flow IRMS analysis of carbonate minerals: Rapid Communications in Mass Spectrometry, v. 17, p. 1004–1006.
- Stoffregen, R.E., Rye, R.O., and Wasserman, M.D., 1994, Experimental studies of alunite: I. <sup>18</sup>O-<sup>16</sup>O and D-H fractionation factors between alunite and water at 250–450°C: Geochimica et Cosmochimica Acta, v. 58, p. 903–916.
- Taylor, B.E., 1986, Magmatic volatiles: Isotopic variation in C, H, and S: Reviews in Mineralogy, v. 16, p. 185–226.
- 1988, Degassing of rhyolitic magmas: hydrogen isotope evidence and implications for magmatic-hydrothermal ore deposits: Canadian Institute of Mining and Metallurgy Special Volume 39, p. 33–49.
- Thomson, D.R., 1960, The Yauricocha sulfide deposit, central Peru: Unpublished Ph.D. thesis, UK, University of London, 170 p.
- Thouvenin, J.-M., 1984, Le gisement polymétallique à Zn-Pb-Cu-Ag de Huaron (Pérou): description des corps minéralisés, étude paragenétique, datations K/Ar des altérations hydrothermales, répartition de l'argent: Chroniques de la recherche minière, v. 477, p. 35–54.
- Ulrich, T., Günther, D., and Heinrich, C.A., 1999, Gold concentrations of magmatic brines and the metal budget of porphyry copper deposits: Nature, v. 399, p. 676–679.
- Vennemann, T.W., and O'Neil, J.R., 1993, A simple and inexpensive method of hydrogen isotope and water analyses of minerals and rocks based on zinc reagent: Chemical Geology, v. 103, p. 227–234.
- Ward, H.J., 1961, The pyrite body and copper orebodies, Cerro de Pasco mine, central Peru: ECONOMIC GEOLOGY, v. 56, p. 402–422.
- Wasserman, M.D., Rye, R.O., Bethke, P.M., and Arribas Jr, A., 1992, Methods for separation and total stable isotope analysis of alunite: U.S. Geological Survey Open-File Report 92–9, 20 p.
- Zachos, J., Pagani, M., Sloan, L., Thomas, E., and Billups, K., 2001, Trends, rhythms, and aberrations in global climate 65 Ma to Present: Science, v. 292, p. 686–693.
- Zhang, X., Nesbitt, B.E., and Muehlenbachs, K., 1989, Gold mineralization in the Okanagan Valley, southern British Columbia: Fluid inclusion and stable isotope studies: ECONOMIC GEOLOGY, v. 84, p. 410–424.
- Zheng, Y.F., 1999, Oxygen isotope fractionation in carbonate and sulfate minerals: Geochemical Journal, v. 33, p. 109–126.

**APPENDIX**  
 Examples of Fluid Inclusion and Stable Isotope Data from a Number of Different Polymetallic Epithermal Deposits (Cordilleran type)

Location	Age(Ma)	Host rock	First-stage main ore minerals described	Second-stage main ore minerals	Fluid inclusion data <sup>1</sup>	Stable isotope data	Interpretation
Cerro de Pasco, Peru	15-11	Mainly carbonate rocks (Pucará Grp.) but also diatreme breccia and siliciclastic rocks (Excelsior Fm.)			First stage: 185°-275°C and 0.5-12 wt % NaCl equiv Second stage: 170°-290°C		This study
Colquijirca, Peru	10.6-12.4	Mainly carbonate Pocobamba Fm. but also in diatreme breccia and dacitic volcanic rocks		enr, cpy, tn-tt, bn, sl, gn	165°-300°C and 0.2-7 wt % NaCl equiv	$\delta^{18}\text{O}$ and $\delta\text{D}$ values from 1.9 to 12.8‰ and from -97 to -142‰ (kaol)	Mixing of magmatic brine and meteoric water (Bendezú, 2007)
Huanzala, Peru	7.7 ± 0.4	Santa Formation limestone	po, asp, sl	tn, enr	Early stage: 200°-330°C Late stage: 250°-330°C	No data	Imai et al. (1985), Imai (1986)
Hualgayoc, Peru	~11	Limestones from the Chulec Fm. and sandstone from the Goyllarisquizga Group and the Inca Fm.		replacement bodies: po, asp, sl, veins: enr, tn, cp, pyrg, sl, gn	170°-300°C and 1.2-12.0 wt % NaCl equiv	$\delta^{18}\text{O}$ and $\delta^{13}\text{C}$ (cal and rdc) from 9.1 to 13.8‰ and from -3.6 to -9.8‰	Macfarlane et al. (1994)
Juleani, Peru	10.1-7.0	Dacite-rhyolite domes		enr, cp, sl, gn	180°-330°C and 2.7-11.2 wt % NaCl equiv	$\delta^{18}\text{O}$ - $\delta\text{D}$ : -8.7 to +3.7‰ and -112 to -60‰ (from fluid inclusions)	Magmatic brine mixing with isotopically exchanged meteoric water. (Deen et al., 1994)
San Cristobal, Peru	~5-6	Pucará Group limestone, Mítu Group volcanics	py-qtz body, py, wf, asp, sl	tt, sl-gn	Early stage: 205°-260 °C and 2.9 to 5.1 wt % NaCl equiv (Beuchat, 2003). 230°-330°C and 1-6.3 wt % NaCl equiv (Campbell et al., 1984) Late stage: 150°-320°C and 0.2-7 wt % NaCl equiv (Campbell et al., 1984)	Early stage: $\delta^{18}\text{O}$ - $\delta\text{D}$ in qtz and wf: 1.4 to 7.3‰ and -58 to -148‰ (Campbell et al., 1984) Late stage: 5 to 7‰ and -90 to -140‰ (Beuchat, 2003)	Mixing of magmatic brine with isotopically exchanged meteoric water (Campbell et al., 1984 and Beuchat et al., 2004)
Pasto Bueno, Peru	~9	Quartz-monzonite Consuzo stock	wf, po, asp, mo,	late stage: enr, tt, sl, gn	175°-290°C and 2-17 wt % NaCl equiv	$\delta^{34}\text{S}$ sulfide: -6.0 to +3.0‰ $\delta^{18}\text{O}$ - $\delta\text{D}$ : -0.2 to +6‰ and -50 to -110‰	Meteoric water mixing with magmatic brine (Landis and Rye, 1974)

## APPENDIX (Cont.)

Location	Age(Ma)	Host rock	First-stage main ore minerals described	Second-stage main ore minerals	Fluid inclusion data <sup>1</sup>	Stable isotope data	Interpretation
Main and East Tintic, Utah, United States	Late Eocene	Paleozoic limestones (Ophir Fm.)		enr, tn-tt, Ag-gn, sl	160°–360°C and 0.2–8.8 wt % NaCl equiv (Hildreth and Hannah, 1996) 150°–200°C (Batchelder et al., 1978)	$\delta^{18}\text{O}$ - $\delta\text{D}$ in FI in qtz: –5.1 to 0.0‰ and +121 to –118‰ $\delta^{18}\text{O}$ - $\delta\text{D}$ in FI in py: similar $\delta^{18}\text{O}$ and –118 to –101 and –89 to –84 (Batchelder, 1978); $\delta^{34}\text{S}$ : –2.0‰ (Hildreth and Hannah, 1996)	Early fluids represent magmatic fluids (formation of early quartz) and late high salinity fluids formed main ore (Hildreth and Hannah, 1996)
Butte Main stage, Montana, United States	66–63	Butte quartz-monzonite		enr, cc, bn, cv, dg, tn, cp, sl, gn	Main stage:	Main stage: $\delta^{34}\text{S}$ sulfides: –3.7 to +4.8‰	Field et al. (2005)
Bisbee, Arizona, United States	Late Jurassic	Argillaceous limestone		enr, bn	300°–340°C		Friedhauf (1998)
Collahuasi vein, Chile	32.9 (porphyry stage)	Porphyry stock and volcano-sedimentary rocks		py-cp-(tn), py-bn-(enr), cc-dg-cv	220°–320°C and 0.7–6.8 wt % NaCl equiv	No data	Masterman et al. (2005)

<sup>1</sup> All fluid inclusions reported were measured in quartz

Mineral abbreviations: asp = arsenopyrite; bn = bornite; cc = chalcocite; cp = chalcopyrite; est = cassiterite; cv = covellite; dg = digenite; enr = enargite; fm = famatinite; gn = galena; lz = luzonite; mt = magnetite; mo = molybdenite; po = pyrrhotite; pyrg = pyrrargyrite; py = pyrite; sl = sphalerite; tn = tennantite; tt = tetrahedrite; wf = wolframite

